Local- and Mesoscale Variability of Winds in the Complex Topography of Southwestern Norway and Iceland

Marius Opsanger Jonassen

Dissertation for the degree of philosophiae doctor (PhD)
University of Bergen, Norway

September 2012

Acknowledgements

First and foremost I would like to express my sincere gratitude to my supervisors Haraldur Ólafsson and Joachim Reuder. They have taught me a lot within the fields of atmospheric dynamics, numerical modelling and experimental meteorology. And who would have thought a model aircraft could be anything more than just a toy?! Joachim has taught me a great deal about model aircraft during all the interesting field campaigns he's brought me to, both in Norway and abroad in France, Germany and elsewhere. Martin Müller and Christian Lindenberg also deserve many thanks, not only for assembling the model aircraft, but also for being pleasant company during many field campaigns.

Haraldur and our fellow colleague Ólafur Rögnvaldsson at the Institute for Meteorological Research hosted me for several months in Iceland, which I am very grateful for. I would also like to thank Hálfdán Ágústsson, not only for many interesting scientific discussions, but also for introducing me to Icelandic football. Parts of my stays in Iceland were funded by the Icelandic Technology Development Fund (Grant 110338-0611) and other parts were funded by the Arctic Studies Grant.

Stephanie Mayer got me off to a flying start with the Weather Research and Forecasting model (WRF) and has also been a nice colleague to work together with over the last few years. My office mates Ellen Viste and Martin Flügge have been pleasant company during many long working hours. Ellen's been a good fellow for discussing meteorological topics and I also enjoyed teaching an introductionary course in meteorology together with her. Martin has done his fair share of motion correction, which is always appreciated. He has also kept me up to date with the latest news from online newspapers, like when a man fell down a ventilation shaft right outside the institute building! Stephanie Gleixner has been a welcome addition to our office milieu, and I hope she has a good time here in Bergen.

I would also like to thank Joan Cuxart and his group at the University of the Balearic Islands in Mallorca for hosting me for several months in 2010 and 2011. I learned a lot during those stays and I hope we will continue our collaboration in the future. The Geophysical Institute and ResClim funded my stays in Mallorca and deserve many thanks.

Last but not least, I would like to thank my friends and family. They have always been there for me when I've needed them.

Marius Opsanger Jonassen
Bergen, September 2012

Abstract

In this study, consisting of four scientific papers, we investigate local- and mesoscale variability of winds in the complex terrain of southwest Norway and Iceland. In Paper 1, we find southwesterly and northeasterly flow in a coastal region of southwestern Norway is orographically enhanced at the ground level. Southeasterly and stably stratified northwesterly, on the other hand, is decelerated by blocking and wake effects. These findings largely confirm those of previous studies with idealised simulations of flow in the area. Furthermore, we deduce a new way of quantifying the wind distribution in the area through a two-parameter Weibull function. The inland locations are associated with low, but variable wind speeds (low shape and scale parameters). In the coastal and offshore locations, the winds are less variable and stronger (high shape and scale parameters). The mountain top wind speed distribution is fundamentally different from the others: it shares the high variability with the inland locations, and it shares the strong winds with the coastal and offshore locations. In strong southwesterly flow, the city centre of Bergen appears to be sheltered with respect to its surroundings. In Paper 2, we investigate this wind shelter in detail. In the numerical simulations of two southwesterly windstorms, we remove the mountains up- and downstream of Bergen (Løvstakken and Fløyen) from the model topography. We find that the wind shelter is a combination of both a wake from Løvstakken and a blocking from Fløyen. Furthermore, Løvstakken acts to significantly increase the precipitation in the city centre through spillover. The findings from Paper 1 and 2 confirm the potentially significant impact of mountains on local- and mesoscale variability of winds in the area. Previous studies have shown that mountains' surface characteristics in terms of friction and thermal properties can modify gravity waves and downslope flows, which are common flow patterns in connection to topography. In Paper 3, we study the sensitivity of flow over the mesoscale Hofsjökull mountain in Iceland to the underlaying surface characteristics. We find that removing the mountain's ice cap from the model landuse data, leaving a rougher and warmer surface, dampens gravity waves and downslope flow acceleration. The impact from the surface friction is greatest. The impact from the surface heating is larger when the surface is rough than when it is smooth. We explain this latter finding by referring to vertical profiles of wind and turbulent mixing. High horizontal grid resolution is important for appropriately resolving local- and mesoscale flow phenomena. Validating such simulations, on the other hand, is a challenge. In Paper 3, we confirm the utility of a remotely piloted aircraft system (RPAS), called the small unmanned meteorological observer (SUMO), for the validation of simulated atmospheric flow. In Paper 4, we use temperature, humidity and wind profile data from SUMO to improve simulations of mesoscale, thermally driven flow in the form of sea breeze in southwestern Iceland. We find that the assimilation of the SUMO data leads to an improvement in the simulated horizontal and vertical extent of the sea breeze circulation along with a better reproduced local component of the background flow.

Papers

- **Paper 1: Multi-scale variability of winds in the complex topography of southwestern Norway**
  Jonassen, M. O., Ólafsson, H., Reuder, J. and Olseth, J. A. (2012)
  Tellus 64A pp. 1−17

- **Paper 2: Simulations of the Bergen orographic wind shelter**
  Jonassen, M. O., Ólafsson, H., Valved, A. S., Reuder, J. and Olseth, J. A.
  Submitted to Tellus A

- **Paper 3: Impact of surface characteristics on flow over a mesoscale mountain**
  Jonassen, M. O., Ágústsson, H. and Ólafsson, H.
  Submitted to Quarterly Journal of the Royal Meteorological Society

- **Paper 4: Improving High-Resolution Numerical Weather Simulations by Assimilating Data from an Unmanned Aerial System**
  Jonassen, M. O., Ólafsson, H., Ágústsson, H. Rögnvaldsson, Ó. and Reuder, J.
  Accepted for publication in Monthly Weather Review, 2012

Contents

1 Introduction

This thesis contributes to an increased understanding of variability in local- and mesoscale flows in complex terrain. We focus on the areas of southwestern Norway and Iceland. These areas, both situated along the North Atlantic storm track, are dominated by rapidly shifting weather with typically large day-to-day variations in wind, temperature and precipitation. Knowledge about the weather in these areas has been essential for centuries, firstly for survival and later for the security of natural resources and property. This is especially true for the coastal areas which are to a large extent freely exposed to frequently passing storms.

Studies of the weather in the region date back to at least the "King's Mirror" (old Norse: Konungs skuggsjá), written in the 13th century for king Håkon Håkonsson and Magnus the Law-mender. In modern times, this was followed by pioneering work of the Bergen School of Meteorology (Bjerknes and Solberg, 1921, 1922). As the observational record increased, forecasting rules for winds and precipitation in Southern Norway were established. These were documented by Finn Spinnangr (Spinnangr, 1943a,b). Later, Godske et al. (1957) made a review of relevant dynamics, based partly on the theories developed by the Bergen School of Meteorology. Particularly relevant to the present work are the references of Godske et al. (1957) to the work by Tor Bergeron on the "corner effect" which causes strong winds in the form of a jet along the southwest coast of Norway. This jet continues to be of interest to modern day weather forecasting as it affects all human activities along the southwest coast of Norway, including shipping, fishing, oil industry and wind energy production. Later, Andersen (1975) published an overview of different wind patterns classified by periods of certain prevailing large-scale wind conditions which he referred to as "H. Johansen weather types".

Lacking the detailed four dimensional observation and simulation datasets we have today, the results in the aforementioned literature were mainly based on simplified flow patterns and sporadic case studies. Furthermore, as was also the case for meteorological research in general at the time, most studies were focused either on the larger/synoptic ($>$2000 km) or local ($<$2 km) scales. The revolution within computational resources in the 70's and 80's sparked a rapid evolution in the research on the intermediate scale, the so called mesoscale (e.g. Pielke, 2002).

Steadily increasing computational power allows mesoscale atmospheric models to be run at horizontal resolutions of 1 km, or even distinctly below that for studies limited in time and space. High resolution is necessary for appropriately resolving local- and mesoscale atmospheric phenomena. While the increased resolution represents an important step forward for numerical weather prediction, the provision of correspondingly high resolution observations needed for validation becomes increasingly challenging. The advancement of observational technologies and the increased number of mesoscale observational networks (e.g. Lin, 2007), contributed significantly to the rapid evolution of mesoscale meteorology. Models used for the simulations of real atmospheric flows are

not only dependent on observations for validation, but also for the provision of initialisation and forcing data. Even today, with relatively new remote sensing technologies, such as radar and satellites, there are regions with sparse data coverage, e.g. the Arctic, the Antarctic and the world's oceans. Hence, the quality of weather forecasts in these and neighbouring regions suffer from a lack of observational data. Data from novel platforms capable of doing in-situ measurements in the region, such as from remotely piloted aircraft systems (RPAS), may improve upon this in the future. The utility of several such platforms, such as the Aerosonde (Holland et al., 1992), the Meteorological Mini Aerial Vehicle (M^2AV; Van den Kroonenberg et al., 2008) and the Small Unmanned Meteorological Observed (SUMO; Reuder et al., 2009), has been demonstrated in recent years.

Using modern capabilities within mesososcale atmospheric modelling, the recent studies of Barstad and Grønås (2005, 2006) significantly added to knowledge about mesoscale flow over Southern Norway. Among their main findings, was a jet forming along the mountain slopes and out over the sea (referred to as a 'left-side' jet) in southwesterly large-scale flow. This is the same jet as mentioned in Godske et al. (1957). However, Barstad and Grønås (2005) found the jet to be caused by the rotational effects on the flow rather than coastal convergence as was suggested previously. In addition, Barstad and Grønås (2005) found lee-side effects such as downslope accelerated winds and a wind shadow connected to inertio-gravity waves in southeasterly to southerly flow.

The history of peer-review studies on local- and mesoscale flows in Iceland is not as long as that of southwestern Norway. Nevertheless, following the recent evolution in observational and modelling capabilities, several studies have emerged during recent years. For example, gust factors in relation to surrounding terrain were studied by Ágústsson and Ólafsson (2004) and Ágústsson and Ólafsson (2009). Downslope flows have been studied by Ágústsson and Ólafsson (2012) and Rögnvaldsson et al. (2011). Bromwich et al. (2005) performed a high resolution climate simulation over Iceland, which they used to analyse the near-surface climate. They found amongst other things land-sea-breeze circulation to be evident in summer and katabatic winds to be an important climatic feature in winter.

The terrain morphologies and climates of Iceland and southwestern Norway are quite similar, and the results of the mentioned studies from Iceland and Norway are presumably mostly valid for both places.

2 Main Objectives

In **Paper 1** of this thesis, one of our aims is to find further observational evidence for the findings of Barstad and Grønås (2005) on the mesoscale flow structures for an area of the southwest coast of Norway. Their study contained a section where reanalysis data and observations from a limited set of automatic weather stations (AWSs) along the

coast were used to validate their results. As with the rest of their study, this section was limited to flow between the south and west sectors. In our study, we use an extensive set of observations from several AWSs along with reanalysis data to validate their findings. We extend the study to yield all larger scale wind directions and we aim to establish a more detailed picture on how the flow on the local scale relates to that on the larger scale. Furthermore, we aim to deduce a new classification of the wind speed distribution in the area using the two-parameter Weibull function.

In **Paper 2**, our main aim is to investigate why the city centre of Bergen is sheltered during strong southwesterly flow. This sheltering is one of the main findings in Paper 1 on the relationship between the smaller and larger scale flow in the Bergen area. Evidence for the sheltering is also found in the study of Harstveit (2006). We use numerical simulations of two southwesterly windstorms in which each of the two mountain massifs (Løvstakken and Fløyen) up- and downstream of the city are stepwise removed from the model topography. We also seek to find out whether the data from the "Florida" AWS are representative for the wind in the city centre of Bergen as a whole. Bergen is not only a calm place, it is also very wet. In fact, Bergen is among one of the wettest cities — if not the wettest — city in Europe, with an average of 2250 mm per year. Precipitation is not the main topic of this thesis, but we include some results on local precipitation in Bergen in Paper 2. It is well recognised that the relatively high annual precipitation amounts along the southwestern coast of Norway are caused by the south Norwegian mountain range (e.g. Steensen et al., 2011). It has, however, until now been unclear how the local mountains around Bergen affect the precipitation in the city through e.g. the "spillover" effect as described by Sinclair et al. (1996).

In **Paper 3**, our main aim is to evaluate the effects of surface heat fluxes and surface friction on flow over the mesoscale, glacier covered mountain of Hofsjökull. A recent dynamical downscaling of flow over Iceland (Rögnvaldsson et al., 2007) shows a persistent downstream shift in the wind speed maximum over the larger glaciers. This flow pattern resembles closely what can be expected in the presence of gravity waves. Idealised modelling studies have shown that surface friction (e.g. Richard et al., 1989; Georgelin et al., 1994; Ólafsson and Bougeault, 1997) and adiabatic heating (e.g. Raymond, 1972; Smith and Skyllingstad, 2011) of flow over mountains can potentially have a significant detrimental impact on gravity waves. We hypothesize that the cold and smooth surface of the glaciers could be the reason for the described persistent downstream shift in the wind speed maximum. To find out, we simulate two summertime cases from the international FLOHOF field campaign, 2007 (Reuder et al., 2011). In several model sensitivity experiments, we modify the surface of Hofsjökull to investigate the impact of its surface characteristics on the gravity waves and downslope flow.

In **Paper 4** we aim to demonstrate how high resolution numerical weather simulations of a mesoscale flow pattern can be improved by the assimilation of temperature, humidity and wind data from the SUMO RPAS. For this application, the four dimensional data assimilation (FDDA) capability of the Weather Research and Forecasting

model (WRF) is used. We apply the SUMO FDDA system to two cases of summertime fair weather situations from the Moso field campaign in Southwest Iceland, 2009. The situations were dominated by thermally driven flow in the form of sea breeze circulation along the coast. The sea breeze is a good example of a finely balanced mesoscale system which operational weather forecasting models often fail to reproduce accurately (e.g. Fuentes et al., 2005).

3 Background Theory and Experimental Method

In the atmospheric sciences, observations, theory and numerical models are all essential tools. In this thesis, we make use of all of these tools. Numerical models along with theory have significantly increased our understanding of many observed weather phenomena. To predict a real atmospheric state, in turn, the numerical models are dependent on input from observations for initial and boundary conditions. Model simulations also rely on observational data for verification. Verification studies lead to revisions of models, which in turn call for more observations for the validation of the revisions. In this way, observations and models are used to guide each other's development and improvement which ultimately further our understanding of the weather. Models, theory and observations as tools in atmospheric research can be regarded as equally important (Warner, 2011).

3.1 Mountain flow theory

Mountains and hills impact atmospheric flow mainly through two basic processes. One is the dynamical aspect through which mountains perturb existing atmospheric flow. These perturbations take the form of e.g. gravity waves, upstream blocking and downstream wakes, downslope accelerated flows, corner winds and jets. A second mechanism is thermally driven flow which arises through thermal contrasts, connected to differential heating of mountains and the surrounding areas (mountain and valley winds). The first process will be the topic of this section. Orographic flow perturbations, and especially gravity waves, have been the subject of theoretical studies for decades. Among the pioneers in the field were Lyra (1943) and Queney (1948) who found solutions for flow over idealised, rectangular and bell shaped mountains. These first theoretical studies assumed a uniform upwind flow speed U and a uniform atmospheric stability, expressed by the Brunt Väisälä frequency, $N = \sqrt{\frac{g}{\theta_{avg}} \frac{d\theta}{dz}}$ where g, θ and z are the acceleration of gravity, the potential temperature and the altitude, respectively. These assumptions are still widely used in many studies of mountain flow. Later, Scorer (1949) famously deduced analytical solutions for trapped lee waves. As Wood (2000) points out in his historical review of mountain flow theory, much progress was made in the beginning by refining and making Scorer's analysis more realistic (e.g. Wallington and Portnall, 1958; Sawyer, 1960; Foldvik, 1962).

As in Queney (1948), more recent studies also work with linearised solutions, giving analytical flow solutions (e.g. Smith, 1979). These studies extend to flow over 3D mountains, with scales on the order of 1 km. Other studies of such flows are mentioned in the review by Durran (1990). On this scale, the effect of the earth's rotation on the flow is negligible. Using the Boussinesq approximation, and by assuming a linear, stratified flow over an isolated mountain with no surface friction, it can be shown that

(e.g. Pierrehumbert and Wyman, 1985; Smith and Grønås, 1993) the flow is governed by the non-dimensional mountain height $\hat{h} = Nh/U$, i.e. the inverse Froude number. N and U are defined above and h is the mountain height. Various flow regimes have been defined and described based on this parameter (e.g. Lin and Wang, 1996; Trüb and Davies, 1995; Ólafsson and Bougeault, 1996; Peng et al., 1995). For flow over a simple 3D obstacle, Smith (1989) describes the three following flow regimes:

1) For low values of $\hat{h}$, the flow typically passes over the mountain with ease, without any upstream blocking and gentle gravity waves form. $\hat{h}$ can be seen as a measure of the linearity of the flow and linear mountain wave theory describes the flow response well within this range (Gill, 1982).

2) High values of $\hat{h}$ are typically associated with upstream flow stagnation and splitting, i.e. the flow is diverted to either side of the mountain on its upwind side. Weak gravity waves may form along with lee-side vortices. The pressure perturbations set up by the mountains are small within this regime as there is only weak flow lifting.

3) For values of $\hat{h}$ close to unity, the flow is dominated by a high-drag state (large pressure perturbations). In this state, there are typically amplified or even breaking gravity waves and strong downslope flow on the mountain's lee side.

For flow on larger scales, the rotation of the earth influences the flow over mountains. This influence can be quantified in terms of a non-dimensional parameter known as the Rossby number, $R_o = \frac{U}{fL}$. As for $\hat{h}$, U is the upstream flow speed. f is the Coriolis parameter and L is a length scale commonly considered as the mountain half width in the direction of the flow. Thus, a high R_o indicates low rotational effects on the flow and vice versa. An effect of rotation is to introduce assymmetries in flows in connection to mountains: as flow impinges on a mountain, a pressure surplus builds up on its upstream side as the flow is forced to ascend. This acts to decelerate the flow which induces an ageostrophic component in the flow, which is initially geostrophic. In the northern hemisphere, the flow is therefore accelerated to the left on the mountain's upstream side. Through this mechanism, rotation may render flow that would be blocked on a rotating plane, to be unblocked (Thorsteinsson and Sigurdsson, 1996; Ólafsson and Bougeault, 1997). It is the effect of rotation that is responsible for the left-side jet frequently forming along the southwestern coast of Norway in southwesterly flow as described by Barstad and Grønås (2005) and further investigated by us in Paper 1. Such jets are also known from many other locations in the world, e.g. Alaska (Overland and Bond, 1993), Greenland (Ólafsson and Ágústsson, 2009; Renfrew et al., 2009), and California (Doyle, 1997). Because the terrain is the forcing element of the flow, such jets are normally confined below the altitude of the mountain peaks (Parish, 1982; Barstad and Grønås, 2005).

A third non-dimensional parameter is the mountain aspect ratio $R = \frac{L_x}{L_y}$, where L_x and L_y are the mountain half widths along and across the main flow direction.

Figure 1 of Petersen et al. (2005), which is here reproduced in Figure 1, nicely

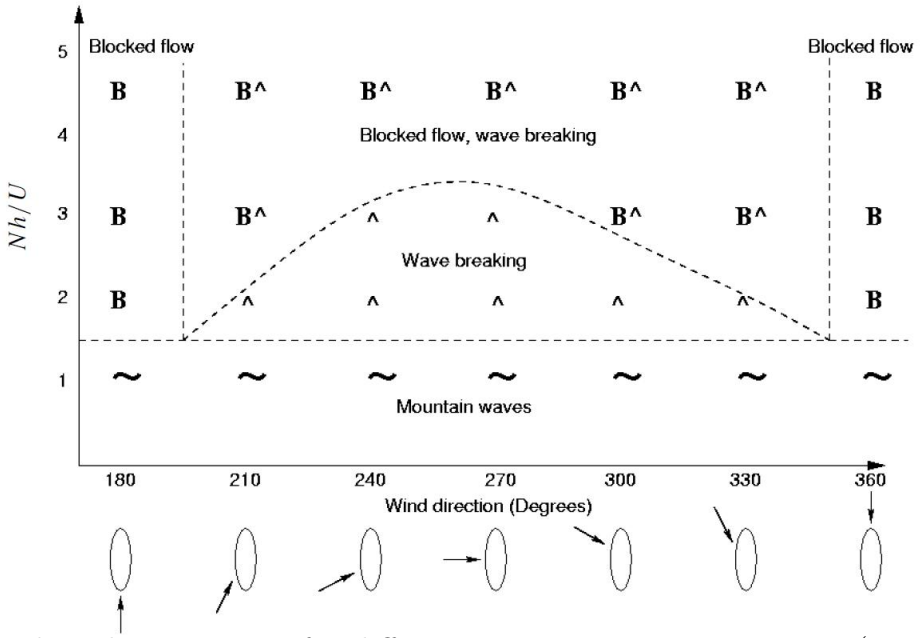

Figure 1: Flow characteristics for different mountain aspect ratios, R (= 4 for westerlies and 0.25 for northerlies) and values of the non-dimensional mountain height, $\hat{h}$. Reproduced from Petersen et al. (2005)

summarises the effect of R for various wind directions and values of $\hat{h}$. The mountain corresponds to the size of Greenland (200 x 800 km), but its shape and north-south alignment resembles that of South Norway.

It can be seen that a value of $\hat{h}$=2 is sufficient to cause blocking for southerly flow, while blocking does not start before around $\hat{h}$=3.5 for westerly flow. This is caused by the above explained effect of rotation which is larger when the flow has to travel farther in the westerly than in the southerly case to get around the mountain. Interestingly, for the non-rotational case, the effect of the aspect ratio is the opposite (e.g. Smith, 1989): A mountain elongated across the flow would cause blocking for lower values of $\hat{h}$ than a mountain elongated along the flow.

3.2 Remotely Piloted Aircraft Systems (RPASs) in atmospheric sciences

Apart from the observational data from conventional platforms like automatic weather stations (AWS) used in all four papers of this thesis, in Papers 3 and 4 we make use of measurements from a new tool for boundary layer measurements which is based on a light weight RPAS. RPAS is also known under other acronyms, such as UAS (unmanned aerial / aircraft system). In this introductionary part, we use "RPAS", which was assigned as the official acronym by the International Civil Aviation Organization (ICAO) in 2012. However, in the four papers of this thesis, and by many of the references therein, UAS is more widely used.

RPASs, consisting mainly of an unmanned aircraft and a ground control station,

have undergone a technical revolution over the past few decades. Since their first application for atmospheric research in the late sixties (Konrad et al., 1970), they have been developed into autonomous platforms featuring advanced navigational systems and mission planning tools. Particularly the smaller RPASs are relatively user friendly and cost efficient to operate. RPASs' flexibility is unique in terms of controllability when compared to e.g. tethered sondes and radiosondes as they can be operated both to perform horizontal transects as well as vertical profiles. Data delivery is fast or even instantaneous. Unlike most lidar, radar and satellite based systems, the data acquisition does not rely on similarity or propagation assumptions and it is undisturbed by clouds. RPAS is thus a system with the potential to close the observational gap in the atmospheric boundary layer (ABL) between the aforementioned conventional instrument platforms. Examples of RPASs for atmospheric research include the Aerosonde (Holland et al., 1992; Curry et al., 2004), which has amongst other things been used for observations of hurricanes over the Atlantic Ocean (Cascella, 2008) and katabatic flows in the Antarctic (Cassano and Knuth, 2010). With a wingspan of 3 m, a weight of 14 kg and an endurance of some hours, the Aerosonde is a relatively small RPAS and far smaller than the larger ones like the Global Hawk (wingspan 35 m and weight 5000 kg, National Aeronautics and Space Administration (NASA) and National Oceanic and Atmospheric Administration (NOAA)) which can remain in the air for more than a 24 hours. The Manta is a RPAS similar in size to the Aerosonde and it has been used for e.g. the measurement of atmospheric heating rates of black carbon (Ramanathan et al., 2007) and turbulent water vapor fluxes (Thomas et al., 2012). The Meteorological Mini Aerial Vehicle M^2AV (Van den Kroonenberg et al., 2008; Martin et al., 2011) is another small sized RPAS which has been used to obtain e.g. atmospheric soundings and measurements of turbulent heat fluxes.

In this thesis, we make use of the RPAS SUMO which has been developed by a collaboration between the Geophysical Institute, University of Bergen and Martin Müller engineering in Hildesheim, Germany. The system is based on an autopilot system developed under the open source Paparazzi project led by the French school for civil aviation (Ecole Nationale de l'Aviation Civile, ENAC) (Brisset et al., 2006). With a wingspan of 0.58 m and a weight of around 600 g, the Multiplex FunJet airframe of SUMO is most likely the lightest airframe currently in use for atmospheric research. It is electrically powered and the battery package gives it an endurance of 20–40 minutes, depending on the flight conditions and flight pattern. SUMO's small size and low demands for infrastructure makes it ideal for use in field campaigns in remote locations. It can be operated both during daytime and night-time. The maximum airspeed is currently around 15–20 m s^{-1}, which also defines the wind speed limit for operations. Temperature, relative humidity and pressure are measured by onboard sensors. Wind speed and wind direction are indirectly estimated using information from the onboard Global Positioning System (GPS). The SUMO wind algorithm is described in detail by Mayer et al. (2012). For atmospheric profiling, we use a flight path resembling a helix with a radius typically

Figure 2: The SUMO airframe and the laptop used as the ground control station.

set between 50 and 100 m. So far, SUMO has been operated in a total of 10 international field campaigns, and more than 700 scientific measurement flights have been performed. The system has been proven to provide measurement quality close to that of well established measurement platforms such as radiosondes (e.g. Jonassen, 2008; Mayer et al., 2012). The SUMO airframe, along with the ground control station, are depicted in Figure 2.

Performing measurements with a moving platform is a challenging task and there are generally more sources of measurement errors than for static platforms using the same instruments. One such error source is that of the sensor response time, which can be a critical factor when performing atmospheric profiles with a fast ascending and descending RPAS like SUMO. The combined temperature and humidity sensor in use for SUMO during the FLOHOF campaign was found by Jonassen (2008) to be relatively slow, with response times of around 5 and 12 seconds, respectively. Such a sensor lag time leads to a general warm / dry bias in the ascent profiles and a cold / moist bias in the descent profiles. We have therefore corrected all profiles used in this thesis with a corresponding algorithm outlined in Jonassen (2008).

3.3 The Weather Research and Forecasting model (WRF) and Four Dimensional Data Assimilation (FDDA)

For the numerical simulations of this thesis, we use the WRF model (Skamarock et al., 2008). WRF is a community model, with development led by the National Center for Atmospheric Research (NCAR). Typical applications for WRF focus on the mesoscale,

but the model also includes global climate and large eddy simulation (LES) capabilities. It can be used for real data simulations, such as for hindcasting and forecasting purposes, as well as for single column and idealised flow studies. The modelling suite encompasses a range of physical parameterisation schemes, and it supports various sets of atmospheric input data. Both single- and two-way nesting is supported. WRF is used world-wide, both for operational weather forecasting and for research purposes. It has two dynamical cores, one is the Nonhydrostatic Mesoscale Model (NMM) and the other is the Advanced Research WRF (ARW). We use the latter dynamical core in this study. For the initialisation and forcing data in the studies of Paper 2-4, we use operational analyses from the European Centre for Medium-Range Weather Forecasts, with 91 model levels and a horizontal resolution of 0.125 degrees.

Initialisation and forcing data data are typically created using advanced data assimilation methods. WRF also contains data assimilation capabilities such as the variational data assimilation (3D-VAR and 4D-VAR). In Paper 4, we use the computationally less expensive and numerically more simple four dimensional data assimilation (FDDA; e.g. Anthes, 1974; Stauffer and Seaman, 1990, 1994; Schroeder et al., 1990) option in WRF to improve a high resolution weather simulation. The FDDA technique is also referred to as Newtonian relaxation, or simply "nudging". It is used to force the model towards either existing gridded model results (grid nudging) or observations (obs nudging) that are assumed to be closer to the real atmospheric state. When used only in the beginning of the simulation, the application of FDDA is referred to as "dynamic initialisation". It can also continue to force the model throughout the simulation time and hence the name "four dimensional" data assimilation. The FDDA is implemented by adding an artificial tendency term to the governing model equations. This forcing term is based on the difference between the observed and modelled atmospheric state and details on the formulae are outlined in Stauffer and Seaman (1990). In the FDDA setup one can set a range of parameters. One is the nudging coefficient (s^{-1}), which controls the strength of the nudging. Another is the horizontal radius of influence (kilometres), which determines the size of the area that is affected by the nudging. One can also set a time frame for the impact of the nudging. The time frame can e.g. be set to 40 minutes before and after an atmospheric sounding was taken. The parameters that can be nudged are the u and v components of the wind and temperature and humidity.

4 Summary of the Results

In a series of four scientific papers, local- and mesoscale flow patterns in southwestern Norway and Iceland have been studied. The general conclusions are given below.

Our main findings in Paper 1 on the relation between the larger and smaller scale flows in the Greater Bergen area are summarised in Figure 3.

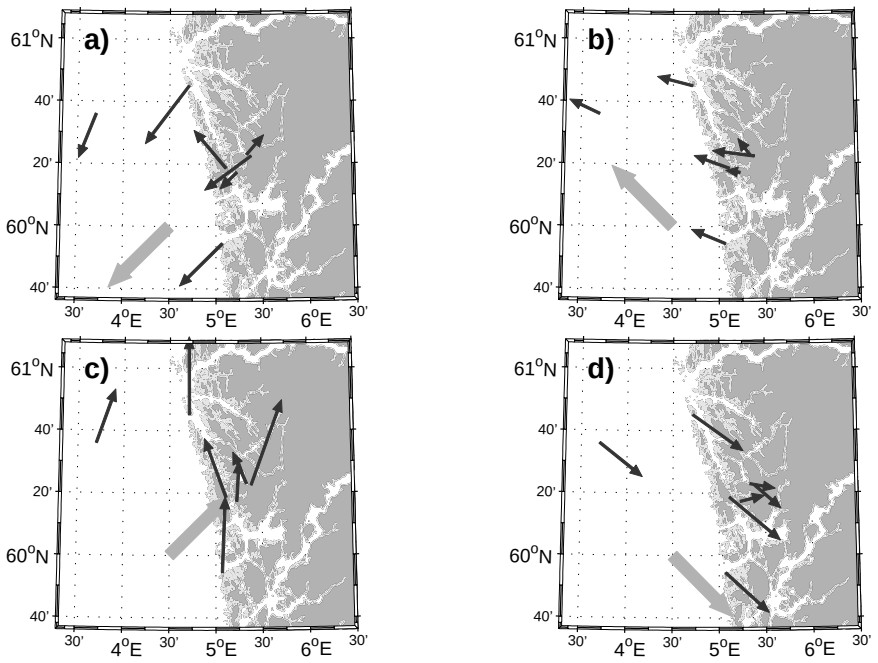

Figure 3: *Mean wind direction and wind ratio at surface stations (black arrows) as a function of four large scale wind directions (from ERA Interim data at 850 hPa, thick, grey arrows) over the greater Bergen area: (a) northeast (35-55°), (b) southeast (125-145°), (c) southwest (215-235°) and (d) northwest (305-325°). The wind ratio is indicated by the arrow lengths. For a wind ratio of 1, the black arrow has a length equal to that of the thick, grey arrow, meaning that the wind speed is the same at the surface as at 850 hPa. All 850 hPa wind speeds are above 5 m* s^{-1}*. Reproduced from Paper 1.*

We find southeasterly and stably stratified northwesterly flows over the Greater Bergen area are decelerated with respect to the larger scale flow through wake and blocking effects. Southwesterly and northeasterly winds, on the other hand, are orographically enhanced. For southwesterly flow, there is a strong clockwise turning in wind direction with height (veering). This veering can be explained both by a topographic steering by the roughly north/south oriented southwest Norwegian coast and mountain range and by the effect of the earth's rotation. For northwesterly flow, on the other hand, there is almost no turning in the wind direction with height. In general,

one would expect increased atmospheric stability to induce stronger deceleration of the flow at the surface with respect to the larger scale flow. For southwesterly flow over the area investigated, however, the average surface wind speeds are approximately the same for stable atmospheric conditions as for unstable conditions. This can be attributed to a left-side jet, which is induced by the effect of the earth's rotation and enhanced by increased atmospheric stability / increased non-dimensional mountain height (Nh/U) leading to a more pronounced upstream blocking. The results are in line with well established mountain flow theory and largely confirm the findings of Barstad and Grønås (2005) on south to westerly flows over southwestern Norway for the area investigated. Furthermore, we show the geographical wind speed distribution in the greater Bergen area can be classified in terms of a two-parameter Weibull function. The coastal and offshore locations are dominated by steady and strong winds (high Weibull shape and scale factors). The wind speed inland is on average lower, but more variable (low Weibull shape and scale factors). The wind speed distribution at the mountain tops is fundamentally different from the others: it shares the relatively high variability with the inland locations, and it shares the high average wind speeds with the coastal and offshore locations. A factor acting to increase the variability in the wind speed inland is thermally driven flow. We find that such flow dominates inland under quiescent synoptic conditions. The inland wind speed is typically significantly reduced by a relatively high surface friction. However, local mountains can also be expected to contribute to local deceleration of the flow through blocking and wake effects. We find the city centre of Bergen to be especially sheltered during strong southwesterly flow as represented by the "Florida" weather station. Variability of winds in the centre of Bergen, and the role of individual mountains in forming the local flow during southwesterly windstorms, are the main objectives of Paper 2.

In Paper 2, we numerically reproduce two southwesterly windstorms that impact southwestern Norway on 10 January 2009 and 25 November, 2011. As exemplified in (Figure 4 a)), the simulated flow along the southwest coast of Norway at 1200 UTC on 11 January, 2009, resembles closely that found in the idealised simulations by Barstad and Grønås (2005) and described by us in Paper 1. The highest wind speeds are found along the coast in the form of a jet reaching 30 m s^{-1} near the surface. The flow along the coast is turned towards the left with respect to the flow farther up- and downstream. As with the larger scale, there is also great variability in the wind field on the local scale (Figure 4 b)): relatively high wind speeds (20-25 m s^{-1}) are found along the coast and on the local mountain- and hilltops. Low wind speeds are found up- and downstream of the same hills (5-10 m s^{-1}). The city centre of Bergen stands out as one of the calmer areas, suggesting that the sheltering of Bergen is captured by the model. Both the high spatial variability and the observed temporal variability are confirmed by a comparison with a relatively dense network of AWSs. In a set of additional model sensitivity experiments, we investigate the sheltering of Bergen in further detail by removing each of the two mountains upstream (Løvstakken) and downstream (Fløyen)

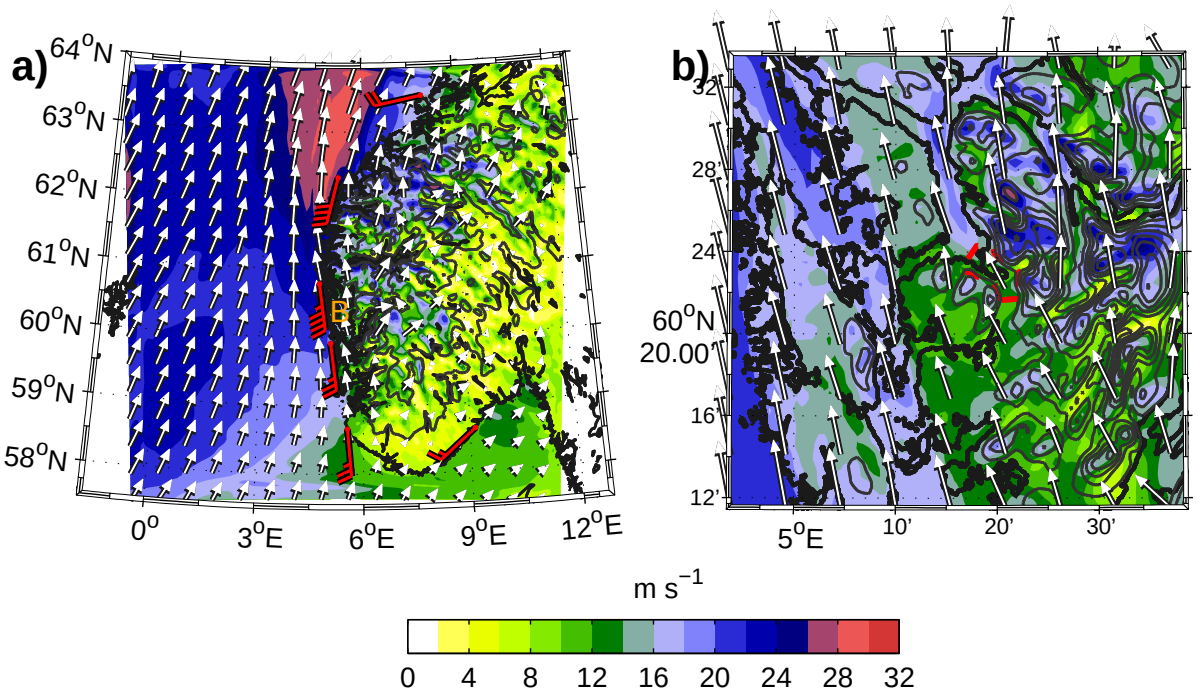

Figure 4: *Simulated near surface (19.5 m AGL) horizontal wind speed at 1200 UTC on 11 January 2009 for a), the outermost domain (4.5 km horizontal resolution) and b), the innermost domain (500 m horizontal resolution). Observations from selected AWSs along the coast are indicated with red wind barbs. Each barb is 2.5 m* s^{-1}*. The location of Bergen is indicated with a "B" in panel a) and with a red, dashed line in panel b).)*

from the model topography. The results show that the sheltering of Bergen is caused by a combination of a wake from Løvstakken and blocking from Fløyen. As could be expected, each effect is strongest closest to the respective mountains. At the Florida weather station, the blocking effect is the strongest. The impact of both mountains on the wind in the city is close to the sum of each of them. Previous experiments with idealised flow over two mountains, show that the effect of two mountains not always equals the sum of the individual effects from the two (e.g. Hunt and Richards, 1984; Grubišić and Stiperski, 2009; Stiperski and Grubišić, 2011). We find that a spillover effect from Løvstakken significantly enhances the precipitation in the city centre of Bergen for the wind storms investigated. Strong wind is known to strengthen the spillover effect (e.g. Sinclair et al., 1996). The effect is thus probably less prominent on the average than for the investigated strong wind cases. When compared to AWS observations from the area, our simulation results show only very little sensitivity to the choice of the model landuse and topography datasets.

Papers 1 and 2, both demonstrated significant impacts on the meso- and localscale flow patterns from mountains. Several studies have shown that the actual surface of the mountains can play an important role in how the different flow patterns manifest themselves. For example, both a high surface friction (e.g. Richard et al., 1989; Georgelin et al., 1994; Ólafsson and Bougeault, 1997) and positive surface heat fluxes (e.g. Ray-

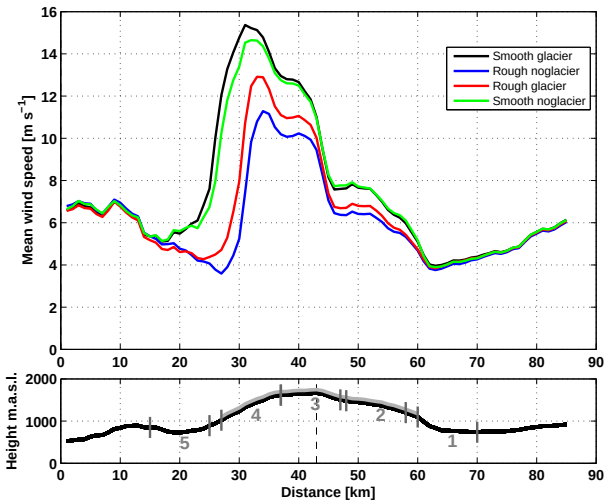

Figure 5: *Cross section of mean simulated near surface wind speed [m s^{-1}] (average over the three lowest model levels) on 13 and 14 August, 2007, for the four WRF simulations with differing model surface over Hofsjökull. The location of the characteristic areas 1) Upstream, 2) Upslope, 3) Mountain top, 4) Downslope and, 5) Downstream are indicated in this figure's lower panel. The location of the ice cap is indicated with a solid, grey line in the lower panel. The larger-scale flow direction is from the right to the left (from the northeast). Reproduced from Paper 3.*

mond, 1972; Smith and Skyllingstad, 2011) have been found to have a detrimental impact on gravity waves and downslope accelerated flow. In Paper 3, we investigate the effects of surface friction and heat fluxes on flow over the mesoscale Hofsjökull ice cap in Central Iceland. The main findings of this investigation can be summarised in Figure 5, showing mean near surface wind speed on 13 and 14 August, 2007, over Hofsjökull for four sensitivity simulations with differing mountain surface characterics. We find that both an increased surface friction and an increased heat flux over the mountain have a detrimental impact on the downslope flow acceleration and gravity waves. The above mentioned studies considered only one of these effects. To our knowledge, our study is the first to systematically address both effects. For our case studies, we find the detrimental effect of an increased surface friction to be larger than that of an increased surface heat flux. This result might be sensitive to the tested range of values for each of the parameters. Nevertheless, we believe that our results are representative for a plausible future scenario where the ice cap of Hofsjökull has melted. The cold and smooth surface of the glacier is probably the reason for the persistent downslope accelerated flow seen in the dynamic downscaling of flow over Iceland in Rögnvaldsson et al. (2007). Interestingly, the effect of the surface heat flux is larger over a rough than over a smooth mountain surface. This finding can be explained by referring to vertical profiles of wind and turbulent mixing.

Validation of high resolution simulations, as those in this study, is a challenging task. In Paper 3, we confirm the usefulness of the SUMO RPAS for the validation of the simulated flow aloft.

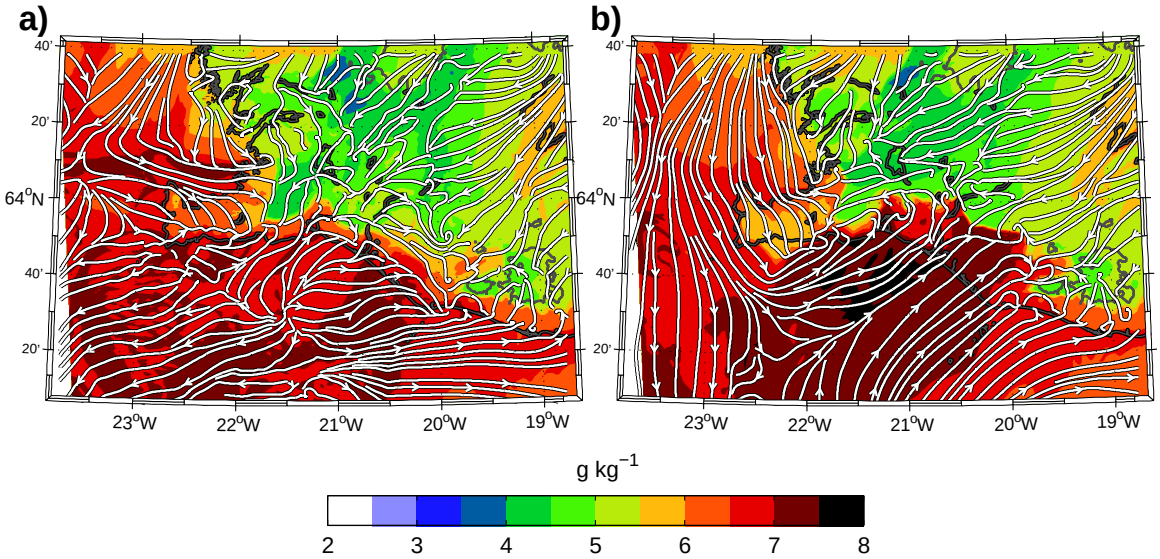

Figure 6: *Simulated wind direction and specific humidity (g kg^{-1}) in southwestern Iceland from the lowermost model half level (approximately 9 m AGL) at a horizontal resolution of 1 km at 1600 UTC 19 Jul 2009 for the (a) CTRL simulation and (b), FDDA-all simulation. Areas with over 98% relative humidity are encircled by a black, dashed line.*

Local- and mesoscale flows can be challenging to accurately reproduce with weather models. Thermally driven flow in the form of sea breeze is an example of flow that can be difficult for operational weather models to appropriately predict (e.g. Fuentes et al., 2005). In Paper 4, we demonstrate how a high resolution numerical weather simulations of mesoscale flow can be improved by assimilating data from the SUMO RPAS using FDDA. To the knowledge of the authors, this is the first time RPAS data have been assimilated into an advanced atmospheric simulation. In our study, the combined SUMO-FDDA system is applied to two summertime fair weather situations from the Moso field campaign in southwestern Iceland, on 19 and 20 July, 2009. The weather both days was dominated by a high diurnal boundary layer temperature variation leading to sea breeze circulation along the coast. The data assimilation leads to a more accurately reproduced vertical and horizontal extension of the sea breeze as well as a better description of the local component of the background flow. On 19 July, there is erroneous fog residing along the Reykjanes peninsula in the simulation without data assimilation, leading to a temperature underestimation of 8 K. This error is almost eliminated by assimilating the SUMO data. An example of the impact on the horizontal extent of the sea breeze front from the data assimilation can be seen in Figure 6. The figure shows the near surface humidity field at 1600 UTC on 19 July, 2009. It

is clearly seen how the sea breeze front reaches farther inland with than without the data assimilation, which is in closer agreement with the observations. We find that both the assimilation of the temperature and humidity data as well as the wind data are important for the quality of the simulation results. Potential future applications for the SUMO FDDA system include the improvement of high resolution weather now- and forecasts for search and rescue missions.

5 Future Perspectives and Outlook

Studies of local- and mesoscale flow over the greater Bergen area in southwestern Norway, as presented in Papers 1 and 2, could in future include simulations with idealised flow. In this way, we would gain a more conceptual understanding of the processes studied. One of the remaining questions is the role of static stability in creating the Bergen orographic wind shelter. More observations could also prove useful for future studies. As of June 2012, there are data available from a scanning wind lidar temporarily mounted on the roof of the Geophysical Institute in Bergen (at the Florida weather station). These data are complimented by a rapidly growing network of AWSs in the area. Simulations and observations could also be used for the study of meteorological conditions during events of high concentrations of pollutants in the Bergen valley. Such issues typically arise during clear weather in wintertime when strong inversions build up in the valley (e.g. Berge and Hassel, 1984; Bergen-Kommune, 2007).

In Paper 2, we run a set of numerical sensitivity tests with higher resolution model datasets for landuse and topography. Our results show no consistent improvement when applying the high resolution datasets for the two studied cases of southwesterly wind storms. Previous studies have shown a larger improvement (e.g. Cheng and Byun, 2008; Arnold et al., 2012) when using such datasets. Our results could be sensitive to the larger scale flow. Cheng and Byun (2008) found a larger positive effect from an improved landuse dataset for weak synoptic flow, rather than for strong synoptic flow. The study of Paper 4 highlighted the need for a more accurate dataset for southwestern Iceland as the default dataset in WRF from the United States Geological Service (USGS) contains far too much inland water. The excessive surface water amounts caused negative temperature biases of several degrees in the affected locations. Work is currently being done on the implementation of a higher resolution and newer dataset for Iceland, called Corine (from the European Space Agency). This is a part of the high resolution landuse dataset that was used for Norway in Paper 2. Future climates are predicted to bring about land surface changes such as the melting of glaciers. In Iceland, smaller glaciers may disappear during the next 200 years (Jóhannesson, 1997). Such land coverage changes may have impacts on the regional climate, such as the altering of mesoscale flow over previously ice covered mountains. In Paper 3, we show that the removal of the ice cap from the Hofsjökull mountain in Central Iceland, leaving a rougher and warmer surface, has

a detrimental impact on the formation of gravity waves and downslope accelerated flow. Such changes in mountain flow patterns will in turn change the drag exerted on the atmosphere by the mountain. This may have implications for the general atmospheric circulation; orographic drag is an important sink in the atmospheric momentum budget (e.g. Lilly, 1972; Wahr and Oort, 1984).

Validation and provision of data for initialising and forcing numerical weather models, become increasingly challenging tasks as the model grid resolutions increase. In Papers 3 and 4, we confirm the utility of the SUMO RPAS for validating and forcing the WRF model. In the future, the utility of SUMO and similar systems is expected to expand significantly. As with RPASs in general, SUMO is a novel system under constant development. Recently, a five-hole probe that can measure the turbulent components of the u, v and w flow components, was incorporated in the system. The turbulence probe has already shown promising results from field campaigns in Denmark and France, in 2011 (Reuder et al., 2012). In Denmark, the system was flown in and around a small wind farm. The measurements revealed distinct differences in the turbulence kinetic energy (TKE) up- and downstream of the farm. In this context, the RPAS is a unique system in terms of flexibility and no other instrument platform can, to our knowledge, perform in-situ measurements with similar spatial and temporal resolution.

There is a rapidly increasing demand for energy in the world and renewable energy in the form of e.g. wind energy is foreseen to have a great potential. Planning of wind farms demands an in-depth knowledge of the surrounding areas. Especially in complex terrain, typical of Norway and Iceland, knowledge of the effects on the local flow field from both the surrounding and larger scale topography, as investigated in Papers 1-3, can prove essential. In this context, modelling tools are important. Liu et al. (2011) proposed a system in which very high resolution LES is combined with observations using FDDA for simulation of flows in wind farms. Measurements from SUMO and similar RPASs, both for validation and assimilation, would be ideal for such a system. The findings on wind speed distributions in Paper 1 could also be useful for future planning of wind farms. Mapping of wind speed distributions are frequently used in connection to wind energy. Generally, steady and moderate wind speeds are desirable for the extraction of wind energy.

Accurate prediction of local weather is key for a wide range of services and decision makers, such as search and rescue organisations. As proposed by Rögnvaldsson (2011), the improvement of weather forecasts or nowcasts for search and rescue purposes is a potential future application for the SUMO FDDA system, that we present in Paper 4. Search and rescue (SAR) missions are highly dependent on accurate weather information as the safety of people in the field must be secured, and the missions must be run as efficiently as possible. SAR missions often take place in remote areas and / or areas severely affected by natural hazards. RPASs, such as SUMO therefore represent an ideal platform for the provision of in-situ data from these areas.

Lessons learned from high resolution numerical case simulations can be useful guid-

ance for forecasters. Many flow phenomena, especially those connected to complex topography, are not appropriately resolved or represented by today's numerical weather prediction models as these are generally run at coarser resolutions (on the order of kilometres). These phenomena include mountain waves and wakes as studied in this thesis, and effects of sub-grid topography as discussed by Zardi and Rotach (e.g. 2007).

References

Ágústsson, H. and H. Ólafsson, 2004: Mean gust factors in complex terrain. *Meteorologische Zeitschrift*, **13 (2)**, 149–155.

Ágústsson, H. and H. Ólafsson, 2009: Forecasting wind gusts in complex terrain. *Meteorol. Atmos. Phys.*, **103**.

Ágústsson, H. and H. Ólafsson, 2012: The bimodal downslope windstorms at kvísker. *Meteorology and Atmospheric Physics*, **116**, 27–42.

Andersen, F., 1975: Surface winds in southern Norway in relation to prevailing H. Johansen weather types. *Meteor. Ann.*, **6 (14)**, 377–399.

Anthes, R., 1974: Data assimilation and initialization of hurricane prediction models. *J. Atmos. Sci.*, **31**, 702 – 718.

Arnold, D., I. Schicker, and P. Seibert, 2012: Towards high-resolution environmental modelling in the alpine region. *NATO Science for Peace and Security Series C: Environmental Security*, **14**, 269–273.

Barstad, I. and S. Grønås, 2005: Southwesterly flows over southern Norway-Mesoscale sensitivity to large-scale wind direction and speed. *Tellus 57A*, 136–152.

Barstad, I. and S. Grønås, 2006: Dynamical structures for southwesterly airflow over southern Norway: the role of dissipation. *Tellus 58A*, 2–18.

Berge, E. and F. Hassel, 1984: An investigation of temperature inversions and local drainage flow in Bergen, Norway (in Norwegian). *Meteorological report series, University of Bergen.*

Bergen-Kommune, 2007: Action plan for better air in Bergen (In Norwegian). *report*, 74, ISBN 978-82-7827-001-1.

Bjerknes, J. and H. Solberg, 1921: Meteorological conditions for the formation of rain. *Geofys. Publ.*

Bjerknes, J. and H. Solberg, 1922: Life cycles of cyclones and polar front theory of the atmospheric circulation. *Geofys. Publ*, **3 (1)**, 1–18.

Brisset, P., A. Drouin, M. Gorraz, P. Huard, and J. Tyler, 2006: The Paparazzi Solution. Http://www.recherche.enac.fr/paparazzi/papers_2006/mav06_paparazzi.pdf, http://www.recherche.enac.fr/paparazzi/papers_2006/mav06_paparazzi.pdf.

Bromwich, D. H., L. Bai, and G. G. Bjarnason, 2005: High-Resolution Regional Climate Simulations over Iceland Using Polar MM5. *Mon. Wea. Rev.*, **133**, 3527 – 3547.

Cascella, G., 2008: Identifying the Inner-Core Characteristics of Hurricane Noel (2007) via the Unmanned Aerial Vehicle, the Aerosonde. *Conference on Hurricanes and Tropical Meteorology, American Meteorological Society.*

Cassano, J. and S. Knuth, 2010: UAV observations of the wintertime boundary layer over the Terra Bay Polynya. *European Geosciences General Assembly, Vienna.*

Cheng, F.-Y. and D. W. Byun, 2008: Application of high resolution landuse and land cover data for atmospheric modeling in the HoustonâĂŞGalveston metropolitan area, Part I: Meteorological simulation results. *Atmospheric Environment*, **42**, 7795âĂŞ7811.

Curry, J. A., J. Maslanik, G. Holland, and J. Pinto, 2004: Applications of Aerosondes in the Arctic. *Bull. Amer. Meteor. Soc.*, **85 (12)**, 1855–1861.

Doyle, J. D., 1997: The influence of mesoscale orography on a coastal jet and raindband. *Mon. Weather Rev.*, **125**, 139–158.

Durran, D. R., 1990: Mountain waves and downslope winds. *in Atmospheric processes over complex terrain*, 59–81, ed. W. Blumen. American Meteorological Society. Boston. USA.

Foldvik, A., 1962: Two-Dimensional Mountain Waves - A Method for the Rapid Computation of Lee Wavelenghts and Vertical Velocities. *Quart. J. Roy. Metorol. Soc.*, **88**, 271–285.

Fuentes, M., L. Chen, J. M. Davis, and G. M. Lackmann, 2005: Modeling and predicting complex space-time structures and patterns of coastal wind fields. *Environmetrics*, **16**, 449–464.

Georgelin, M., E. Richard, M. Petitdidier, and A. Druilhet, 1994: Impact of Subgrid-Scale Orography Parameterization on the Simulation of Origraphic FLows. *Mon. Wea. Rev.*, **122**, 1509–1522.

Gill, A. E., 1982: Atmosphere-Ocean Dynamics. 662.

Godske, C., T. Bergeron, J. Bjerknes, and R. Bundgaard, 1957: Dynamic meteorology and weather forecasting. 800.

Grubišić, V. and I. Stiperski, 2009: Lee-Wave Resonances over Double Bell-Shaped Obstacles. *J. Atmos. Sci*, **66**, 1205–1228.

Harstveit, K., 2006: Mapping of extreme wind conditions in Bergen kommune (in Norwegian). *met.no report*, **3**, 55pp.

Holland, G. J., T. McGeer, and H. Youngren, 1992: Autonomous Aerosondes for Economical Atmospheric Soundings Anywhere on the Globe. *Bull. Amer. Meteor. Soc.*, **73 (12)**, 1987–1998.

Hunt, J. C. R. and K. J. Richards, 1984: Stratified airflow over one or two hills. *Bound.-Lay. Meteorol.*, **30**, 223–229.

Jóhannesson, T., 1997: The response of two Icelandic glaciers to climatic warming computed with a degree-day glacier mass-balance model coupled to a dynamic glacier model. *Journal of Glaciology*, 321–327.

Jonassen, M. O., 2008: The Small Unmanned Meteorological Observer (SUMO) - Characerization and test of a new meaurement system for atmospheric boundary layer research. *Master's thesis. Geophysical institute, University of Bergen. http://web.gfi.uib.no/forskning/Master/Master_ Jonassen.pdf.*

Konrad, T., M. Hill, J. Rowland, and M. J.H., 1970: A small, radio-controlled aircraft as a platform for meteorological sensors. *Applied Physics Laboratory Technical Digest*, **11**, 11–19.

Lilly, D. K., 1972: Wave momentum flux - A GARP problem. *Bull. Amer. Meteor. Soc.*, **53**, 17–23.

Lin, Y.-L., 2007: Mesoscale dynamics. 646.

Lin, Y.-L. and T.-A. Wang, 1996: Flow regimes and transient dynamics of two-dimensional flow over an isolated mountain ridge. *J. Atmos. Sci.*, **53**, 139–158.

Liu, Y., et al., 2011: Simultaneous nested modeling from the synoptic to the LES scale for wind energy applications. *J. Wind Eng. Ind. Aerodyn.*, **99**, 308 – 319.

Lyra, G., 1943: The theory of stational lee wave flow in the free atmosphere (in German). *Z. Angew. Math. Mech.*, **23**, 1–28.

Martin, S., J. Bange, and F. Beyrich, 2011: Meteorological profiling of the lower troposphere using the reaserch UAV "M2AV Carolo". *Atmos. Meas. Tech.*, **4**, 705 – 716.

Mayer, S., G. Hattenberger, P. Brisset, M. O. Jonassen, and J. Reuder, 2012: A 'no-flow-sensor' wind estimation algorithm for Unmanned Aerial Systems. *Int. J. Micro Air Vehicles*, **4**, 15–29.

Ólafsson, H. and H. Ágústsson, 2009: Gravity wave breaking in easterly flow over Greenland and associated low level barrier- and reverse tip-jets. *Meteorol. Atmos. Phys.*, **104**, 191–197.

Ólafsson, H. and P. Bougeault, 1996: Nonlinear Flow Past an Elliptic Mountain Ridge. *J. Atmos. Sci.*, **53**, 2465–2489.

Ólafsson, H. and P. Bougeault, 1997: The Effect of Rotation and Surface Friction on Orographic Drag. *J. Atmos. Sci.*, **54 (2)**, 193–210.

Overland, J. E. and N. Bond, 1993: The Influence of Coastal Orography: The Yakutat Storm. *Mon. Weather Rev.*, **121**, 1388–1397.

Parish, T. R., 1982: Barrier winds along the Sierra Nevada Mountains. *J. Appl. Meteor.*, **21**, 925–930.

Peng, M. S., S.-W. Li, S. W. Chang, and R. T. Williams, 1995: Flow over mountains: Coriolis force, transient troughs and three dimensionality. *Q. J. R. Meteorol. Soc.*, **121**, 593–613.

Petersen, G. N., H. Ólafsson, and J. E. Kristjánsson, 2005: The effect of upstream wind direction on atmospheric flow in the vicinity of a large mountain. *Q. J. R. Meteorol. Soc.*, **131**, 1113–1128.

Pielke, R. A., 2002: Mesoscale meteorological modeling. 676.

Pierrehumbert, R. and B. Wyman, 1985: Upstream effects of mesoscale mountains. *J. Atmos. Sci.*, **42**, 977–1003.

Queney, P., 1948: The problem of air flow over mountains: A summary of theoretical studies. *Bull. Am. Meteorol. Soc.*, **29**, 16–26.

Ramanathan, V., M. V. Ramana, G. Roberts, K. Dohyeong, C. Corrigan, C. Chung, and D. Winker, 2007: Warming trends in Asia amplified by brown cloud solar absorption. *Nature*, **448**, 575–578.

Raymond, D. J., 1972: Calculation of Airflow Over an Arbitrary Ridge Including Diabatic Heating and Cooling. *J. Atmos. Sci.*, **62**, 837–843.

Renfrew, I. A., S. D. Outten, and G. W. K. Moore, 2009: An easterly tip jet off Cape Farewell, Greenland. I: Aircraft observations. *Q. J. R. Meteorol. Soc.*, **135**, 1919–1933.

Reuder, J., P. Brisset, M. O. Jonassen, M. Müller, and S. Mayer, 2009: The Small Unmanned Meteorological Observer SUMO: A new tool for atmospheric boundary layer research. *Meteor. Z.*, **18**, 141 – 147.

Reuder, J., M. O. Jonassen, and H. Ólafsson, 2012: The Small Unmanned Meteorological Observer SUMO: Recent developments and applications of a micro-UAS for atmospheric boundary layer research,. *Acta Geophys.*, doi: 10.2478/s11600-012-0042-8.

Reuder, J., et al., 2011: FLOHOF 2007: An overview of the mesoscale meteorological field campaign at Hofsjökull, Central Iceland. *Meteorol. Atmos. Phys.*, DOI: 10.1007/s00 703–010–0118–4.

Richard, E., P. Mascart, and E. C. Nickerson, 1989: The Role of Surface Friction in Downslope Windstorms. *J. Appl. Meteor.*, **28**, 241–251.

Rögnvaldsson, O., 2011: Search and rescue, Weather prediction system assists huminatarian aid. *Meteorological technology international*, 76 – 78.

Rögnvaldsson, O., H. Ágústsson, E. M. Einarson, H. Ólafsson, H. Björnsson, and O. G. B. Sveinsson, 2007: Status report for year one of the RAV project (In Icelandic). Http://thjarkur.orkugardur.is/wordpress/wp-content/uploads/RAVarsskyrsla2007.pdf.

Rögnvaldsson, O., J.-W. Bao, H. Ágústsson, and H. Ólafsson, 2011: Downslope windstorm in Iceland âĂŞ WRF/MM5 model comparison. *Atmospheric Chemistry and Physics*, **11**, 103–120.

Sawyer, J. S., 1960: Numerical Calculation of the Dsiplacements of a Stratified Airstream Crossing a Ridge. *Quart. J. Roy. Metorol. Soc.*, **86**, 326–345.

Schroeder, A. J., D. R. Stauffer, N. L. Seaman, A. Deng, A. M. Gibbs, G. K. Hunter, and G. S. Young, 1990: Mountain Waves and Downslope Winds. *Meteorological Monographs*, **23**, 59–81.

Scorer, R. S., 1949: Theory of waves in the lee of mountains. *Quart. J. R. Met. Soc.*, **75**, 41–56.

Sinclair, M. R., D. S. Wratt, R. D. Henderson, and W. R. Gray, 1996: Factors Affecting the Distribution and Spillover of Precipitation in the Southern Alps of New Zealand - A Case Study. *J. Appl. Meteor.*, **36**, 428–442.

Skamarock, W. C., et al., 2008: A description of the Advanced Research WRF Version 3. *NCAR Tech. Note*, **TN-475+STR**, 125.

Smith, C. M. and E. D. Skyllingstad, 2011: Effects of Inversion Height and Surface Heat Flux on Downslope Windstorms. *Mon. Wea. Rev.*, **139**, 3750–3764.

Smith, R. B., 1979: The Influence of Mountains on the Atmosphere. *Advances in Gephysics, Academic Press, Inc.*, **21**, 87–230.

Smith, R. B., 1989: Mountain-induced stagnation points in hydrostatic flow. *Tellus 41A*, 270–274.

Smith, R. B. and S. Grønås, 1993: Stagnation points and bifurcation in 3-D Mountain flow. *Tellus 45A*, 28–43.

Spinnangr, F., 1943a: Synoptic studies on precipitation in southern norway. i instability showers. *Meteor. Ann.*, 323–356.

Spinnangr, F., 1943b: Synoptic studies on precipitation in southern norway. ii front precipitation. *Meteor. Ann.*, 433–468.

Stauffer, D. R. and N. L. Seaman, 1990: Use of four-dimensional data assimilation in a limited-area mesoscale model. Part I: Experiments with synoptic-scale data . *Mon. Wea. Rev.*, **118**, 1250 – 1277.

Stauffer, D. R. and N. L. Seaman, 1994: Multiscale Four-Dimensional Data Assimilation. *J. Appl. Meteor.*, **33**, 416 – 434.

Steensen, B. M., H. Ólafsson, and M. O. Jonassen, 2011: An extreme precipitation event in Central Norway. *Tellus 63A*, 675–686.

Stiperski, I. and V. Grubišić, 2011: Trapped Lee Wave Interference in the Presence of Surface Friction. *J. Atmos. Sci*, **68**, 918–936.

Thomas, R. M., K. Lehmann, H. Nguyen, D. L. Jackson, D. Wolfe, and V. Ramanathan, 2012: Measurement of turbulent water vapor fluxes using a lightweight unmanned aerial vehicle system. *Atmos. Meas. Tech.*, **5**, 243–257.

Thorsteinsson, S. and S. Sigurdsson, 1996: Orogenic blocking and deflection of stratified air flow on an f-plane. *Tellus 48A*, 572–583.

Trüb, J. and H. C. Davies, 1995: Flow over a mesoscale ridge: Pathways to regime transition. *Tellus 47A*, 502–524.

Van den Kroonenberg, A., T. Martin, M. Buschmann, and P. Bange, J. Vörsmann, 2008: Measuring the wind vector using the autonomous Mini Aerial Vehicle M2AV. *J. Atmos. Ocean. Technol.* , **25**, 1969 – 1982.

Wahr, M. J. and A. H. Oort, 1984: Friction- and Mountain-Torque Estimates from Global Atmospheric Data. *J. Atmos. Sci.*, **41**, 190–204.

Wallington, C. E. and J. Portnall, 1958: A Numerical Study of the Wavelength and Amplitude of Lee Waves. *Quart. J. Roy. Metorol. Soc.*, **84**, 38–45.

Warner, T. T., 2011: Numerical Weather and Climate Prediction. *Cambridge University Press*, 526.

Wood, N., 2000: Wind flow over complex terrain: A historical perspective and prospect for large-eddy modelling. *Boundary-Layer Meteorol.*, 11–32.

Zardi, D. and M. W. Rotach, 2007: On the boundary-layer structure over highly complex terrain: Key findings from MAP. *Q. J. R. Meteorol. Soc.*, **133**, 937–948.

6 Appendix

In addition to the four papers included in this thesis, the author has contributed to the scientific peer reviewed papers listed below. The contribution has mainly been in the form of numerical simulations and corresponding pre- and post-processing as well as in-field collection of observational data.

- **The Small Unmanned Meteorological Observer SUMO: A new tool for atmospheric boundary layer research**
  Reuder, J., Brisset, P., **Jonassen, M. O.**, Müller, M. and Mayer, S. (2009)
  Meteorologische Zeitschrift, **18**, pp. 141−147

- **An extreme precipitation event in Central Norway**
  Steensen, B. M., Ólafsson, H. and **Jonassen, M. O.** (2009)
  Tellus 63A, pp. 675−686

- **FLOHOF 2007: An overview of the mesoscale meteorological field campaign at Hofsjökull**
  Reuder, J., et al. (2011)
  Meteorology and Atmospheric Physics, DOI: 10.1007/s00 703−758 010−0118−4

- **A 'no-flow-sensor' wind estimation algorithm for Unmanned Aerial Systems**
  Mayer, S., Hattenberger, G., Brisset, P., **Jonassen, M. O.** and Reuder, J. (2012)
  International Journal of Micro Air Vehicles, **4**, pp. 15−29

- **Atmospheric profiling with the UAS SUMO: a new perspective for the evaluation of fine-scale atmospheric models**
  Mayer, S., Sandvik, A., **Jonassen, M. O.** and Reuder, J. (2012)
  Meteorology and Atmospheric Physics, DOI: 10.1007/s00703−010−0063-2

- **Profiling the Arctic Stable Boundary Layer in Advent Valley, Svalbard: Measurements and Simulations**
  Mayer, S., **Jonassen, M. O.**, Sandvik, A. and Reuder, J. (2012)
  Boundary Layer Meteorology, DOI: 10.1007/s10546−012−9709−6

- **The Small Unmanned Meteorological Observer SUMO: Recent Developments and Applications of a Micro-UAS for Atmospheric Boundary Layer Research**
  Reuder, J., **Jonassen, M. O.** and Ólafsson H. (2012)
  Acta Geophysica, DOI: 10.2478/s11600−012−0042−8

- **First results of turbulence measurements in a wind park with the Small Unmanned Meteorological Observer SUMO**
  Reuder, J. and **Jonassen, M. O.** (2012)
  Energy Procedia, 24, 176-185.

Paper 1

Multi-scale variability of winds in the complex topography of southwestern Norway

Jonassen, M. O., Ólafsson, H., Reuder, J. and Olseth, J. A. (2012)

Tellus 64A pp. 1−17

Tellus SERIES A DYNAMIC METEOROLOGY AND OCEANOGRAPHY
PUBLISHED BY THE INTERNATIONAL METEOROLOGICAL INSTITUTE IN STOCKHOLM

Multi-scale variability of winds in the complex topography of southwestern Norway

By MARIUS O. JONASSEN[1]*, HARALDUR ÓLAFSSON[1,2,3], JOACHIM REUDER[1] AND JAN A. OLSETH[1], [1]*Geophysical Institute, University of Bergen, Allegaten 70, Bergen, Norway*; [2]*Department of Physics, University of Iceland, Reykjavík, Iceland*; [3]*Icelandic Meteorological Office, Bustadavegi 9, IS-150 Reykjavík, Iceland*

(Manuscript received 1 April 2011; in final form 31 October 2011)

ABSTRACT

Multi-scale variability of winds in the complex terrain of southwestern Norway is investigated using up to 20 yr of observations from nine automatic weather stations and reanalysis data. Significant differences between the large- and local-scale winds are found. These differences are mainly governed by the large-scale topography of Southern Norway. Winds from the southeast and statically stable flow from the northwest are found to be significantly reduced at the ground level due to large-scale wake and blocking effects. Southwesterly and northeasterly winds are orographically enhanced. At a local scale, there are differences in the wind speed distributions between the surface stations, both in space and time. These differences can to a large extent be quantified in terms of the Weibull distribution function and associated with the respective geographical locations as discretised in four characteristic surface categories: offshore, inland, coast and mountain. The inland category is found to be associated with relatively low but variable wind speeds, whereas the coastal and offshore locations are dominated by more steady and stronger winds. The mountain wind speed distribution is fundamentally different from the others; it shares the variability with the inland locations but the higher average wind speed with the other categories.

Keywords: complex terrain, Southern Norway, flow modification, topography, local meteorology

1. Introduction

Along the southwest coast of Norway, southerly winds prevail throughout the year. On a timescale of days and weeks, however, the frequent passages of cyclones give rise to rapid and large changes, both in wind direction and wind speed. Of similarly great magnitude are the spatial differences found in smaller scale winds for a given large-scale flow. These differences are in first order governed by the larger scale topography of Southern Norway (approximately 100–150 km wide, 1500 m high), inducing phenomena that can be characterised as meso to synoptic-scale flow structures. At a local scale (1–50 km), the flow is modified by topographic features typical for the Norwegian coast such as steep mountains, valleys, narrow fjords, islands and straits. Also, contributing to the local-scale variability in winds are thermally driven flows such as land–sea breezes or valley and mountain winds. Meso to synoptic-scale flows over Southern Norway have been studied since the early days of the Bergen School of Meteorology (Bjerknes and Solberg, 1921, 1922). With an increased observational record, their findings later led to forecasting rules for different flow regimes. The findings were documented by Spinnangr (1943). Later, Andersen (1975) gave an overview of different wind patterns classified by periods of certain prevailing large-scale wind directions. In recent years, two papers have been published on the topic, Barstad and Grønås (2005), hereafter BG05) and Barstad and Grønås (2006). Using a series of idealised numerical simulations and reanalysis data along with ground observations, they studied flows over Southern Norway in the sector from south to west with emphasis on mesoscale flow structures. Among their main findings, was a jet forming along the mountain slopes and out over the sea (referred to as a 'left-side' jet) connected to southwesterly large-scale flow. In addition, lee side effects such as downslope-accelerated winds and a wind shadow connected to inertio-gravity waves were identified in southeasterly to southerly flow.

*Corresponding author.
email: marius.jonassen@gfi.uib.no

Citation: Tellus A 2012, **64**, 11962, DOI: 10.3402/tellusa.v64i0.11962

Under conditions with weak synoptic flow, thermally driven flows (flows driven by local temperature and pressure gradients) such as sea and land breezes, valley and mountain winds typically dominate on a local scale. In southwestern Norway, such local flow has mainly been studied in the Bergen valley and its surroundings. Berge and Hassel (1984) studied temperature inversions and local drainage flow in the Bergen valley using a tethered balloon and automatic weather stations (AWSs). They found the development of inversions to be most frequent in wintertime during periods with larger scale easterly (offshore) winds and high atmospheric stability. Utaaker (1995) studied the climate in Bergen, with the main emphasis on local winds and temperature conditions. He described a prominent channelling effect by the Bergen valley and a variation in dominating local wind directions with the time of the year, driven under weak synoptic flow to a large extent by sea breeze during summertime and katabatic winds during wintertime. An AWS at Flesland, some 10 km southwest of the centre of Bergen, was found to give the most representative picture of the wind field in the Bergen area as a whole.

In many ways, the southwest coast of Norway represents a physical barrier to the large-scale flow. In the aforementioned studies on such flow over southwestern Norway, this roughly north/south-oriented barrier has mainly been treated as a two phased one, with sea to the west and land/mountains to the east. Accordingly, this simplification has predominantly been used when describing flow regimes over the area (with one over land and one over sea). In this study, a more refined topography transition between sea and land is used, laterally dividing the coastal zone into four discrete surface categories: offshore, coastal, inland and mountain. By this new concept, the present study lays more emphasis on finer scales, allowing for a more detailed description of the flow over the southwest coast of Norway.

It is a main aim of this study to investigate the relationship between the large-scale flow, the aforementioned mesoscale flow structures and the flow at local scale. Previous studies on the relationship between the small- and large-scale flow in complex terrain, (e.g. Whiteman and Doran, 1993; Kalthoff et al., 2003) have found significant differences between the two but have not explicitly included mesoscale flow structures as those studied here. The present investigation is confined to a relatively limited area roughly covering the western/seaward half of the Hordaland county, centrally situated at the southwest coast of Norway (Fig. 1). The area is further on referred to as the 'Greater Bergen area'. The results will, amongst other things, provide a climatological frame for an ongoing project, where a very dense network of AWSs is being established in the central areas of Bergen. In addition, the results will be of general relevance for local-scale weather forecasting in the area and may give guidance for estimations of, for example dispersion of pollutants.

Up to 20 yr (1989–2009) of data from nine AWSs situated in a rough transect from offshore via the coast to the inland and the mountains are used. ERA Interim data from the European Centre for Medium-Range Weather Forecasts (ECMWF) are used to estimate the corresponding large-scale flow.

The second section of this paper is dedicated to a description of the data and theory.

Section 3 describes the results, section 4 presents a discussion of these and the main findings are summarised in the fifth and last section.

2. Data and theory

2.1. Atmospheric data

In the area of interest, i.e. the Greater Bergen area as defined in the introduction, a number of AWSs have been erected to provide information on the local climate. The AWS at Mount Ulriken is run in a collaboration between Aanderaa data instruments (AADI) and the Geophysical institute, University of Bergen (GFI), and the AWS at Sotra is run by Avinor. The remaining stations are operated by the Norwegian meteorological office (met.no). The geographical locations of the AWSs are indicated in Fig. 1, and key figures for each station are listed in Table 1. At Florida, the measurements are made on the top of the GFI building around 25 m above the surrounding ground. The wind speed there is, therefore, most likely somewhat higher than the typical 10 m reference value. The measurements offshore, i.e. at the platforms of Troll A and Gullfaks C, are also made at higher altitudes (approximately 70 and 77 m.a.s.l.).

For most of this study, the meteorological data are obtained as 10 minute averages every 6 hours, i.e. 0000, 0600, 1200 and 1800 UTC. Not all station data are available with a full 20 yr record. These inhomogeneities might have implications on the accuracy of, for example the calculations of the Weibull factors, as presented in Section 3, and more data in future records would be expected to yield more accurate estimations. The same holds for the wind ratios presented in the same section.

Following the concept given in the introduction, the AWSs are grouped into four categories according to their geographical locations, that is offshore, coast, inland and mountain. No regular upper air observations are made in the area; therefore, ECWMF ERA Interim 850 hPa reanalysis data (hereafter 'ERA Interim') from a point at 60°N 4.5°E are used to estimate the large-scale wind direction and wind speed. The ERA Interim data have a temporal resolution of 6 hours and a horizontal grid spacing of 1.5°.

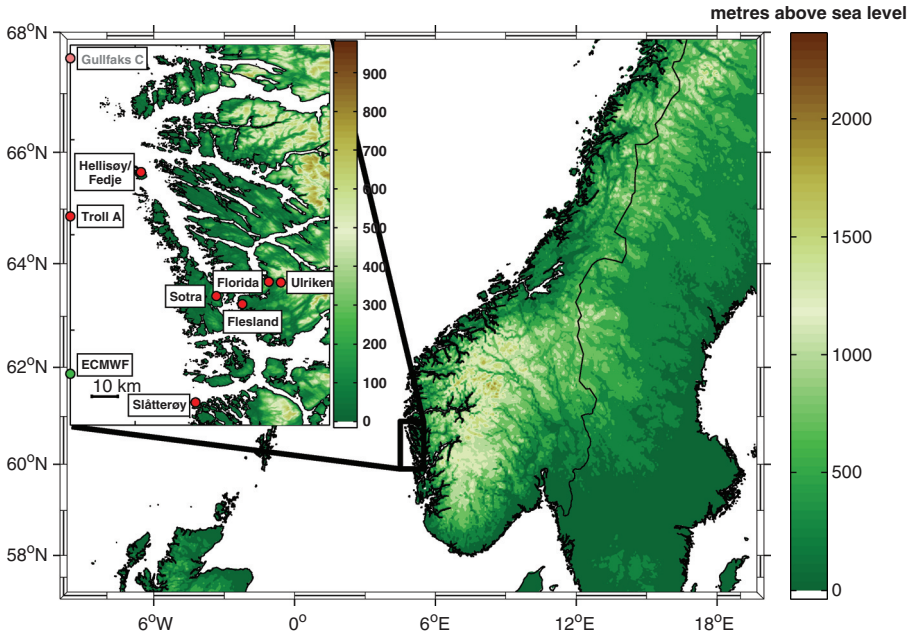

Fig. 1. Topography of Southern Norway with the area of main interest and the locations of the nine automatic weather stations. Gullfaks C is located some 80 km to the west of the indicated position. 'ECMWF' indicates the position from which the ECWMF reanalysis data are obtained.

2.2. *Theory*

2.2.1. Mountain flow. Rotunno and Ferretti (2001) list the following five central parameters in the theory of orographic flow modification (neglecting the effects of latent heat release): The typical wind speed of the background flow, U, the Coriolis force f, the Brunt–Väisälä frequency N, the obstacle (mountain) height h and L, a length scale commonly considered as the mountain half-width in the direction of the flow. The effect of these parameters are nicely summarised in Fig. 11 of their paper. The five parameters are often combined to form three different non-dimensional control parameters (e.g. Birkhoff, 1960): The non-dimensional mountain height (or inverse Froude number) Nh/U, the Rossby number U/fL and the hydrostatic number U/NL.

Table 1. Automatic weather stations

Station	Dates	Source	m.a.s.l.
Florida	1989–2009	met.no	48
Flesland	1989–2009	met.no	48
Ulriken	2005–2009	AADI/GFI	605
Sotra	2007–2010	Avinor	341
Hellisøy	1989–2005	met.no	20
Fedje	2004–2009	met.no	19
Slåtterøy	1989–2005	met.no	25
Troll A	1998–2009	met.no	Approximately 70
Gullfaks C	1990–2009	met.no	77
ERA Interim-850 hPa	1989–2009	ECMWF	N/A
ERA Interim-925 hPa	1989–2009	ECMWF	N/A
ERA Interim-10 m	1989–2009	ECMWF	N/A

For a linear, stratified flow over a mountain on a frictionless, non-rotating plane, the main parameter governing the flow is Nh/U (Pierrehumbert and Wyman, 1985). In the literature, various flow regimes based on this parameter are described (e.g. Peng et al., 1995; Triib and Davies, 1995; Lin and Wang, 1996; Ólafsson and Bougeault, 1996). Smith (1989) outlined three main flow regimes over simple 3-D mountains: Low values of Nh/U enable the flow to pass over the mountain without any stagnation, and typically gentle gravity waves are formed. Nh/U can be seen as a measure of the non-linearity in the flow, and linear theory describes the response well in this range (Gill, 1982). For high values of Nh/U, the flow may stagnate on the upstream side of the mountain, and this is the most common pattern for high mountain ranges. On a non-rotating plane, for a mountain that is elongated along the flow, stagnation starts at values of Nh/U that are higher than if the mountain is elongated across the flow (Smith, 1989). This has been confirmed by Bauer et al. (2000), using 3-D numerical simulations. Neglecting the effects of rotation, westerly flow should in other words be more easily blocked than southerly flow, both impinging on a

mountain with the shape of Southern Norway (north–south elongated).

The Rossby number enters the theory as an additional parameter for flow on a rotating plane. As the flow impinges on the mountain, it is decelerated by the buildup of a pressure surplus on the upstream side created below the air that is cooled off through adiabatic ascent as it is forced to climb the mountain. The deceleration causes a net force imbalance in the initially geostrophic flow leading more of the flow towards the left of the mountain (in the northern hemisphere). This effect is well described in the literature (e.g. Smith, 1982; Pierrehumbert and Wyman, 1985). Rotation, thereby, may render flow that would be blocked on a rotating plane, unblocked (Thorsteinsson and Sigurdsson, 1996; Ólafsson and Bougeault, 1997). The effect of the mountain aspect ratio on a rotating plane is the opposite of that for a non-rotating plane. For Southern Norway, it facilitates the westerly flow but not the southerly flow to overcome the blocking (Petersen et al., 2005). Finally, smaller scale topography impacts the flow on scales, where the Coriolis force is negligible and at these scales the flow may be blocked locally.

The intensity of upstream blocking critically depends on the ambient static stability that can modulate the magnitude and direction of the low-level flow impinging on the orography (e.g. Smith, 1979; Smolarkiewicz and Rotunno, 1989, 1990). For strong atmospheric stratifications and through the above-described effect of rotation, left-bound barrier jets often form in connection to larger mountain ranges. They may be associated with cold air damming effects, as investigated by, for example Bell and Bosart (1998) for flow near the Appalaches and flow with high Nh/U as discussed by Pierrehumbert and Wyman (1985) and Overland and Bond (1993). Such jets are typically found along larger mountain ranges as the Rocky Mountains (Colle and Mass, 1995), the Appalaches (Bell and Bosart, 1998) and along mountainous coastal regions as those of Southern Norway (BG05), California (Doyle, 1997), Alaska (Overland and Bond, 1993) and Greenland (Ólafsson and Ágústsson, 2009; Renfrew et al., 2009). The terrain is the forcing element of the flow, so such jets are normally confined below the mountain peaks (Parish, 1982, BG05).

For Southern Norway, L varies between 100 km (westerly flow) and 250 km (southerly flow). This corresponds to a length scale found within the meso range. Typical wind speeds in the region are in the range 5–20 m s^{-1}, and the characteristic mountain height is around 1500 m. This would yield a typical Rossby radius from 0.15 to 0.65 for southerly/northerly winds and from 0.4 to 1.65 for westerly/easterly winds (BG05). These values are in the so-called intermediate range (e.g. Triib and Davies, 1995), where perturbations take the form of inertia buoyancy waves for R_0 slightly above 1 and pseudo-geostrophic waves for R_0 slightly below 1 (Pierrehumbert and Wyman, 1985).

2.2.2. Wind speed distribution. Wind speed distributions have successfully been approximated by the Weibull probability density function (e.g. Justus and Mikhail, 1976; Hennessey, 1977; Pavia and O'Brien, 1986; Wei, 2010). The function can be expressed as follows:

$$f(x) = \begin{cases} \frac{k}{\lambda}\left(\frac{x}{\lambda}\right)^{k-1} e^{-(x/\lambda)^k} & x \geq 0 \\ 0 & x < 0 \end{cases}$$

f(x) gives the probability that a random observation has a value equal to x. $k > 0$ is the shape parameter and $\lambda > 0$, the scale parameter. k is dimensionless and λ has the units m s^{-1}. In short, the shape parameter k is a measure of the variability in wind speed.

The wind speed distribution in areas with high diurnal variability, for example, areas often experiencing local thermally driven flow, will typically be associated with a low shape parameter (k-values below approximately 1.8). The same is generally valid for regions with complex terrain. A low shape parameter k also indicates a high prevalence of low wind speeds. Regions with a more stable wind climate, such as the trade wind belt, are generally characterised by a higher shape parameter (k-values around 3). The scale parameter λ is tightly linked to the average wind speed. A high scale parameter indicates a high average wind speed and vice versa.

The cumulative Weibull distribution function, giving the probability that a random observation has a value equal to or less than an assigned value x, can be expressed as follows:

$$F(x) = 1 - e^{-(x/\lambda)^k}$$

In this study, the scale and shape parameters are obtained through a maximum likelihood estimate. The calculations are based on 6 hourly data from the periods indicated in Table 1.

3. Results

3.1. Large-scale wind climatology

Looking at the wind distribution at 850 hPa derived from 20 yr of ERA Interim data (Fig. 2, a–e), it is clear that winds from the southeast through the westerly sector to the north are dominating. Winds from the east and northeast, on the other hand, are rare throughout the year. The highest wind speeds are generally found in the sector south to southeast. A seasonal variation is seen in both the wind direction and the wind speed. In the winter, the winds are more westerly than in the other seasons. The winter also has the highest wind speeds. The weakest winds are, as

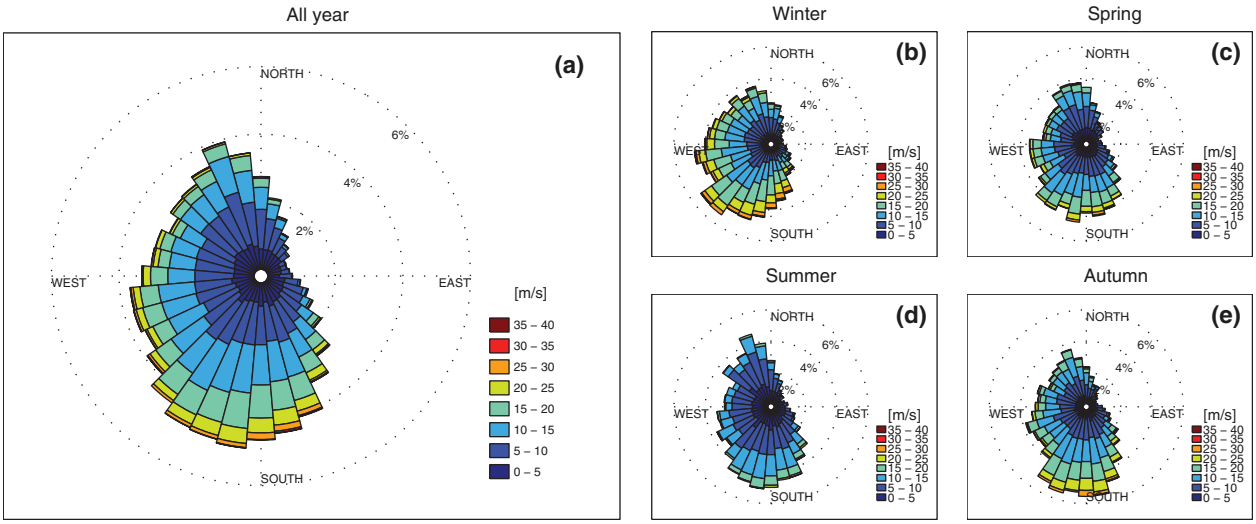

Fig. 2. Climatology of large-scale winds (ERA Interim 850 hPa at 60°N 4.5°E) for (a) all year, (b) the winter (December–January–February), (c) the spring (March–April–May), (d) the summer (January–July–August) and (e) the autumn (September–October–November).

expected, found in summertime. Furthermore, the summer season is associated with dominating large-scale winds from the south and a higher portion of northwesterly winds than the rest of the year.

3.2. *Frequency of wind directions*

Figure 3 shows the relative frequency of occurrence of different wind directions at the selected AWSs. It appears that the most common wind direction at the ground level in the area is south-southeast. Similar to the flow at 850 hPa, winds at the ground level from east and northeast are rare. Although somewhat more frequent offshore (observations of wind direction at Gullfaks C are missing) and aloft, westerly winds are also generally rare. Close to 25% of the strong winds at Florida are south-southeasterly (150–170°), making it the single most common wind direction at any of the included locations. Undoubtedly, this is caused by a channelling through the Bergen valley. The second most dominating wind direction in the area is northerly (around 340°).

When excluding data corresponding to local wind (winds observed at each station) speeds below 10 m s^{-1} (Fig. 4), one can see where the stronger winds come from. The south-southeasterly peak in wind direction distribution at Florida becomes even more pronounced, now accounting for close to 50% of the observations (although this is a rare event, see Fig. 6). The same effect is seen at Flesland. Also, the majority of the other stations report a significantly higher portion of wind speeds from the south for this higher wind speed threshold. A significant increase in relative frequency is also seen for northerly winds at most stations. Together with the increase in frequency of southerly winds, this indicates a stronger alignment to the coastline and general topography in the area for strong winds. Winds from the east and northeast of this magnitude are almost absent at all stations, with one notable exception, around 5% of the winds at Florida are easterly (100°).

3.3. *Frequency of wind speeds*

From the fitted Weibull distribution of wind speeds for the chosen AWSs (Fig. 5), a relatively close resemblance is found within each of the four location categories in Table 2. In terms of the Weibull shape parameter (k) and scale parameter (λ), as listed in Table 2, the inland locations are associated with a comparably low λ value (around 4) and a k ranging between 1.56 (Flesland) and

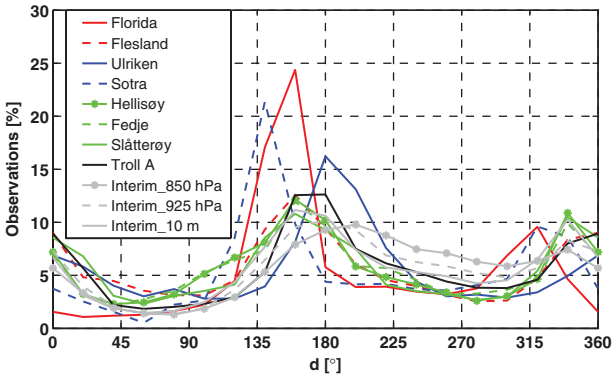

Fig. 3. Distribution of wind direction, d (°), at the chosen surface stations and ERA Interim data in Table 1 for all local wind speeds. Wind direction data from Gullfaks C are missing.

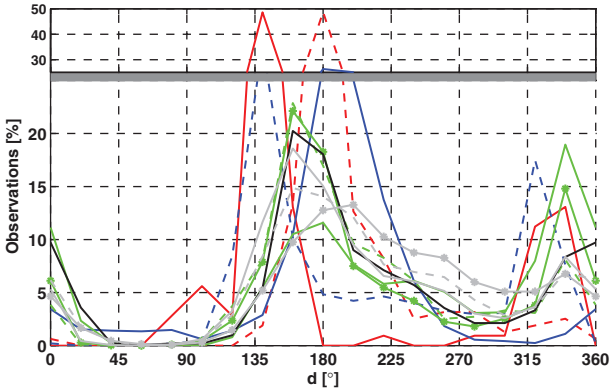

Fig. 4. Same as in Fig. 3 but for local wind speeds above 10 m s^{-1}. The thick, horizontal line at 25% corresponds to a change of scale in the y-axis. The change in scale is done to make the results below the line directly comparable to the results in Fig. 3.

1.74 (Florida). The coastal and offshore stations, on the other hand, have larger λ values ranging from 7.29 (Slåtterøy) to 9.31 (Gullfaks C), or roughly twice that of the inland stations, and so are their mean and median wind speeds (7–8 m s^{-1}, not shown). These stations' *k* values are also higher, around 2. The *k* and λ values for the stations at Mount Ulriken and Sotra appear as a combination of those from the three other categories: The *k* values are relatively low, similar to those at the inland stations, whereas the λ values are high, more similar to those found offshore and at the coast. In the case of Ulriken, the lower shape parameter corresponds to a higher frequency of wind speeds below 2 m s^{-1}, lower frequency of wind speeds between 2 and 15 m s^{-1} and a higher frequency of wind speeds exceeding 15 m s^{-1} when compared to the observations offshore and at the coast.

According to the cumulative Weibull distribution of winds (Fig. 6), showing the probability of having a wind speed equal to or less than a certain threshold (*x*-axis), only about 1% of the winds at the inland location of Florida exceed 10 m s^{-1}. This is significantly lower than that for, for example, Hellisøy/Fedje that is freely exposed to the North Sea, with a corresponding number of around 30%. At Mount Ulriken, around 25% of the winds are above 10 m s^{-1} and 2% above 20 m s^{-1}.

3.4. *Seasonal and diurnal variations in wind speed*

Figure 7 shows that the highest wind speeds are found during wintertime and the lowest during summertime. The overall strongest diurnal variations in wind speed are seen at the inland stations during summertime. In that season, the lowest wind speeds occur during night-time, whereas the highest ones are found around midday. A somewhat weaker diurnal variability in wind speeds is seen for the coastal stations. At the stations offshore, there is hardly any diurnal variability at any time of the year.

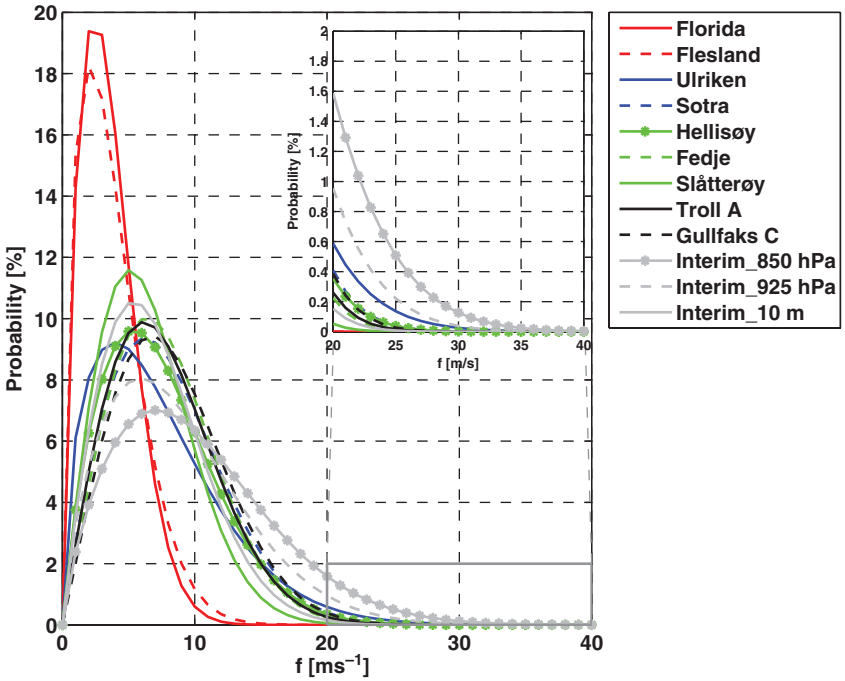

Fig. 5. Fitted Weibull distributions of wind speeds, f (m s^{-1}), for the chosen surface stations and the ERA Interim data. The inserted panel (upper right corner) shows the upper tails of the distributions (wind speeds above 20 m s^{-1}) in more detail.

Table 2. Weibull shape and scale factors for the wind speed distribution at each station. The factor estimations are based on 6 hourly data from the respective data periods stated in Table 1

Station name	Location category	scale, λ [m s^{-1}]	Shape, k
Florida	Inland	3.99	1.74
Flesland	Inland	4.13	1.56
Ulriken	Mountain	8.03	1.48
Sotra	Mountain	8.4	1.81
Hellisøy	Coast	8.98	1.93
Fedje	Coast	8.79	2.08
Slåtterøy	Coast	7.29	1.94
Troll A	Offshore	8.68	2.00
Gullfaks C	Offshore	9.31	2.07
ERA Interim-850 hPa	Model	11.36	1.77
ERA Interim-925 hPa	Model	9.79	1.73
ERA Interim-10 m	Model	7.91	1.92

3.5. *Surface winds and the large-scale flow*

A question of central interest is how the local wind speed at the ground level varies with the large-scale flow. From the theory on mountain flow, as described in Section 2.2, this relationship is expected to mainly depend on the large-scale wind speed and wind direction and the atmospheric stability.

As a step towards answering the posed question, a wind ratio is introduced, defined as the median of the ratio between the local and larger scale wind speed:

$$\text{median}(\text{AWS\_wind}/850\text{hPa\_wind}) \quad (1)$$

Situations with 850 hPa wind speeds below 5 m s^{-1} and or with less than 20 cases are excluded from the calculations. Wind ratios are also calculated for model data at 925 hPa and 10 m above ground. The sensitivities of the wind ratio to the Nh/U, N and U have similarly been investigated by calculating the wind ratios for two different intervals of each parameter. The intervals are divided by high and low values of each parameter, and the differences in wind ratios between them correspond to the sensitivity.

In the calculations, h is set to the characteristic mountain height of Southern Norway, 1500 m. U is the average of the ERA Interim 850 hPa and 10 m wind speed and N, the Brunt–Väisälä frequency, is defined as follows:

$$N = \sqrt{\frac{g}{\theta_{\text{avg}}}\frac{d\theta}{dz}},$$

where g,θ and z are the acceleration of gravity, the potential temperature and the altitude. Δθ and Δz are the differences in θ and z between 850 hPa and the ground and θ_{avg} is the vertical average of θ below 850 hPa. The thickness of the atmospheric layer, Δz, is obtained from the hypsometric equation. A dry atmosphere is assumed in the calculations.

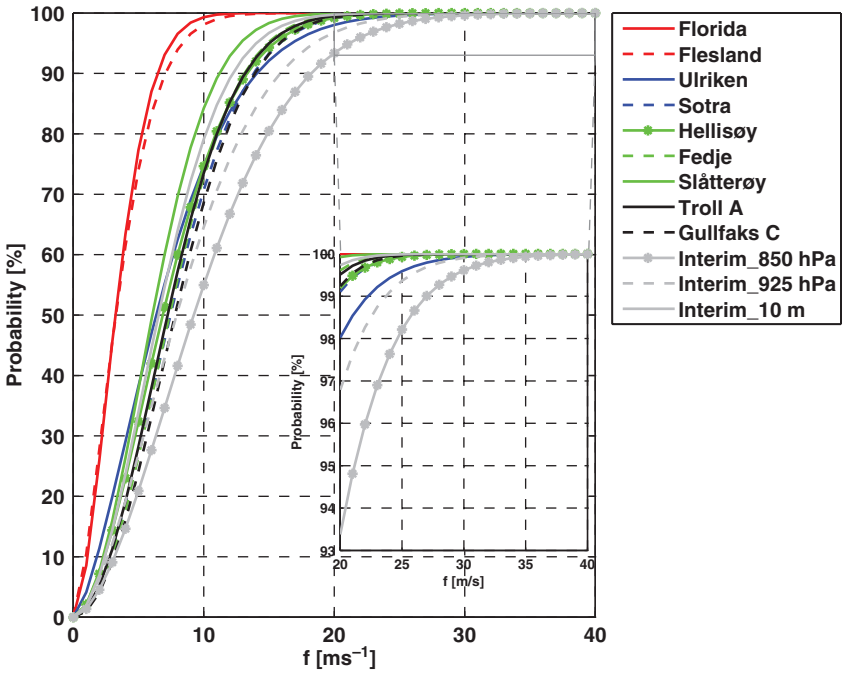

Fig. 6. Fitted cumulative Weibull distributions of wind speeds, f (m s^{-1}), for the chosen surface stations and the ERA Interim data. The inserted panel (at the right) shows the cumulative distributions for wind speeds above 20 m s^{-1} in detail.

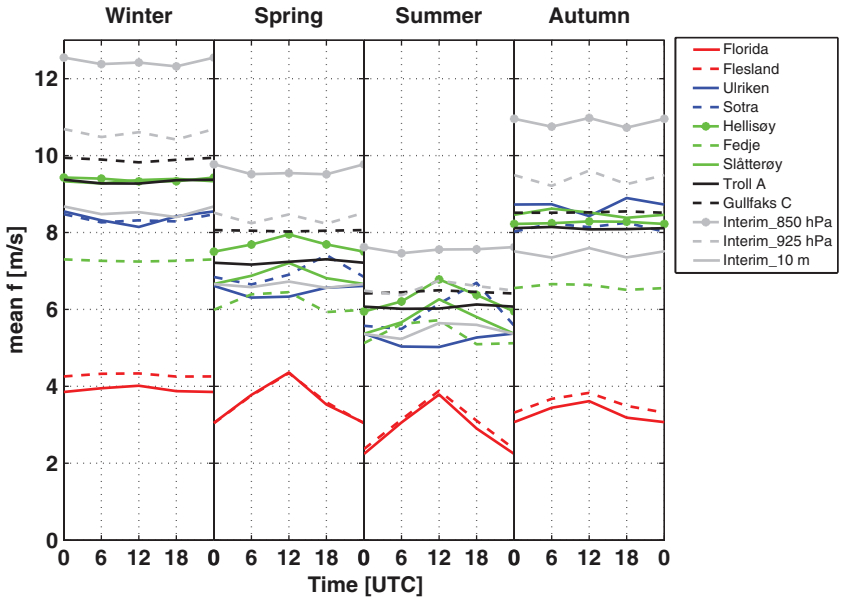

Fig. 7. Seasonal and diurnal variation in wind speed, f ($m\,s^{-1}$), for the chosen surface stations and the ERA Interim data.

The two different intervals of Nh/U are defined as follows: equal to or higher Nh/U than for 75% of all data ($Nh/U \geq 2.4$) and equal to or lower Nh/U than for 25% of all data ($Nh/U \leq 1.1$). The intervals for U are 5–10 $m\,s^{-1}$ and 10–15 $m\,s^{-1}$. For N, the two intervals are equal to or higher N than for 75% of all data ($N \geq 0.012\,s^{-1}$) and equal to or lower N than for 25% of all data ($N \leq 0.008\,s^{-1}$). In the context of N, only situations with 850 hPa winds in the range 10–15 $m\,s^{-1}$ are considered. This range is chosen to minimise the influence from variations in the ambient wind speed on the results and contains approximately 25% of the 850 hPa winds.

Figure 8 shows the wind ratio calculated over large-scale wind direction sectors of 20°. The corresponding results for the sensitivity of the wind ratio to Nh/U, U and N are presented in Figs. 9, 10 and 11.

The wind ratios reveal two distinct wind regimes, one connected to strong surface flow and another to weak surface flow. These are discussed separately in Section 3.5.1.

3.5.1. Strong surface flow: Large-scale winds from southwest and northeast. The, on average, highest wind ratios are found in connection to southwesterly flow. The response in the wind ratios to an increased Nh/U, as seen in Fig. 9 c, is on average higher wind ratios. Both U and N contribute to this increase as a decreased U (Fig. 10c) and an increased N (Fig. 11c) give higher wind ratios.

The second sector of relatively strong surface wind speeds is northeast. At the offshore stations, these maxima are, in fact, higher than in southwesterly flow. In contrast to, for example Flesland, Florida also observes relatively high wind speeds in this sector. Increasing Nh/U on average lowers the wind ratio for this wind sector (Fig. 9c) with contributions mainly from the static stability, N (Fig. 11c). The wind speed U works actively in the opposite direction (Fig. 10c). There are relatively few northeasterly cases, which is reflected by a large spread in wind ratios for this sector.

3.5.2. Weak surface flow: large-scale winds from northwest and southeast. In southeasterly large-scale flow, markedly

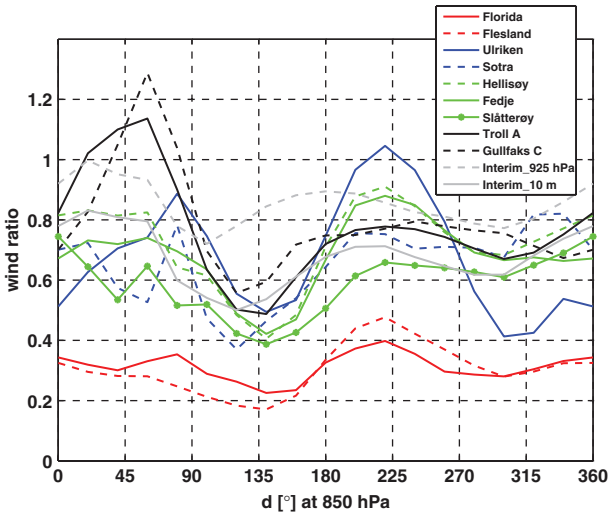

Fig. 8. Wind ratios for the surface stations and ERA Interim data as a function of the 850 hPa wind direction, d (°) for wind speeds at 850 hPa greater than 5 $m\,s^{-1}$.

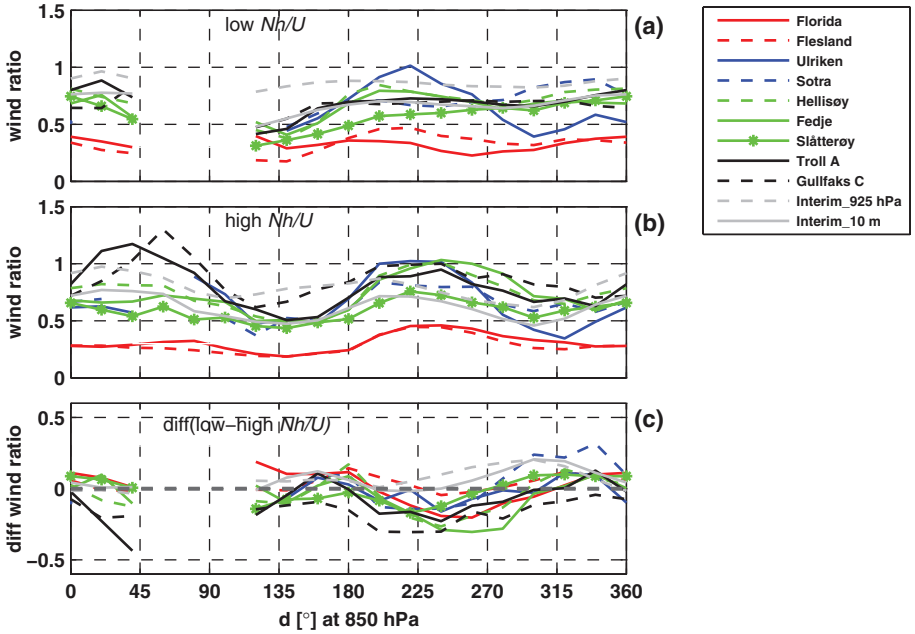

Fig. 9. Wind ratios for cases with (a) low Nh/U and (b) high Nh/U and (c) the difference between both (a) and (b) (see the text for the definition of low and high Nh/U).

reduced wind speeds are observed, not only at all surface stations but also at higher levels in the free atmosphere (ERA Interim 925 hPa data) (Fig. 8). The wind ratio appears on average quite insensitive to Nh/U and U for this wind sector.

Reduced wind speeds at the ground level are also found in large-scale flow from west and northwest. Increasing Nh/U gives, in general, lower wind ratios for this wind sector (Fig. 9c). The contributions are mainly from an increased N (Fig. 11c).

3.5.3. Wind direction. As expected from Ekman's theory, a general anti-clockwise shift in wind direction is seen at the ground locations when compared with the 850 hPa wind direction (Fig. 12). Deviations from the average shift of 20° are most notably found for large-scale wind directions from the west-southwest with an average shift in the order of 30–40° (anti-clockwise) and from north-northwest with no or even a negative (clockwise) shift of some few degrees. The station at Florida stands out as it observes winds from 130° and 160° in large-scale flow from south-southeast (160°) to west-southwest (240°). Similarly, for large-scale flow from north (0°) to northeast (40°), Florida observes winds from the northwest. These large deviations are caused by the channelling effect from the Bergen valley, as commented by Utaaker (1995).

3.6. *Local-scale variations in the wind climate inland*

Typically, the wind climate in complex terrain has a large variability, both in space and time. The central Bergen area is indeed dominated by complex terrain. At the location of Florida, the Bergen valley has an orientation of approximately 160/340° or south-southeast/north-northwest. The valley is rather open towards the sea in the northwest and somewhat more sheltered in the south. Ulriken, which is the highest mountain around Bergen (643 m.a.s.l.), is located 3 km to the east of Florida.

The local-scale wind variability in the Bergen area is here investigated using data from the stations at Florida and Flesland. Figure 13 shows a map over the central Bergen area together with profiles of maximum topography heights surrounding the two stations.

3.6.1. Wind speed. Figure 14 shows the mean difference in wind speed between the two stations (Flesland–Florida) with respect to the ERA Interim 850 hPa wind speed and wind direction. For large-scale wind speeds higher than 10 m s^{-1} in the sector from south to west (170–290°), the mean wind speed at Flesland is consistently higher than at Florida. The maximum difference of around 4–5 m s^{-1} is found for 850 hPa wind speeds in the range 21–27 m s^{-1}. For wind directions outside this sector, the wind speeds are either similar or higher at Florida than at Flesland, forming

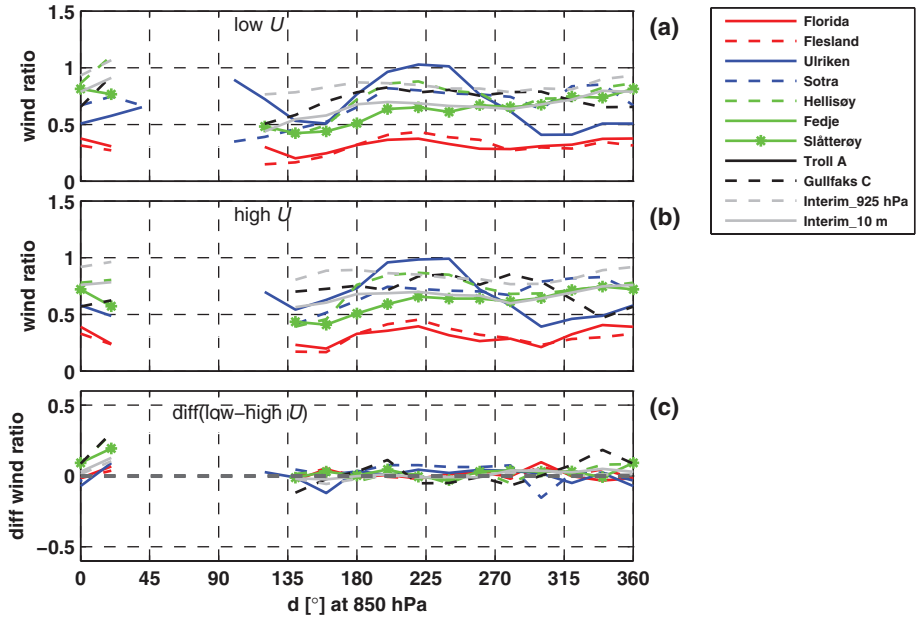

Fig. 10. Wind ratios for cases with large-scale wind speeds from (a) 5 to 10 m s^{-1} (b) 10 to 15 m s^{-1} and (c) the difference between both (a) and (b).

a dipole-like pattern with a positive difference for westerly winds and a negative difference for easterly winds.

3.6.2 Wind direction Looking at Fig. 15 a showing the summertime diurnal variation in wind direction distribution at Florida and Flesland for all large-scale wind speeds, a clear bimodal pattern is seen at both locations. The daytime (approximately 0700–2200 UTC) is dominated by a northerly wind component, whereas the winds at nighttime are more southerly. For large-scale winds below 10 m s^{-1} (Fig. 15 b), an even larger portion of the winds at Florida is northwesterly. At Flesland, a similar daytime increase in the frequency of northerly winds is seen.

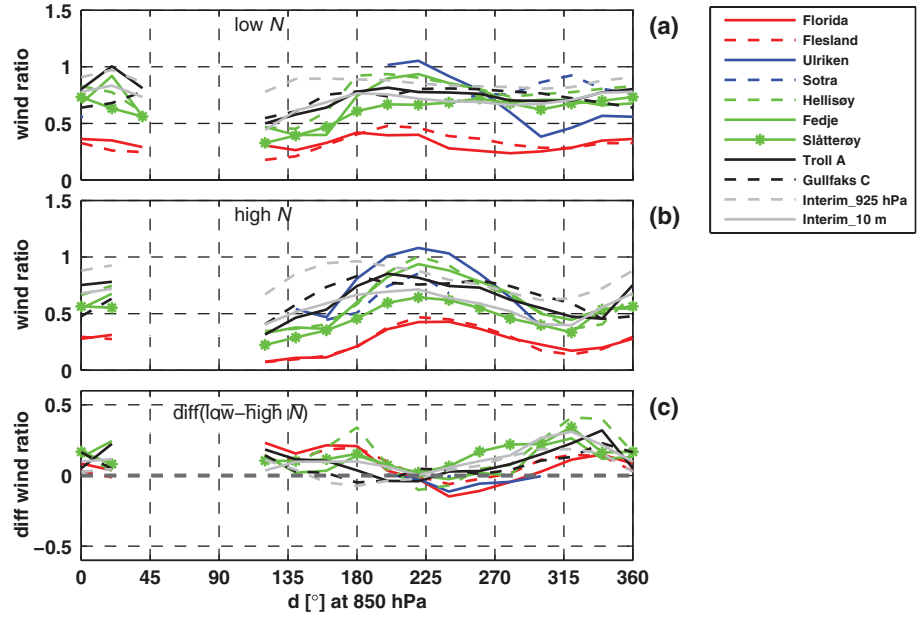

Fig. 11. Wind ratios for cases with large-scale wind speeds from (a) 5 to 10 m s^{-1} (b) 10 to 15 m s^{-1} and (c) the difference between both (a) and (b).

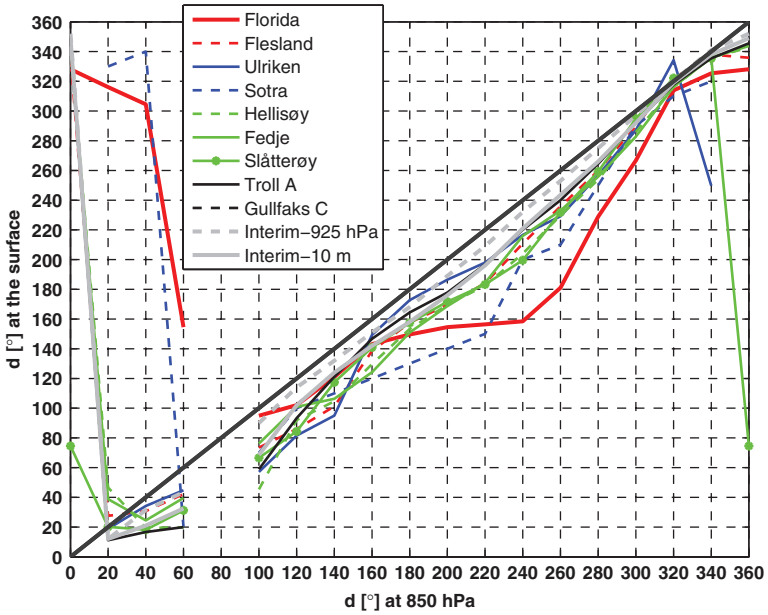

Fig. 12. Mean wind directions at the ground as a function of the 850 hPa wind direction.

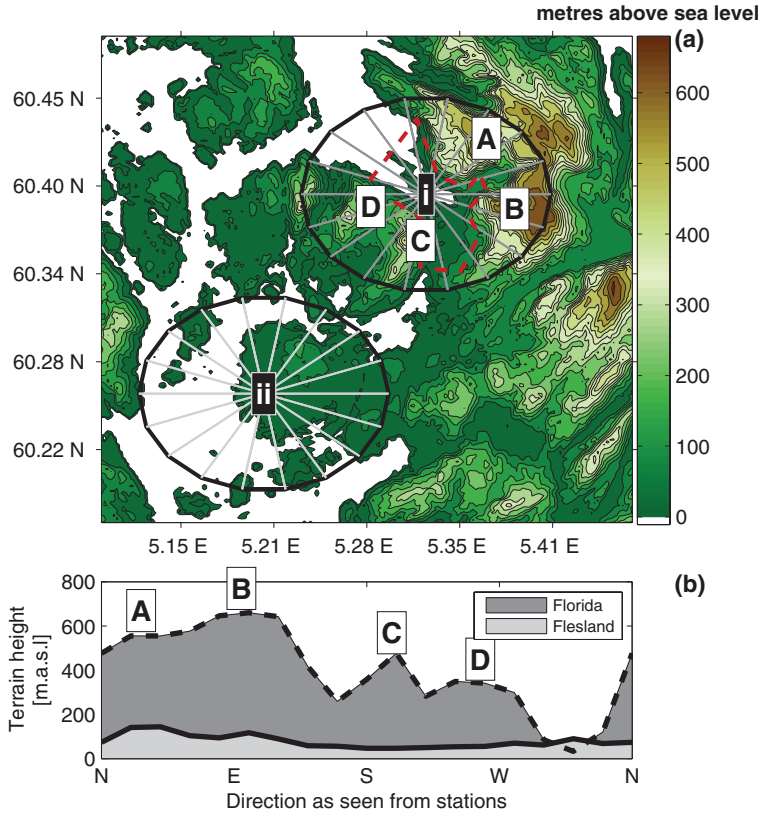

Fig. 13. (a) Map over the central Bergen area with Florida in the northeast (i) and Flesland in the southwest (ii). The city centre of Bergen is marked by a red, dashed line. Both stations are shown with circles surrounding them with radii of 4 km. Each circle sector spans 20°. (b) The sectors' maximum topography heights are plotted as a function of direction in relation to the respective stations. The topography curve for Florida is given labels from A to D indicating the geographical locations of the dominating topographic features around that location. Ulriken is marked by a 'B'.

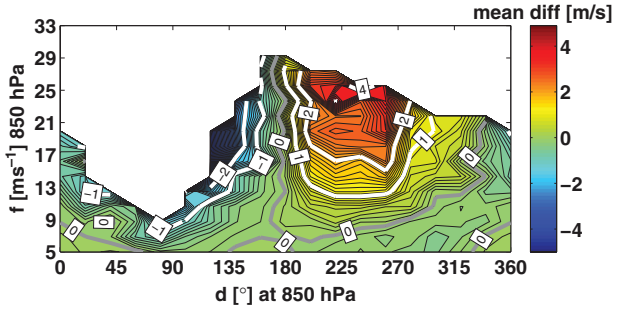

Fig. 14. Mean difference in wind speed between Florida and Flesland (Flesland–Florida) as a function of the 850 hPa wind speed, f (m s^{-1}), and wind direction, d (°).

Considering situations with large-scale winds above 10 m s^{-1}, as shown in Fig. 15 c, the wind direction distributions assume a character much more similar to that found during night-time, and only a slight diurnal signal is seen.

Differences between the two stations are mainly seen as deviations at Flesland from Florida's strictly south-south-east/ north-northwest-oriented wind components. These differences are especially evident during daytime, where Flesland has a larger prevalence of winds from the south and the west. Contributing to this difference is also a clockwise turn (veering) in wind direction with time at Flesland, which is not seen at Florida. The clockwise turn, as caused by the effect of Coriolis on the sea breeze circulation (e.g. Simpson, 1994), is presumably not evident at Florida because of the surrounding topography's tendency of aligning the wind along the Bergen valley's axis. It is clear that the sea breeze's presence depends on the magnitude of the large-scale wind speed. For wind speeds above 10 m s^{-1}, the daytime northerly wind components at ground are almost absent, whereas for large-scale wind speeds below 10 m s^{-1}, they dominate (Fig. 15).

Wintertime situations show, to a large extent, similar patterns as those found during night-time in the summer (not shown).

4. Discussion

In the present study, multiscale variability of winds in the complex terrain of southwestern Norway has been

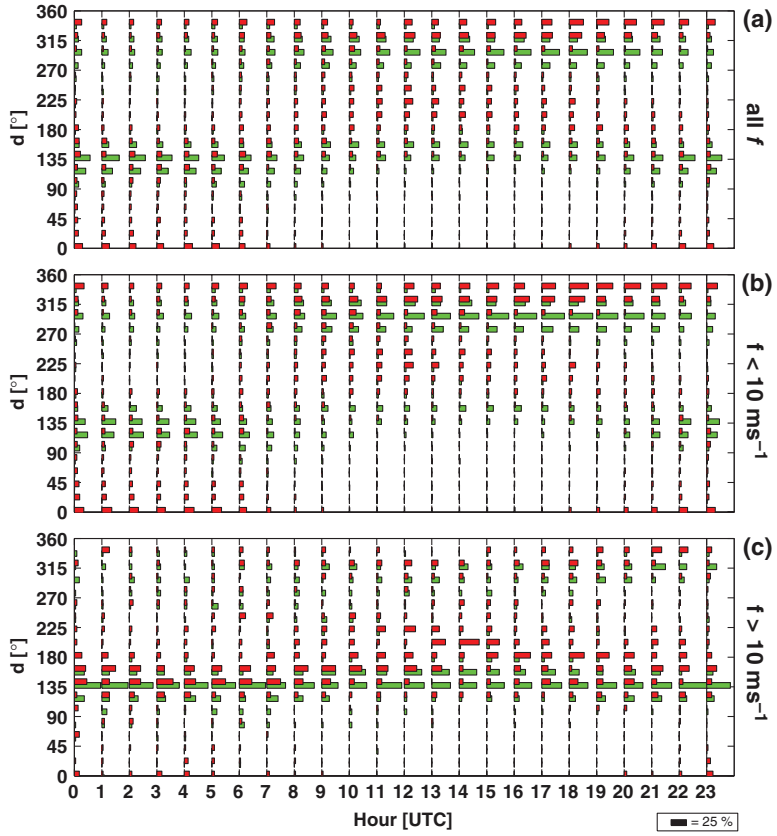

Fig. 15. Diurnal variation in wind direction distribution at Florida (green) and Flesland (red) during the summer months June, July and August for (a) all 850 hPa wind speeds (f), (b) 850 hPa wind speeds below 10 m s^{-1} and (c) 850 hPa wind speeds above 10 m s^{-1}. The statistics are based on hourly 10 minutes. Averages from the years 2005 to 2009.

investigated using up to 20 yr of observational and reanalysis data. The wind field has been shown to have a large variability in both space and time over a relatively short distance from offshore, via the coast to the inland and mountain.

The content of this article can be summarised in three main themes: geographical differences in the local wind speed distributions, the relationship between the flow at larger and smaller scale and variations in the wind climate at the local scale. The following discussion is arranged accordingly.

4.1. Geographical variations in the wind speed distribution

It has been shown that the differences in wind character between four characteristic surface categories in the Greater Bergen area (mountain, inland, coast and offshore) can to a large extent be quantified in terms of the Weibull distribution function. The higher variability found inland, as reflected by the low Weibull shape factors (Table 2), may be explained by local circulations associated with the complex terrain such as features such as orographic blocking, wakes, gap winds and thermally driven flow. Sea breeze is, indeed, found to dominate locally inland during daytime in the summer as seen in Figs. 7 and 15 and as found by Utaaker (1995). The higher wind speeds found in the mountains, at the coast and offshore (as reflected by higher Weibull scale factors), as compared to inland, are presumably caused by the relatively lower surface roughness and the lack of sheltering from surrounding topography, both at scales below 5 km (Fig. 13) as well as at scales of Southern Norway (Fig. 16).

The difference in Weibull scale factors between the coast and offshore locations is marginal. A distinct difference between these two categories, however, is the lack of diurnal variability in the wind speed offshore in summertime, but this difference alone has limited impact on the Weibull factors.

The current classification of surface categories through Weibull factors strictly only applies to the qualitative domain. A method, including a more statistical approach, to rigorously test to which category the stations belong could prove beneficial for future studies.

4.2. Variation in surface wind with the flow aloft

When considering the relationship between local and larger scale flow in the area, two main regimes stand out: relatively strong surface winds are found in southwesterly and northeasterly flow and weak surface winds are found for southeasterly flow (Fig. 8). Given a high atmospheric stability, relatively low surface wind speeds are also found in northwesterly flow.

BG05 also found strong surface winds along the southwestern coast of Norway in southwesterly flow. They attributed this flow nature to a coastal jet, mainly created by the effect of rotation deflecting the flow to the left, caused by a weakened Coriolis force as the flow is decelerated by the mountain. Petersen et al. (2005) described this kind of flow in their study of southwesterly flow impinging on an idealised mountain resembling the shape and north/south orientation of Southern Norway. A more than average deflection of the surface flow towards the left with respect to the flow aloft is indeed found for the southwesterly flow (Fig. 12). The surface wind speed is in this study shown to increase for higher values of Nh/U (Fig. 9) for the southwesterlies. This is in accordance with Overland and Bond's (1993) finding on the formation of jets along a mountainous coast line in Alaska as well as the idealised flow in Petersen et al. (2005).

In northeasterly flow, the surface wind is not far from being parallel to the height contours of the south Norwegian mountain range (Fig. 12). It is presumably accelerated by a pressure gradient associated with a wake at the west coast of South Norway.

Markedly reduced wind speeds are observed in southeasterly large-scale flow, not only at all surface stations but also at higher levels in the free atmosphere (ERA Interim 925 hPa data) (Fig. 8). This confirms the validity of the idealised numerical experiments made by BG05. They proposed an explanation in terms of a rather deep (more than 1500 m in some places), large-scale wind shadow forming downstream of the mountains in Southern Norway. They further suggested that this is not a classical wake, as typically occurring behind smaller scale mountains but a wake caused by rotational effects on the downstream inertio-gravity waves, as described by, for example Triib and Davies (1995). The wind ratio appears on average quite insensitive to Nh/U and U for this wind sector. There is no simple theory on how the mean surface wind speeds in wakes vary with U or Nh/U.

The surface winds in the northwesterly flow are quite variable in space and they are sensitive to the static stability, N. This indicates the presence of an orographic blocking with varying intensity and extension. Pierrehumbert and Wyman (1985) found through numerical simulations that the upstream horizontal extension of such blocking in a steep mountain zone is limited by the effect of rotation and is on the order of the Rossby radius of deformation, Nh/f. In the present case, for a value of $N = 0.01\,\mathrm{s}^{-1}$, $h = 1500$ m and $f = 10^{-4}\,\mathrm{s}^{-1}$, this would yield a deformation radius of 150 km. Even the most distant stations (Gullfaks C, $\sim$130 km and Troll A, $\sim$60 km) are within this distance from the mountains in Southern

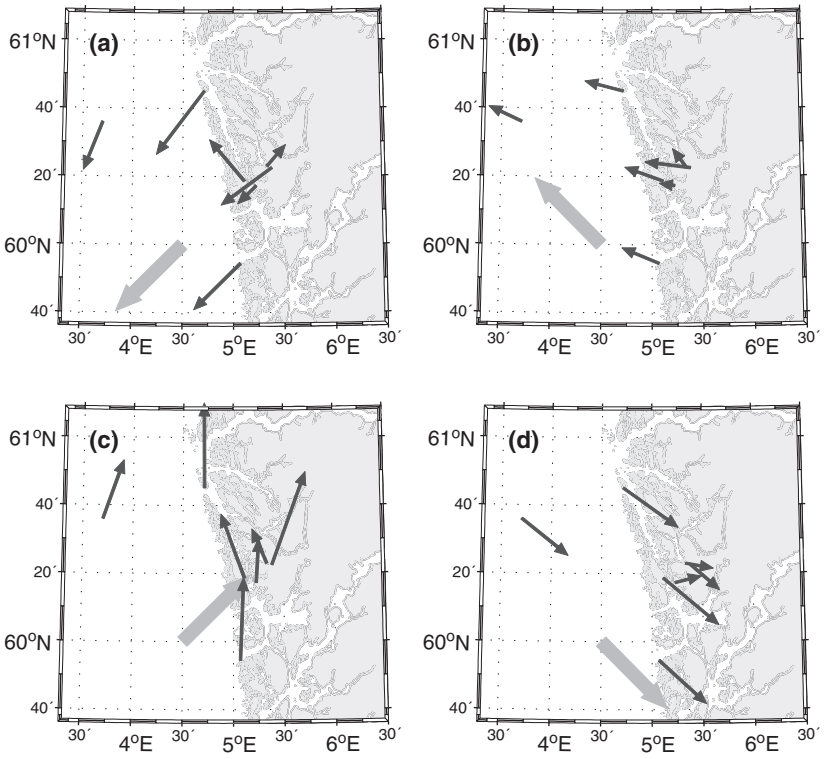

Fig. 16. Mean wind direction and wind ratio at the surface stations (black arrows) as a function of four ERA Interim 850 hPa wind directions (thick, grey arrow): (a) northeast (35–55°), (b) southeast (125–145°), (c) southwest (215–235°) and (d) northwest (305–325°). The wind ratio is indicated by the arrow lengths. For a wind ratio of 1, the black arrow has a length equal to that of the thick, grey arrow, meaning that the wind speed is the same at the surface as at 850 hPa. All 850 hPa wind speeds are above 5 m s^{-1}.

Norway. In the northwesterly flow, the weakening of the Coriolis force, as the flow impinges on the mountains, contributes to a leftward turning. This is towards the mountain range and thus supports the blocking. This is opposite to the Coriolis effect in the Southwesterly flow, where a turning to the left supports the left-side jet.

In summary, the effect of the atmospheric stratification, N, has an impact through two different processes. Firstly, it increases the Nh/U and thereby the magnitude of the orographic disturbances, including the above-described left-side jet and the blocking. Secondly, it dampens the vertical mixing of momentum and reduces, thereby, the surface wind speed. In the southwesterly flow, the stability has, on average, no effect on the mean surface wind speed. The two processes appear, in other words, to compensate for each other. In the northwesterly flow, both processes contribute to a decrease in the surface wind as N increases: the blocking is increased and vertical mixing is decreased. This appears clearly in Fig. 11. In the southeasterly flows, the impact of N may contribute to increased surface winds through enhancement of gravity waves, but such effects are presumably quite local, and at our stations damping of the surface winds through less vertical mixing appears to be more important.

An effect left out in the above discussion is that of latent heat release. The release of latent heat has been shown to decrease the deceleration of flow impinging on a mountain and thereby facilitate for more of the flow to go over and less to go around the mountain (Rotunno and Ferretti, 2001; Miglietta and Buzzi, 2004). This effect would presumably be present in the target area, at least with flow from a sector of 90° around west, where most moist air masses originate. Thus, the release of latent heat may be a damping on both the northwesterly blocking and the coastal jet in the southwesterly flow. It is, however, unclear if this effect is important for the non-saturated surface flow that may be cooled by evaporation from precipitation at the same time. An increased N would also contribute to less vertical mixing of momentum and thereby lower the surface wind speed. Further investigations based on numerical simulations could shed some light on the importance of this effect in the area.

4.3. *Variations in the wind climate at local scale*

As an example of variations in the wind climate at local scale, the wind at Flesland, where the mountains are relatively far away, has been compared to the wind at the

valley station at Florida. Both stations show markedly reduced wind speeds when compared to the flow aloft and the other investigated locations, but there are differences between them. The largest wind speed differences are found in southwesterly and easterly flow, averaging to about $+4\,\mathrm{m\,s^{-1}}$ and $-2\,\mathrm{m\,s^{-1}}$, respectively (Fig. 14). A possible explanation for the differences seen in easterly flow could be local downslope-accelerated winds, which have been found in easterly flow at inland stations in the area close to mountain slopes by Utaaker (1995). At Florida, these winds may be enhanced as they penetrate through the gap between two surrounding mountain ranges. Instances are found where these winds cause differences exceeding $12\,\mathrm{m\,s^{-1}}$ (not shown). Such cases are, however, very rare.

The apparent sheltering of Florida in southwesterly flow (with respect to Flesland) can be related to its surrounding topography, as seen in Fig. 13. There are at least two likely explanations for these differences. One is the mountain massif to the southwest of Florida (marked 'C' and 'D' in Fig. 13), potentially creating a wake over the city centre of Bergen. Secondly, the mountain massif to the northeast (marked 'A' in Fig. 13) is likely to create a local blocking of the southwesterly flow. Whether this shelter effect is caused by a downstream wake, an upstream blocking or a combination of both is hard to assess using only the dataset at hand. Numerical simulations may answer this question. Interestingly, looking at Fig. 11 showing the effect of increasing the atmospheric stability on the wind speed at the ground, a markedly stronger increase in wind speed for an increased atmospheric stability is seen at Florida than at Flesland in southwesterly flow. The cause of this stronger wind speed increase at Florida could be related to a stronger channelling through the Bergen valley, forced by a higher Nh/U deflecting the flow around and channelling it in between the surrounding mountains. It may also be related to gravity wave activity aloft.

Sea breeze circulation induces a high diurnal variability in the local winds inland and at the coast in the summer months. This is seen as a 1200 UTC wind speed maximum (Fig. 7). At the mountain of Sotra, however, there is a maximum in the afternoon (1800 UTC). As at Florida, there is a clockwise turn in wind direction with time at Sotra during summertime and at 1800 UTC, the local wind is on average northwesterly (not shown). One possible explanation for this apparent shift in timing of the Sotra, the wind maximum is a local, orographic, wind enhancement for this wind direction. This would be consistent with the increase in wind ratio observed at Sotra for a shift from westerly (1200 UTC) to northwesterly wind (1800 UTC) (Fig. 8).

Interestingly, the diurnal variation in winds at Ulriken appears to be inverted when compared with the inland and coastal stations. The lowest wind speeds are observed during daytime and the highest during night, which is typically dominated by a relatively shallow, stable boundary layer. The peak of Ulriken, thereby, resides in a relatively undisturbed flow decoupled from the surface layer in the valley. During daytime, when the boundary layer grows higher than Ulriken, the wind speed at Ulriken is affected by the valley surface, and a downward-directed vertical mixing of momentum extracts energy from the mean wind. This argument is supported by the fact that the highest atmospheric stability, as estimated from the temperatures observed at Florida and Ulriken, is on average found during night-time (not shown).

5. Summary and conclusions

This article leads us to a series of conclusions of both general value as well as more specific value for the understanding of weather and climate of southwestern Norway and the Greater Bergen area.

While previous studies have focused mainly on either meso to synoptic- or small-scale phenomena (e.g. BG05 and Utaaker, 1995), this article has aimed at forming a link between the large-scale flow and processes at small scales. Central to this has been the verification of several mesoscale flow structures frequently forming over the area as numerically simulated by BG05, using several years of data from nine automatic weather stations along with ERA Interim reanalysis.

A new concept for describing the flow patterns along the Norwegian west coast has been introduced in the form of four characteristic surface categories: offshore, coast, inland and mountain. The concept has allowed for a detailed description of the flow in the investigated area and has furthermore been justified through a remarkable resemblance in wind character at the locations within each of the four categories.

The distributions of wind speeds in the area have been quantified in terms of the Weibull probability density function. The inland locations are found to be characterised by small scale and shape factors of, respectively, around $4\,\mathrm{m\,s^{-1}}$ and 1.5, indicating generally low but highly variable wind speeds. The locations offshore and at the coast are associated with higher and more stable wind speeds, giving shape factors around 2 and scale factors around $8\,\mathrm{m\,s^{-1}}$. The mountain wind distribution is fundamentally different and appears as a hybrid between the coastal/offshore and inland categories: It shares the shape factor with the inland and the scale factor with the coast and offshore locations.

Winds from the northeast and east are rare, not only at sea level but also in the mountains and at mountain top level in the free atmosphere (ERA Interim 925 and 850 hPa). The south and southwesterly winds are the

most frequent aloft, which is in agreement with the position of the stormtrack.

The main findings on the relationship between the flow at larger scale and at the surface can be inferred from Fig. 16. In northwesterly large-scale flows, there is virtually no change in wind direction with height in the lower troposphere, whereas in southwesterly winds, there is strong clockwise turning (veering) of wind direction with height. This is clearly a topographic effect originating from the roughly south/north-oriented South-Norwegian mountain range and coastline, and the effect of rotation plays a central role. For large-scale flow from the southeast and statically stable flow from the northwest, surface winds are much weaker than the winds in the free atmosphere. This has been related to orographic blocking and wake. On the other hand, for large-scale flow from the southwest and northeast, the surface winds are relatively strong due to orographic enhancement.

Looking at the deceleration of winds at the surface, one would expect increased atmospheric stability to reduce the wind speed at the surface for any given wind speed in the free atmosphere due to damping of the turbulent vertical flux of horizontal momentum. This is, however, not the case in southwesterly flow, where the surface winds in stable flows on average are approximately the same as in unstable flows. However, in northwesterly flows, an unstable atmosphere gives relatively high wind speeds at the surface, and a stable atmosphere gives relative weak wind speeds at the surface. These findings have been related respectively to a left-side jet and orographic blocking.

On a smaller scale, the city centre of Bergen, as represented by the Florida station, is definitely sheltered in large-scale southwesterly winds. To what extent this is a blocking or wake effect by the surrounding topography, or a combination of both effects, remains unclear. Further investigations based on numerical simulations might give an answer to this.

Under weak synoptic flow, sea breeze dominates locally inland during daytime in the summer.

6. Acknowledgements

The present study is the result of a long-lasting, fruitful collaboration between AADI and GFI on weather observations at Mount Ulriken. We also owe our gratitude to ECMWF for providing ERA Interim reanalysis data and Avinor and met.no for giving access to data from Sotra.

References

Andersen, F. 1975. Surface winds in southern Norway in relation to prevailing H. Johansen weather types. *Meteor. Ann.* **6**(14), 377–399.

Barstad, I. and Grønås, S. 2005. Southwesterly flows over southern Norway-Mesoscale sensitivity to large-scale wind direction and speed. *Tellus.* **57A**, 136–152.

Barstad, I. and Grønås, S. 2006. Dynamical structures for southwesterly airflow over southern Norway: the role of dissipation. *Tellus.* **58A**, 2–18.

Bauer, M. H., Mayr, G. J., Vergeiner, I. and Pichler, H. 2000. Strongly nonlinear flow over and around a three-dimensional mountain as a function of the horizontal aspect ratio. *J. Atmos. Sci.* **57**, 3971–3991.

Bell, G. D. and Bosart, L. F. 1998. Appalachian cold-air damming. *Mon. Weather Rev.* **116**, 137–161.

Berge, E. and Hassel, F. 1984. An investigation of temperature inversions and local drainage flow in Bergen, Norway. *Meteorological report series.* University of Bergen, yearly report number. 2. (in Norwegian)

Birkhoff, G. 1960. Hydrodynamics. In *A study in logic, fact and similitude*. Princeton University Press, New Jersey, p. 184.

Bjerknes, J. and Solberg, H. 1921. Meteorological conditions for the formation of rain. *Geofys. Publ.* **2**, 59.

Bjerknes, J. and Solberg, H. 1922. Life cycles of cyclones and polar front theory of the atmospheric circulation. *Geofys. Publ.* **3**(report number 1), 1–18.

Colle, B. A. and Mass, C. F. 1995. The structure and evolution of cold surges east of the Rocky Mountains. *Mon. Weather Rev.* **123**, 137–161.

Doyle, J. D. 1997. The influence of mesoscale orography on a coastal jet and rainband. *Mon. Weather Rev.* **125**, 139–158.

Gill, A. E. 1982. *Atmosphere-Ocean Dynamics*. Academic Press, London, p. 662.

Hennessey, J. P. 1977. Some aspects of wind power statistics. *J. Appl. Meteor.* **16**(2), 119–128.

Justus, C. G. and Mikhail, A. 1976. Height variation of wind speed and wind distributions statistics. *Geophys. Res. Lett.* **3**(5), 261–264.

Kalthoff, N., Bischoff-Gauss, I. and Fiedler, F. 2003. Regional effects of large-scale extreme wind events over orographically structured terrain. *Theor. Appl. Climatol.* **74**, 53–67.

Lin, Y.-L. and Wang, T.-A. 1996. Flow regimes and transient dynamics of two-dimensional flow over an isolated mountain ridge. *J. Atmos. Sci.* **53**, 139–158.

Miglietta, M. M. and Buzzi, A. 2004. A numerical study of moist stratified flow regimes over isolated topography. *Q. J. R. Meteorol. Soc.* **130**, 1749–1770.

Ólafsson, H. and Ágústsson, H. 2009. Gravity wave breaking in easterly flow over Greenland and associated low level barrier- and reverse tip-jets. *Meteorol. Atmos. Phys.* **104**, 191–197.

Ólafsson, H. and Bougeault, P. 1996. Nonlinear flow past an elliptic mountain ridge. *J. Atmos. Sci.* **53**, 2465–2489.

Ólafsson, H. and Bougeault, P. 1997. The effect of rotation and surface friction on orographic drag. *J. Atmos. Sci.* **54**, 193–210.

Overland, J. E. and Bond, N. 1993. The influence of coastal orography: the Yakutat storm. *Mon. Weather Rev.* **121**, 1388–1397.

Parish, T. R. 1982. Barrier winds along the Sierra Nevada Mountains. *J. Appl. Meteor.* **21**, 925–930.

Pavia, E. G. and O'Brien, J. J. 1986. Weibull statistics of wind speed over the ocean. *J. Climate Appl. Meteor.* **25**, 1324–1332.

Peng, M. S., Li, S.-W., Chang, S. W. and Williams, R. T. 1995. Flow over mountains: Coriolis force, transient troughs and three dimensionality. *Q. J. R. Meteorol. Soc.* **121**, 593–613.

Petersen, G. N., Ólafsson, H. and Kristjánsson, J. E. 2005. The effect of upstream wind direction on atmospheric flow in the vicinity of a large mountain. *Q. J. R. Meteorol. Soc.* **131**, 1113–1128.

Pierrehumbert, R. and Wyman, B. 1985. Upstream effects of mesoscale mountains. *J. Atmos. Sci.* **42**, 977–1003.

Renfrew, I. A., Outten, S. D. and Moore, G. W. K. 2009. An easterly tip jet off Cape Farewell, Greenland. Part I: aircraft observations. *Q. J. R. Meteorol. Soc.* **135**, 1919–1933.

Rotunno, R. and Ferretti, R. 2001. Mechanisms of intense April rainfall. *J. Atmos. Sci.* **58**, 1732–1749.

Simpson, J. E. 1994. *Sea breeze and local wind*. Cambridge University Press, Cambridge, p. 234.

Smith, R. B. 1979. The influence of mountains on the atmosphere. *Adv. Geophys.* **21**, 87–230.

Smith, R. B. 1982. Synoptic observations and theory of orographically disturbed wind and pressure. *J. Atmos. Sci.* **39**, 60–70.

Smith, R. B. 1989. Hydrostatic airflow over mountains. *Adv. Geophys.* **31**, 59–81.

Smolarkiewicz, P. K. and Rotunno, R. 1989. Low froude number flow past three-dimensional obstacles. Part I: Baroclinically generated lee vortices. *J. Atmos. Sci.* **46**, 1154–1164.

Smolarkiewicz, P. K. and Rotunno, R. 1990. Low froude number flow past three-dimensional obstacles. Part II: upwind flow reversal zone. *J. Atmos. Sci.* **47**, 1498–1511.

Spinnangr, F. 1943. Synoptic studies on precipitation in southern norway. Part II: front precipitation. *Meteor. Ann.* **1**(17), 433–468.

Thorsteinsson, S. and Sigurdsson, S. 1996. Orogenic blocking and deflection of stratified air flow on an f-plane. *Tellus* **48A**, 572–583.

Trüb, J. and Davies, H. C. 1995. Flow over a mesoscale ridge: pathways to regime transition. *Tellus* **47A**, 502–524.

Utaaker, K. 1995. Energy in the planning of area – local climate in Bergen. *Meteorological report series*. University of Bergen, yearly report number 1. (in Norwegian)

Wei, T. 2010. *Wind power generation and wind turbine design*. WIT Press, Southampton, Boston, p. 725.

Whiteman, C. D. and Doran, J. C. 1993. The relationship between overlying synoptic-scale flows and winds within a valley. *J. Appl. Meteoro.* **32**, 1669–1682.

Paper 2

Simulations of the Bergen orographic wind shelter
Jonassen, M. O., Ólafsson, H., Valved, A. S., Reuder, J. and Olseth, J. A.
Submitted to Tellus A

Tellus **000**, 000–000 (0000) Printed July 25, 2012 (Tellus LaTeX style file v2.2)

Simulations of the Bergen orographic wind shelter

By Marius O. Jonassen[1]*, Haraldur Ólafsson[1,2], Aslaug S. Valved[1], Joachim Reuder[1], Jan A. Olseth[1],

[1] *Bergen School of Meteorology, Geophysical Institute, University of Bergen, Allégaten 70, Bergen, Norway;* [2] *Dpt. of Physics, University of Iceland. Icelandic Meteorological Office, Bústaðavegi 9, IS-150 Reykjavík Iceland*

July 25, 2012

ABSTRACT

Even though the coast of Western Norway is very windy, the centre of Bergen is rather calm. To gain further understanding of this wind shelter, we study the flow in the complex topography of Bergen during two southwesterly windstorms, using surface observations and high resolution numerical simulations. The results reveal large spatial variability in the local wind field. In some areas, there are periods of sustained winds of more than 25 m s^{-1}, while at nearby locations the winds are typically less than 5 m s^{-1}. The centre of Bergen is among the calmest areas. To investigate the effect of the individual mountains upstream (Løvstakken) and downstream (Fløyen) of the Bergen city centre, they have stepwise been removed from the model topography. Areas with relatively large wind speed reductions are found immediately downstream of Løvstakken and immediately upstream of Fløyen. At Florida, situated close to the city centre, both a wake effect of Løvstakken and a blocking effect of Fløyen are evident, but the latter is most prominent. The total impact of both mountains on the winds in the city is close to the sum of each of them. A spillover effect of Løvstakken acts to substantially increase the local precipitation in the centre of Bergen.

1 Introduction

The centre of Bergen, as represented by the weather station "Florida", appears to be remarkably sheltered during strong southwesterly flow (Harstveit, 2006; Jonassen et al., 2012). It is, however, unclear if this sheltering effect (hereby referred to as the "Bergen

* Corresponding author.

e-mail: marius.jonassen@gfi.uib.no

shelter") is caused by a wake of the upstream mountain massif of Løvstakken, a blocking by the downstream mountain massif of Fløyen or a combination of both. It is also unclear whether the wind observations at Florida are representative for the city centre of Bergen as a whole. These are the main questions to be answered in this study. The results may serve as guidance for studies of local dispersion of pollutants and weather forecasting in the area.

There are numerous studies on how larger scale flow is affected by the south Norwegian mountain range. Such investigations were initiated already during the early days of the Bergen School of Meteorology (Bjerknes and Solberg, 1921; 1922). Their studies were continued by Spinnangr (1943) and Andersen (1975). More recently, Barstad and Grønås (2005; 2006) identified and explained several meso-scale flow structures frequently forming over and around the topography of Southern Norway for flow within the sector south to west. Studies on local scale flow in the Bergen area, on the other hand, are few and focus mainly on thermally driven winds (Utaaker, 1995) and temperature inversions (Berge and Hassel, 1984).

Many of the flow patterns forming in connection to topography can be diagnosed using the non-dimensional mountain height $\hat{h}{=}Nh/U$ (e.g. Pierrehumbert and Wyman, 1985), where N is the Brunt-Väisälä frequency, describing the buoyancy on a vertically displaced air parcel, h is the mountain height and U is the flow speed of the airmass impinging on the mountain (e.g. Lin and Wang, 1996; Trüb and Davies, 1995; Ólafsson and Bougeault, 1996; Peng et al., 1995). High values of $\hat{h}$ facilitate for blocked flow leading to more of the flow going around than over the mountain. For low values of $\hat{h}$, the flow typically passes over the mountain and weak gravity waves may form. In the complex topography of southwestern Norway, these flow patterns frequently form at the larger scale as documented in the aforementioned literature. The same flow patterns should be expected to form at the lesser documented smaller scale, which we focus on in this study.

Topographically modified flow also affects precipitation (e.g. Jiang, 2003; Smith, 2006). Orographic precipitation, i.e. precipitation that is formed as moist air is forced to ascend over mountains, is an integral part of the climate of Western Norway, both in terms of mean values (e.g. Reuder et al., 2007), as well as extremes (Steensen et al., 2011). The phenomenon is of essential importance to a range of environmental factors of both direct and indirect influence on people, such as the local hydrology, long-term trends in terrain evolution, development of glaciers etc. Mountains enhance precipitation on their upwind side, but this enhancement may extend downstream of the mountains' crest as the precipitation elements are transported

downwind while forming and falling to the ground (the 'spillover effect') (e.g. Sinclair et al., 1996). The mean annual precipitation in the city of Bergen is 2250 mm, which is almost twice the value of precipitation at locations along the Norwegian southwest coast that are far away from mountains, such as Stavanger (1250 mm). It is well recognized that the larger scale topography of southern Norway has a central role in creating the high precipitation amounts along the southwest coast of Norway where Bergen is situated (e.g. Teigen, 2005). It is, however, not clear how large the contribution from the local topography is, e.g. through the above described spillover effect.

The primary purpose of this paper is to investigate the above introduced Bergen shelter effect. As a bi-product of this investigation, some results on precipitation will be presented. We study the local flow field in Bergen during two southwesterly windstorms that hit the southwest coast of Norway on 10 January, 2009 (Case 1) and 25 December, 2012 (Case 2). Data from a dense network of automatic weather stations (AWS) along with high resolution numerical simulations with the Weather Research and Forecasting model (WRF) (Skamarock et al., 2008) are used. The latter storm, named Dagmar by the Norwegian Meteorological Institute (met.no), caused floodings, property damage and even casualties along the coast in the areas most severely affected. The former windstorm is believed to be a more typical storm for the winter season in the region.

2 Atmospheric data

2.1 Case studies: Two southwesterly windstorms

On 10 January, 2009, a low pressure system to the south of Iceland and a high pressure system over central Europe induced a strong southwesterly flow along the coast of Southwestern Norway (Figure 1). This low pressure system moved slowly towards the northeast, and the associated flow over the Bergen area remained fairly stationary throughout the day. The system of 25 December, 2011, on the other hand, moved rather quickly eastwards. The general flow direction over Southwestern Norway thus shifted from southwesterly in the beginning of the day to westerly towards the evening.

2.2 Observations

There is a fairly dense network of AWSs in the Bergen area. The main AWS in Bergen is situated in the city centre and called "Florida". At Florida, the observations are made on

the top of the building of the Geophysical institute (GFI), University of Bergen, around 30 m above the surrounding ground. There is also a station on the top of the highest nearby mountain, Mount Ulriken. In addition, there is an AWS at the airport of Flesland, some 10 km to the south of Florida, and at Mount Sotra, situated to the west of the latter. Another station is situated at the Sotra bridge. All these stations were in service during the windstorm on 10 January, 2009. From the windstorm on 25 December, 2011, data from a network of 5 additional stations in Bergen are available from a research project at GFI.

An overview over the AWSs is given in Table 2 and their geographical locations are indicated in Figure 2.

The observed wind speed presented in the following, is from the unprocessed raw data. In the later comparison with the simulated wind speed, however, we have converted the observed wind speed (u_z) to the height of the lowermost half sigma level in the WRF model setup (z=19.5 m.a.g.l.) using the following following formula:

$$u_z = \frac{u_*}{\kappa}\left[\ln\left(\frac{z-d}{z_0}\right) + \psi(z, z_0, L)\right]$$

Here, u_* is the friction velocity (m s^{-1}) and z_0 is the roughness length in metres. The value of z_0 used for each AWS is indicated in Figure 5. d is the zero displacement length (m), i.e. the height adjacent to the obstacle (here building) at which the wind speed is zero. d is set to 2/3 of z_0, where z is 30 m for Florida and Nordnes. In the calculations, we have assumed neutral atmospheric stability, and hence $\psi(z, z_0, L)$, in which the Monin-Obukhov stability parameter, L, is set to zero. Setting L to zero is presumably a close approximation to reality because the investigated weather situations contain relatively high wind speeds, thus providing significant turbulent mixing of momentum.

During the two studied windstorms, the AWS observations reveal a large spatial variability in the wind field in the area (Figure 3). While the wind speed at the top of Mount Ulriken reaches more than 25 m s^{-1} in both cases, the wind speed at Florida, situated in the middle of the Bergen valley, barely exceeds 12 m s^{-1} in any of the cases.

The results from Case 2 allow for a more detailed investigation of the wind in the centre of Bergen because they include more AWS observations from the area. The wind speed observed in the northern part of the city centre (Nordnes) is stronger than at Florida. It is in fact more similar to the wind speed observed at Flesland, which is situated some 10 kilometres to the south of Florida and is more exposed to the strong winds.

While the wind speed at most AWSs decreases as the flow turns westerly in Case 2 (after 1800 UTC), it remains the same or is even slightly higher at Florida (the same is seen at the mountain stations of Strandafjellet and Løvstakken). When compared to the wind direction at Ulriken, which is on average found to be in reasonable agreement with the larger scale flow direction (Jonassen et al., 2012), the wind direction observed at the other AWSs show large deviations towards a more south and southeasterly direction for the southwesterly flow of Case 1. In the southwesterly flow of Case 2 (before 1800 UTC), the deviations are even larger and it is particularly large at Florida. This deviation is undoubtedly caused by the strong alignment of the flow to the Bergen valley at this location. In the westerly flow of Case 2 (after 1800 UTC), there is, on the other hand, a clear agreement in the wind direction for all stations. An exception is the AWS at Haukeland, where the wind speed is very low at this time.

2.3 Numerical simulations

In order to further investigate the local wind in the Bergen area during the two studied windstorms, and how it is modified by the surrounding topography, we have numerically reproduced the flow during both case studies with high horizontal resolution using the WRF model. The modeling system is fully compressible and is in this study run in non-hydrostatic mode using three one-way nested domains with horizontal resolutions of respectively 4.5, 1.5 km and 500 m. The outermost and coarsest domain (720 x 270 km^2) covers approximately the extent of Southern Norway and the innermost domain (42.5 x 42.5 km^2) covers a limited area centred around the city of Bergen. There are 61 vertical terrain following sigma levels with an increased density towards the ground and the lowest level is at approximately 36 m above the ground. The prognostic variables for temperature, humidity and wind are vertically staggered implying that they are calculated at each model half-level with the lowermost at an altitude of approximately 19.5 m above the ground. The two simulations cover respectively the 24 hour periods of 10-11.01.2009 and 25-26.12.2011 which of the first 6 hours are considered as spin-up. The RRTM scheme (Mlawer et al., 1997) is used for long wave radiation, the Dudhia scheme (Dudhia, 1989) for short wave radiation, and the Unified NCEP/NCAR/AFWA Noah land-surface model (Chen and Dudhia, 2001) with soil temperature and moisture in four layers for surface physics. Furthermore, the Mellor Yamada Janjic scheme (Janjic, 1990; 1996; 2002) is used for the parameterisation of the boundary

layer. The WSM 3-class simple ice scheme (Dudhia, 1989; Hong et al., 2004) is chosen for the parameterisation of microphysics with cloud water/ice, and rain/snow as prognostic variables. Operational analysis from the European Centre for Medium-Range Weather Forecasts (ECMWF) with a horizontal resolution of 0.125 degrees is used to initialise and force the model at its boundaries every 6 hour.

2.4 The simulation results

2.4.1 Sensitivity to model topography and landuse data We have carried out a number of sensitivity experiments in this study. The first set of experiments concerns the landuse and topography datasets. These are the datasets describing the physiographical model surface in terms of land coverage of e.g. sea, forest, agricultural landscape and cities, and topography height. The landuse determines to a large extent the local surface energy and momentum budget. Of probably the greatest importance to this study, which is focused on strong wind speeds, are accurate descriptions of the surface roughness length for momentum (z_0). In WRF, z_0 is along with the albedo, the emissivity and other parameters prescribed for each landuse type using a lookup table.

The most frequently used landuse dataset in WRF originates from the United States Geological Survey (USGS), and has a horizontal resolution of approximately 1 km (30 arc seconds). For high resolution simulations, the resolution and accuracy of this dataset is previously found to be insufficient (e.g. Cheng and Byun, 2008; Arnold et al., 2012). To further investigate the validity of this finding to the present study, a new dataset from GlobCorine is used in an additional set of sensitivity experiments. This dataset is based on data from 2009 and is thus of newer date than the USGS dataset (1992-1993). GlobCorine has a horizontal resolution of approximately 300 m and it has fewer landuse categories than the USGS set (13 vs. 24). In this study, we use the same look-up table for albedo, roughness etc. for the GlobCorine data as for the USGS dataset. Each landuse category in the GlobCorine dataset has been manually adopted to its closest approximate in the USGS dataset, meaning that for example the GlobCorine "forest" has been set to "mixed forest" and so on. A complete list of these conversions is given in table 3.

The roughness length for both the landuse datasets as well as the true roughness length at each of the AWSs are indicated in Figure 5. The true roughness length is estimated

Table 1. WRF sensitivity experiments with different landuse and topography datasets. See text for further explanations.

name	landuse	topography
USUS	USGS	USGS
USAS	USGS	Aster
GLUS	GlobCorine	USGS
GLAS	GlobCorine	Aster

by using the values from the WRF lookup table that correspond to the realistic landuse category at the location of each AWS.

Figure 4 shows the landuse over a zoom-in of the finest model domain (500 m horizontal resolution) for the USGS and GlobCorine datasets. It can be seen that, even though GlobCorine has fewer categories, it displays significantly more fine scale spatial details in the land use field. Also, the GlobCorine coastline matches the high resolution coastline from the Global Self-consistent, Hierarchical, High-resolution Shoreline Database, (GSHHS) significantly better than does the USGS coastline.

In addition to the USGS topography dataset, we employ a topography dataset from the Advanced Spaceborne Thermal Emission and Reflection Radiometer (ASTER). The dataset is made in a joint effort between the Ministry of Economy, Trade, and Industry (METI) of Japan and the United States National Aeronautics and Space Administration (NASA). The horizontal resolution is 1 arc second (30 m) as opposed to the 30 arc seconds of the USGS topography dataset. We have made a couple of adjustments to the USGS topography and GlobCorine landuse datasets. The USGS topography dataset features in its standard WRF setup an apparent westwards shift of approximately 500 m when compared to reality (AWS station heights) and the ASTER dataset. We therefore corrected it accordingly in the preprocessing of the model data input. Also, a smaller area (approximately 1x1 km) surrounding Nordnes does not have an urban landuse category in the GlobCorine dataset. Since this area is a part of the centre of Bergen, which is of central interest to this study, the error was corrected accordingly.

The main results from the landuse and topography sensitivity experiments are presented in Figure 6. The figure shows the average root mean squared error (RMSE) and mean error (bias) between the available AWS wind speed observations and the corresponding model point estimations.

The error statistics reveals only a marginal sensitivity to the applied model landuse and topography datasets. In Case 1, using the GLAS setup gives both the lowest average RMSE

(2.4 m s^{-1}) and the lowest average bias (1.3 m s^{-1}). In Case 2, there is no such consistent improvement for any of the experiments. Relatively large wind speed biases are found at Mount Ulriken, with the largest ones being around 6 m s^{-1} in the USUS setup for Case 2. Using the high resolution terrain dataset from ASTER has a clear advantage over using the USGS dataset for Ulriken. At this location, there is a reduction in the wind speed RMSE and bias of around 1 m s^{-1} in both cases. In the further analysis of the model results, the GLAS setup is used, which combines the two highest resolution datasets (GlobCorine and ASTER).

2.5 The Bergen shelter

The simulated larger scale flow (Figure 7) compares reasonably well with surface stations situated along the South Norwegian coast. The synoptic flow pattern in southwestern Norway did not change much during the course of the day in Case 1. The flow during Case 2, on the other hand, started out as southwesterly and ended as westerly. The simulation results show that both cases are associated with strong wind with more than 30 m s^{-1} off the northwestern corner (west cape) and over the central mountain range of Southern Norway (Langfjella). These flow patterns are typical for southwesterly storms in the region (Barstad and Grønås, 2005).

In the Bergen area, the model matches in general the near surface observed wind speed and wind direction well (Figures 8 and 9). As commented on in the above error statistics analysis, the largest average deviations are found at mount Ulriken. Also the simulated wind direction at Ulriken is off by some 20° towards the south in both cases. The model times quite accurately the shift towards westerly winds around 1500 UTC in Case 2 at all stations. An exception is Florida, where this shift is delayed by a couple of hours. The wind speed at Florida is, however, less than 5 m s^{-1} at this time.

A main goal of this article is to investigate how the mountains surrounding the centre of Bergen impact the local flow field in the southwesterly storms. We have done this through three different sensitivity experiments, in which the following modifcations to the model topography have been applied (see Figure 2): 1) the Løvstakken massif is removed (NOL), 2) the Fløyen massif is removed (NOF) and 3) both of them are removed (NOFL). The results from these experiments are presented in the following.

From Figure 10, showing the near surface wind speed at 0000 UTC on 11 January, 2009,

in the CTRL run and the difference between this and the three topography sensitivity experiments, several deducations can be drawn. Firstly, the simulated local flow field evidently features a considerable spatial variability (Figure 10 a), ranging from 2-20 m s^{-1} thus supporting the impression given from the above analysis of the AWSs observations. The highest wind speeds are found along the coast and at the mountain tops. The lowest wind speeds are found immediately up- and downstream of the local mountains and hills. The centre of Bergen appears to be one of the calmer areas. Removing the mountain massif of Løvstakken (Figure 10 b) gives a wind speed increase in most parts of the centre of Bergen of 2-6 m s^{-1}. The highest increase is found closest to the massif itself. Removing Fløyen (Figure 10 c) causes a wind speed increase of up to 6 m s^{-1} in an area immediately upstream of the massif. When removing both massifs (Figure 10 d), the effect on the wind field in the Bergen valley is the largest and wind speed increases of up to 8 m s^{-1} are seen over larger parts of the city centre. The wind field in the northernmost part of the city centre (around the AWS at Nordnes) is least affected by the model topography modifications.

The above findings allow for the definition of four areas with characteristic flow patterns during the large-scale southwesterly flow, as indicated in Figure 11: The 'Wake area' is the area immediately downstream of Løvstakken, which is mainly affected by this massif. The 'Less calm area' experiences the smallest effect of the surrounding mountains. The 'Block area' is mainly affected by 'Fløyen' and 'Florida area', which is the area representative for the main AWSs in the centre of Bergen, is affected by both the presence of Løvstakken and Fløyen. The temporal development of changes in wind speed within each of the areas, as caused by the topography modifications, is shown in Figure 12. The situation is fairly stationary in most of Case 1, with a slight tendency towards an increased shelter effect and a more westerly synoptic flow towards the end of the day. In Case 2, there is a complete change in wind speed within the four areas at around 1600 UTC, as the synoptic wind turns from southwest to west. The area categorisation made above for the southwesterly wind does no longer hold for the westerlies. The location of the area affected by Løvstakken shifts further to the south (Figure 13). Fløyen, on the other hand, affects an area further to the north and the effect of removing both mountain massifs resembles a superposition of the two former effects. Otherwise, for the southwesterly part of Case 2, the spatial flow patterns seen for the topography modifications resembles closely that of Case 1 (not shown).

2.6 The vertical flow structure

As in the above described horizontal near surface wind field, the wind speed reduction in the vertical is largest immediately down- and up-stream of respectively Løvstakken and Fløyen (Figure 14). The vertical extent of the effect from removing Løvstakken is relatively low when compared to the effect from removing Fløyen, which extends to levels roughly twice that of the nearby mountain tops. Upstream of Løvstakken, there is a sign of a small blocking effect (equal to or less than 2 m s^{-1}), which extends to elevations between 1.5 (NOL) and 2 times the height of this mountain (NOFL).

The combined effect of removing both mountain massifs (NOFL, Figure 14 d) is close to the effect of the blocking alone and it is strongest at around 50 m.a.g.l., where it reduces the wind speed by up to 8 m s^{-1}. Above all mountain crests, there are signs of speedup when comparing the runs with and without the original model topography.

2.7 Impact of the local topography on the precipitation field

It is evident that the local topography surrounding Bergen should have an impact on the precipitation in the area. Although precipitation is not the main focus of this article, a short analysis of this parameter is presented. Figure 15, shows the simulated precipitation accumulated between 0600 and 2400 UTC on 10 January 2009. The largest precipitation amounts are found downstream of the local mountain and hill tops. In most of the centre of Bergen, the simulated 18 hour accumulated precipitation is between 15 and 20 mm, which compares quite well with the observed amount at Florida of 18 mm. In the flat area immediately upstream of Løvstakken, the model predicts only roughly half of this amount. Removing Løvstakken from the model topography (Figure 15 b), brings the amount of precipitation down by 10-12 mm in most parts of the city centre. Removing Fløyen, on the other hand, has barely any impact at all (Figure 15 c). The results for Case 2 are similar to those of Case 1, with no effect on the precipitation in Bergen from removing Fløyen and a slightly smaller effect than in Case 1 from removing Løvstakken (not shown).

3 Discussion

Numerical sensitivity experiments, where the atmospheric flow during two southwesterly windstorms that hit southwestern Norway on 10 Januar, 2009 and 25 November 2011, has been reproduced. The results show that the sheltering of the northwestern part of the city

centre of Bergen is caused by the decelerating effect upstream of the the Fløyen massif, while the sheltering in the southwestern part of Bergen is largely a wake effect of the Løvstakken massif. These findings seem reasonable, as these areas lie both close to the foothills of the mountains with the largest impact on the wind. A more interesting result is that the total sheltering effect of both mountains is close to the sum of the blocking effect of Fløyen and the wake effect of Løvstakken. This is roughly valid in all central parts of the city as well as aloft, above the Bergen valley. No existing theory supports this fact. There are indeed several studies that reveal that stratified flow in the vicinity of two mountains can be very sensitive to both horizontal and vertical scales of the topography. Through the modification of gravity waves, a mountain downstream of a valley can thus both contribute to acceleration and deceleration of the flow inside the valley. Such effects have been studied by e.g. Hunt and Richards (1984), Grubiŝić and Stiperski (2009) and Stiperski and Grubiŝić (2011) for idealised flows and Ágústsson and Ólafsson (2007) for real flows. Seen from an energetic point of view, a reduction of the speed or the kinetic energy by the wake of the first mountain moves the flow deeper into a regime of orographic blocking as it meets the second mountain and the non-dimensional mountain height is increased. A wake may also be enhanced or sustained by a downstream mountain, blocking the low-level flow.

The simulated near surface wind speed compares relatively well with the observations from a local AWS network. A sensitivity analysis using two different model topography datasets (USGS and ASTER) and two different landuse datasets (USGS and GlobCorine) shows only a marginal sensitivity in the wind speed error statistics to the choice of these datasets. Previous studies have found larger differences when comparing lower and higher resolution datasets (e.g. Cheng and Byun, 2008; Arnold et al., 2012). One consistent improvement, however, is seen in the wind speed at Ulriken when applying the ASTER topography dataset instead of the USGS dataset. This improvement is most likely caused by a more accurate description of the topography in the ASTER dataset. In reality, Ulriken AWS is situated at 605 m.a.g.l., whereas in the simulations using the USGS dataset it is at 459 m.a.g.l. and in those using the ASTER dataset it is at 470 m.a.g.l. In a study of extreme winds in the Bergen region, Harstveit (2006) asserted that Ulriken experiences a local speed up of winds from the sector south to west. He attributed this speed up to small scale features in the local terrain. It is evident that a simulation, even at a high horizontal resolution of 500 m, will not accurately capture all such features. Larger improvements from using higher resolution topography model datasets can probably be expected when going to even higher

horizontal grid resolutions. Then, however, one approaches scales at which the normal ABL model schemes are no longer suited and Large-Eddy Simulation (LES) schemes should rather be applied. Such simulations are beyound the scope of the present study.

Although the studied windstorms are quite typical in terms of wind pattern (see climatology by Jonassen et al. (2012)), there do exist cases where strong and gusty winds in southwesterly flow reach down to parts of the centre of Bergen (e.g. Harstveit, 2006). Such cases are, however, not common and they are presumably related to rare details in the vertical profile of the flow and are left for future studies.

A significant downstream shift of the precipitation maximum around the mountain massif of Løvstakken, largely affecting the city centre of Bergen, is found in the simulation of the southwesterly windstorm of 10 January, 2009. This 'spillover effect' is typical for strong wind events as described by e.g. Sinclair et al. (1996) and during the Reykjanes experiment described in Rögnvaldsson et al. (2007). The removal of Løvstakken from the model topography confirms that this mountain is the source of the described precipitation pattern. Removing the Fløyen mountain massif, which is downstream of the city centre, has hardly any effect on the precipitation in the city. Previous simulations of orographic precipitation with a clear spillover, as e.g. Rögnvaldsson et al. (2007), have revealed a limited sensitivity of the precipitation pattern to the choice of microphysics parameterisation scheme. The topographic and atmospheric conditions in Rögnvaldsson et al. (2007) were quite similar to those in the present study, but in order to establish a conclusive and quantitative result on the impact of individual mountains of the precipitation climatology, many more simulations would be needed.

4 Summary and conclusions

In this study, our main goal has been to investigate why the centre of Bergen is sheltered during southwesterly windstorms. A series of numerical sensitivity experiments, in which we have stepwise removed larger parts of the topography surrounding the city centre from the model topography during two southwesterly windstorms, give some answers. The sheltering of Bergen appears to be caused by a combination of a downstream wake of the Løvstakken mountain massif and an upstream blocking from the Fløyen massif. The combined effect is close to the sum of each of them.

Regarding the initially posed question whether the AWS at Florida is representative of

the Bergen centre as a whole, this is only partly true. The effect from each of the mountains is strongest closest to their foothills. Hence, downstream of Løvstakken a wake dominates and upstream of Fløyen, there is a zone of blocking. At Florida, the blocking effect from Fløyen is most prominent.

Through spillover, the Løvstakken massif acts to increase the precipitation in the centre of Bergen during both of the investigated windstorms. The Fløyen massif turns out to have a minimum impact on the precipitation upstream of it. The strength of the spillover effect is known to increase with increasing wind speeds. Thus, the effect is likely less pronounced on the average than in the present strong wind cases.

A series of numerical sensitivity experiments using high resolution landuse and topography datasets have been carried out. The wind speed error statistics reveal only a marginal sensitivity to the choice of these datasets. This result may, however, be sensitive to the horizontal grid resolution.

5 Acknowledgment

The present study is partly the result of a long-lasting collaboration between AADI and GFI on weather observations at Mount Ulriken. We also owe our gratitude to Avinor and met.no for giving access to data from Sotra.

REFERENCES

Ágústsson, H. and Ólafsson, H. 2007. Simulating a severe windstorm in complex terrain. *Meteorologische Zeitschrift* **16**(1), 111–122.

Andersen, F. 1975. Surface winds in southern Norway in relation to prevailing H. Johansen weather types. *Meteor. Ann.* **6**(14), 377–399.

Arnold, D., Schicker, I. and Seibert, P. 2012. Towards high-resolution environmental modelling in the alpine region. *NATO Science for Peace and Security Series C: Environmental Security* **14**, 269–273.

Barstad, I. and Grønås, S. 2005. Southwesterly flows over southern Norway-Mesoscale sensitivity to large-scale wind direction and speed. *Tellus 57A* pp. 136–152.

Barstad, I. and Grønås, S. 2006. Dynamical structures for southwesterly airflow over southern Norway: the role of dissipation. *Tellus 58A* pp. 2–18.

Berge, E. and Hassel, F. 1984. An investigation of temperature inversions and local drainage flow in Bergen, Norway (in Norwegian). *Meteorological report series, University of Bergen* .

Bjerknes, J. and Solberg, H. 1921. Meteorological conditions for the formation of rain. *Geofys. Publ* .

Bjerknes, J. and Solberg, H. 1922. Life cycles of cyclones and polar front theory of the atmospheric circulation. *Geofys. Publ* **3**(1), 1–18.

Chen, F. and Dudhia, J. 2001. Coupling an Advanced Land Surface-Hydrology Model with the Penn State-NCAR MM5 Modeling System. Part 1. Model Implementation and Sensitivity. *Mon. Wea. Rev.* **129**, 569–585.

Cheng, F.-Y. and Byun, D. W. 2008. Application of high resolution landuse and land cover data for atmospheric modeling in the HoustonâĂŞGalveston metropolitan area, Part I: Meteorological simulation results. *Atmospheric Environment* **42**, 7795âĂŞ7811.

Dudhia, J. 1989. Numerical study of convection observed during the winter monsoon experiment using a mesoscale two-dimensional model. *J. Atmos. Sci* **46**, 3077–3107.

Grubiŝić, V. and Stiperski, I. 2009. Lee-Wave Resonances over Double Bell-Shaped Obstacles. *J. Atmos. Sci* **66**, 1205–1228.

Harstveit, K. 2006. Mapping of extreme wind conditions in Bergen kommune (in Norwegian). *met.no report* **3**, 55pp.

Hong, S., Dudhia, J. and Chen, S. 2004. A revised approach to ice microphysical processes for the bulk parameterization of clouds and precipitation. *Mon. Weather. Rev* **132**, 103–120.

Hunt, J. C. R. and Richards, K. J. 1984. Stratified airflow over one or two hills. *Bound.-Lay. Meteorol.* **30**, 223–229.

Janjic, Z. 1990. The step-mountain coordinate: physical package. *Mon. Weather Rev.* **118**, 1429–1443.

Janjic, Z. 1996. The surface layer in the NCEP eta model. *11th conference on numerical weather prediction, American Meteorological Society* pp. 354–355.

Janjic, Z. 2002. Nonsingular implementation of the Mellor-Yamada Level 2.5 Scheme in the NCEP meso models. *NCEP Office Note* p. 61p.

Jiang, Q. 2003. Moist dynamics and orographic precipitation. *Tellus 55A* pp. 301–316.

Jonassen, M. O., Ólafsson, H., Reuder, J. and Olseth, J. A. 2012. Multi-scale variability of winds in the complex topography of southwestern Norway. *Tellus 64A* pp. 1–17.

Lin, Y.-L. and Wang, T.-A. 1996. Flow regimes and transient dynamics of two-dimensional flow over an isolated mountain ridge. *J. Atmos. Sci.* **53**, 139–158.

Mlawer, E. J., Taubman, S. J., Brown, P. D., Iacono, M. J. and Clough, S. A. 1997. Radiative transfer for inhomogeneous atmospheres: RRTM, a validated correlated-k model for the longwave. *J. Geophys. Res.* **102**, 16663 – 16682.

Ólafsson, H. and Bougeault, P. 1996. Nonlinear Flow Past an Elliptic Mountain Ridge. *J. Atmos. Sci.* **53**, 2465–2489.

Peng, M. S., Li, S.-W., Chang, S. W. and Williams, R. T. 1995. Flow over mountains: Coriolis force, transient troughs and three dimensionality. *Q. J. R. Meteorol. Soc.* **121**, 593–613.

Pierrehumbert, R. and Wyman, B. 1985. Upstream effects of mesoscale mountains. *J. Atmos. Sci.* **42**, 977–1003.

Reuder, J., Fagerlid, G. O., Barstad, I. and Sandvik, A. 2007. Stord Orographic Precipitation Experiment (STOPEX): an overview of phase I. *Advances in Geosciences* **1o**, 17–23.

Rögnvaldsson, O., Bao, J.-W. and Ólafsson, H. 2007. Sensitivity simulations of orographic precipitation with MM5 and comparison with observations in Iceland during the Reykjanes Experiment. *Meteorol. Z.* **16**, 87–98.

Sinclair, M. R., Wratt, D. S., Henderson, R. D. and Gray, W. R. 1996. Factors Affecting the Distribution and Spillover of Precipitation in the Southern Alps of New Zealand - A Case Study. *J. Appl. Meteor.* **36**, 428–442.

Skamarock, W. C., Klemp, J. B., Dudhia, J., Gill, D. O., Barker, D. M., Duda, M. G., Huang, X.-Y., Wang, W. and Powers, J. G. 2008. A description of the Advanced Research WRF Version 3. *NCAR Tech. Note* **TN-475+STR**, 125.

Smith, R. B. 2006. Progress on the theory of orographic precipitation. *Geological Society of America, Special paper 398* pp. 1 – 16.

Spinnangr, F. 1943. Synoptic studies on precipitation in southern norway. ii front precipitation. *Meteor. Ann.* **1**(17), 433–468.

Steensen, B. M., Ólafsson, H. and Jonassen, M. 2011. An extreme precipitation event in Central Norway. *Tellus 63A* pp. 675–686.

Stiperski, I. and Grubišić, V. 2011. Trapped Lee Wave Interference in the Presence of Surface Friction. *J. Atmos. Sci* **68**, 918–936.

Teigen, R. 2005. Numerical simulation of orographic precipitation in West Norway (in Norwegian). *Master's thesis. Geophysical institute, University of Bergen. http://www.ub.uib.no/elpub/2005/h/406004/Hovedoppgave.pdf* .

Trüb, J. and Davies, H. C. 1995. Flow over a mesoscale ridge: Pathways to reg transition. *Tellus 47A* pp. 502–524.

Utaaker, K. 1995. Energy in the planning of area - local climate in Bergen (in Norwegian). *Meteorological report series,*

447 *University of Bergen* (1).

6 Figure captions

Figure 1: Mean sea level pressure at 1200 and 1800 UTC on 10 January 2009 (a and b) and 25 December 2011 (c and d). Based on analysis from the European Centre for Medium-Range Weather Forecasts. The location of Bergen is indicated with a black diamond.

Figure 2: The topography of the area of main interest, the locations and names of the AWSs (S1-S10), and indications of the geographical extent of the two dominating mountain massifs in the area: Løvstakken (1) and Fløyen (2). The dashed, red line indicates the approximate extent of the centre of Bergen. The dashed, black line between the points "A" and "B" indicates the position of the cross section in Figure 14.

Figure 3: Observed wind speed and wind direction during the investigated windstorms on 10 Januar, 2009 and on 25 December, 2011 in the Bergen area

Figure 4: A zoom-in of the landuse of domain 3 (500 m horizontal resolution) using the datasets of a) USGS and b) GlobCorine. See Table 3 for a list over landuse categories and respective numbers indicated on the colorbar. The coastline from GSHHS is indicated with a solid, black line.

Figure 5: Roughness length for momentum at the different AWSs for the simulations using the USGS and GlobCorine landuse datasets. The real roughness length is indicated as well.

Figure 6: Root mean square error (RMSE) and mean error (bias) for wind speed (observed minus simulated) using four different combinations of model landuse and topography datasets. Table 1 lists and explains the different experiments. Case 1 is 10 January, 2009 and Case 2 is 25 December, 2011

Figure 7: Simulated near surface (19.5 m.a.g.l.) horizontal wind speed at a) 1200 UTC on 11 Januar 2009 and at b) 2100 UTC on 25 December 2011. The results are from the outermost domain (4.5 km horizontal resolution). Observations from selected AWSs along the coast are indicated with red wind barbs. Each barb is 2.5 m s^{-1}. The location of Bergen is indicated with a "B".

Figure 8: Observed and simulated wind speed at selected AWSs on 10 Januar 2009 (Case 1) and 25 December 2011 (Case 2). The simulation results are from the innermost domain (500 m horizontal resolution)

Figure 9: As in Figure 8, but for wind direction.

Figure 10: a) near surface wind speed at 0000 UTC on 11 January in the CTRL sim-

ulation, b) wind speed in CTRL minus NOL, c) wind speed in CTRL minus NOF, and d) wind speed in CTRL minus NOFL. The dashed, red line indicates the approximate extent of the centre of Bergen.

Figure 11: Areas of characteristic location and flow patterns. The terrain height is given with contours every 100 m.

Figure 12: Difference in simulated near surface wind speed between the CTRL and the sensitivity simulations with topography modifications averaged within the areas indicated in Figure 11. The wind barbs at the top of the panels denote the simulated wind speed and direction at 900 hPa averaged within a box centred at 4.3°E and 61°N. Each half barb is 2.5 m s^{-1}.

Figure 13: Same as in Figure 10, but for 2100 UTC on 25 December, 2011.

Figure 14: a) cross section of horizontal wind speed at 0000 UTC on 11 January in the CTRL simulation, b) wind speed in CTRL minus NOL, c) wind speed in CTRL minus NOF, and d) wind speed in CTRL minus NOFL. The geographical location of the cross section is indicated in Figure 2.

Figure 15: a) 18 hour accumulated precipitation at 0000 UTC on 11 January, 2009, in the CTRL simulation, b) precipitation in CTRL minus NOL, c) precipitation in CTRL minus NOF, and d) precipitation in CTRL minus NOFL.

Table 2. Automatic weather stations. The height for Ulriken is set to 15 m.a.g.l., representing an average elevation above its immediate surroundings.

Station	Timeres. (min)	Source	m.a.s.l.	m.a.g.l.
Florida	10	GFI	48	30
Ulriken	10	AADI/GFI	605	15
Flesland	60	met.no	48	10
Sotra bridge	10	NPRA	50	50
Sotra	60	Avinor	341	10
Ulriksbakken	10	GFI	408	2.5
Haukeland	10	GFI	64	10
Løvstakken	10	GFI	472	2.5
Strandafjellet	10	GFI	303	2.5
Nordnes	10	GFI	48	30

Table 3. Table used in this study to convert GlobCorine landuse categories to USGS landuse categories.

	GlobCorine categories	USGS categories
1	urban and associated areas	urban and built-up land
2	rainfed cropland	dryland and cropland pasture
3	irrigated cropland	Irrigated cropland and pasture
3	complex cropland	irrigated cropland and pasture
4	not converted	mixed dryland / irrigated cropland and pasture
5	mosaic cropland / natural vegatation	cropland / grassland mosaic
6	mosaic of natural vegetation	cropland/woodland mosaic
7	grassland	grassland
8	heathland and sclerophyllus vegetation	shrubland
9	not converted	mixed shrubland/grassland
10	not converted	savanna
11	not converted	deciduous needleleaf forest
12	not converted	deciduous broadleaf forest
13	not converted	evergreen broadleaf forest
14	not converted	evergreen needleleaf forest
15	forest	mixed forest
16	water bodies	water bodies
17	vegetated low lying areas on regularly flooded soil	herbaceous wetland
18	not converted	wooded wetland
19	sparsely vegetated area	barren or sparsely vegetated
20	not converted	herbaceous tundra
21	not converted	wooded tundra
22	not converted	mixed tundra
23	not converted	bare ground tundra
24	permanent snow and ice	snow or Ice

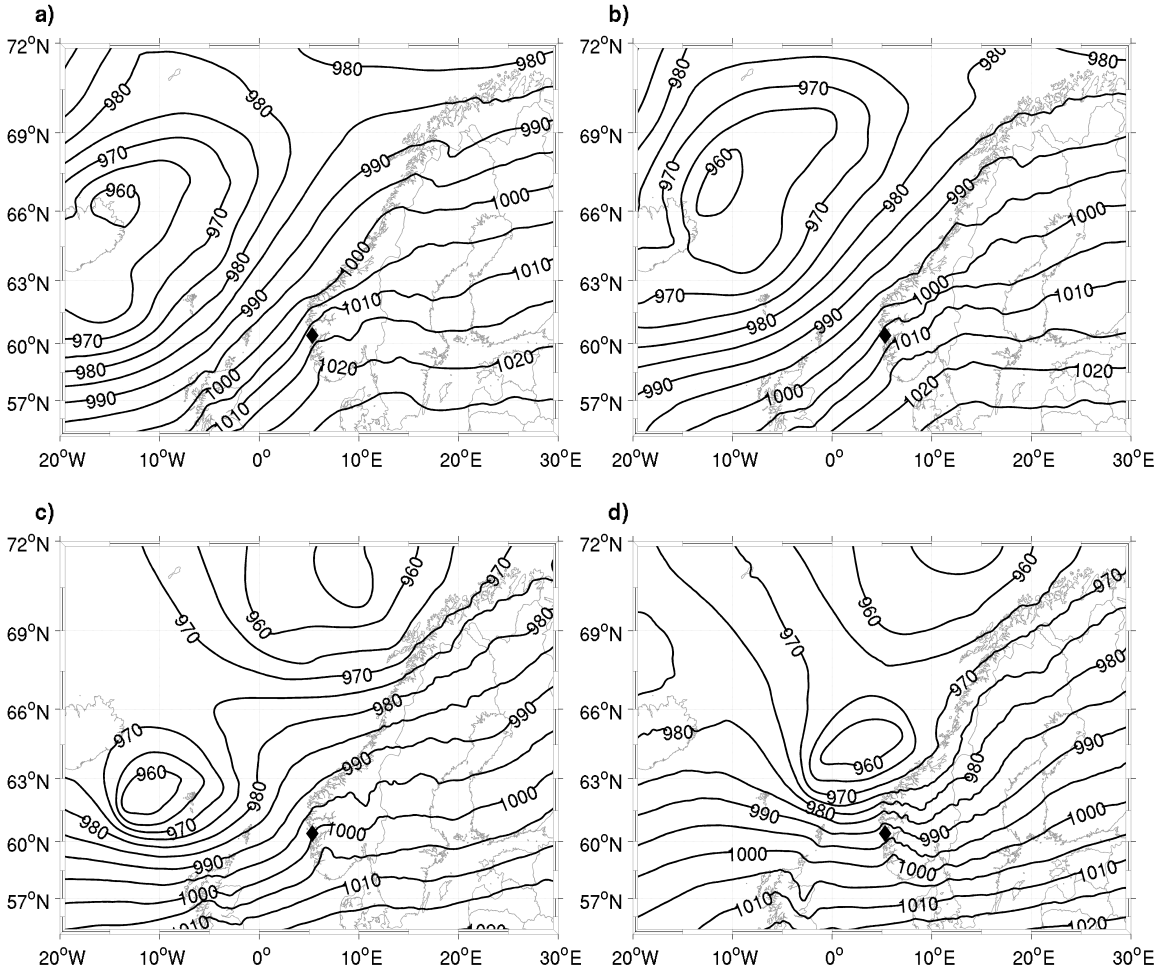

Figure 1. Mean sea level pressure at 1200 and 1800 UTC on 10 January 2009 (a and b) and 25 December 2011 (c and d). Based on analysis from the European Centre for Medium-Range Weather Forecasts. The location of Bergen is indicated with a black diamond.

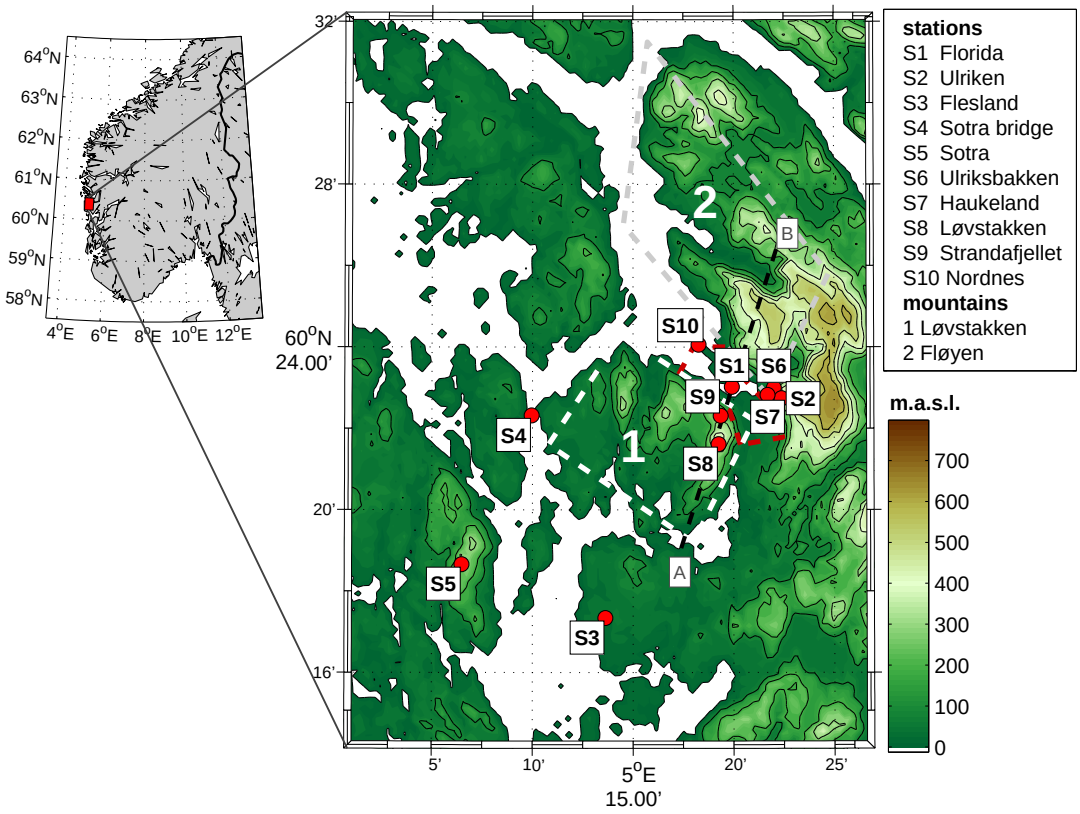

Figure 2. The topography of the area of main interest, the locations and names of the AWSs (S1-S10), and indications of the geographical extent of the two dominating mountain massifs in the area: Løvstakken (1) and Fløyen (2). The dashed, red line indicates the approximate extent of the centre of Bergen. The dashed, black line between the points "A" and "B" indicates the position of the cross section in Figure 14.

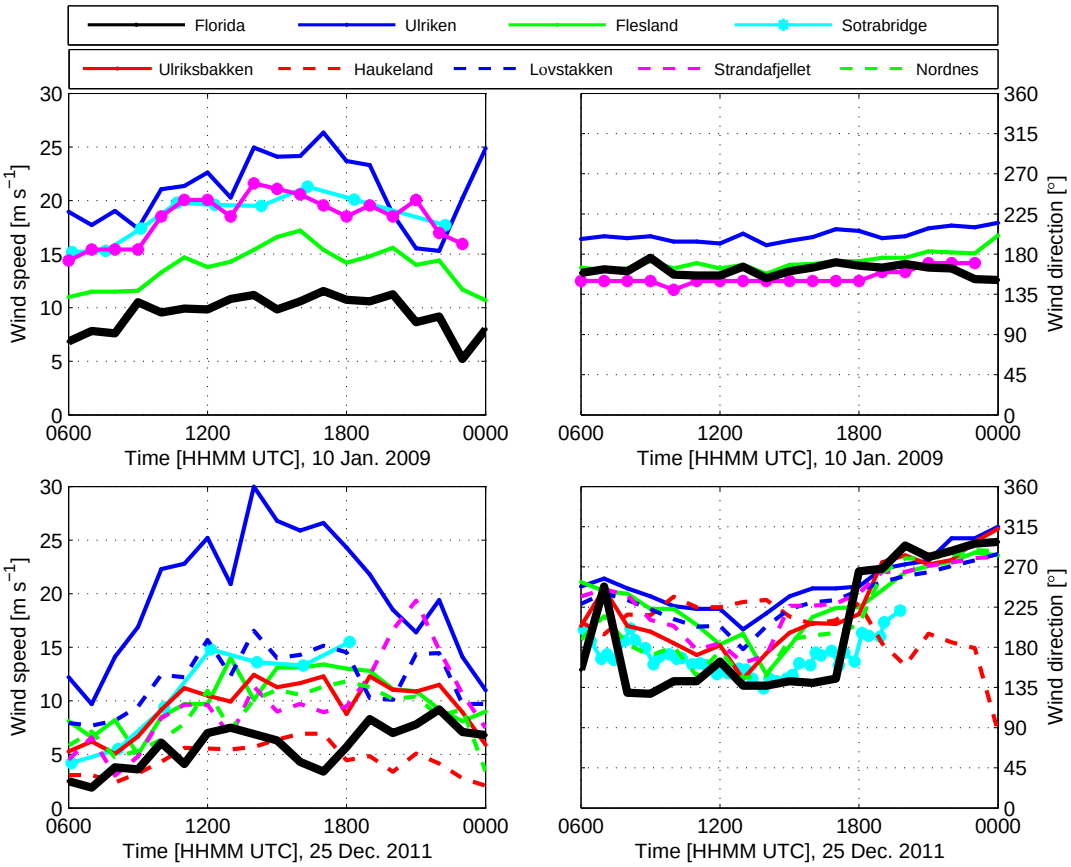

Figure 3. Observed wind speed and wind direction during the investigated windstorms on 10 Januar, 2009 and on 25 December, 2011 in the Bergen area.

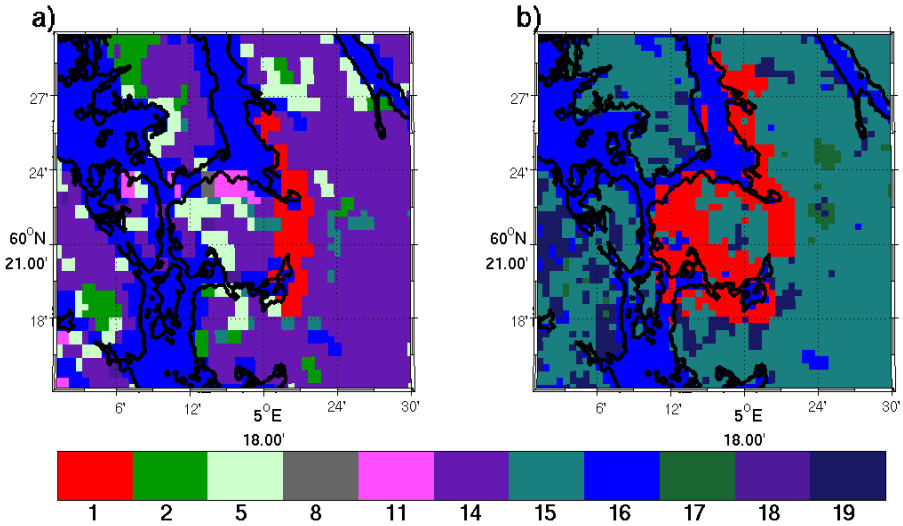

Figure 4. A zoom-in of the landuse of domain 3 (500 m horizontal resolution) using the datasets of a) USGS and b) GlobCorine. See Table 3 for a list over landuse categories and respective numbers indicated on the colorbar. The coastline from GSHHS is indicated with a solid, black line.

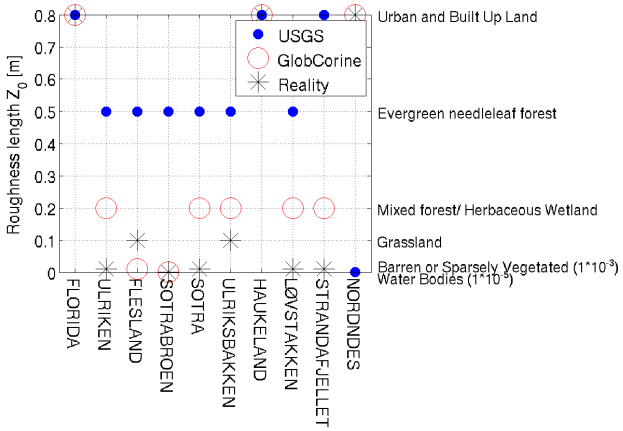

Figure 5. Roughness length for momentum at the different AWSs for the simulations using the USGS and GlobCorine landuse datasets. The real roughness length is indicated as well.

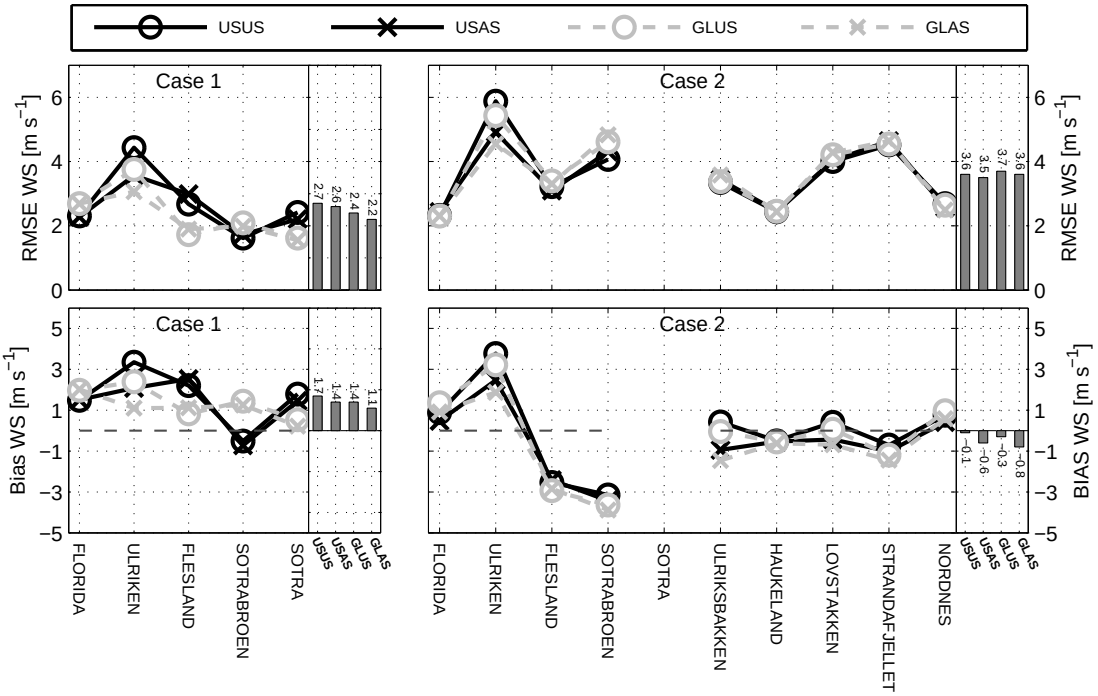

Figure 6. Root mean square error (RMSE) and mean error (bias) for wind speed (observed minus simulated) using four different combinations of model landuse and topography datasets. Table 1 lists and explains the different experiments. Case 1 is 10 January, 2009 and Case 2 is 25 December, 2011.

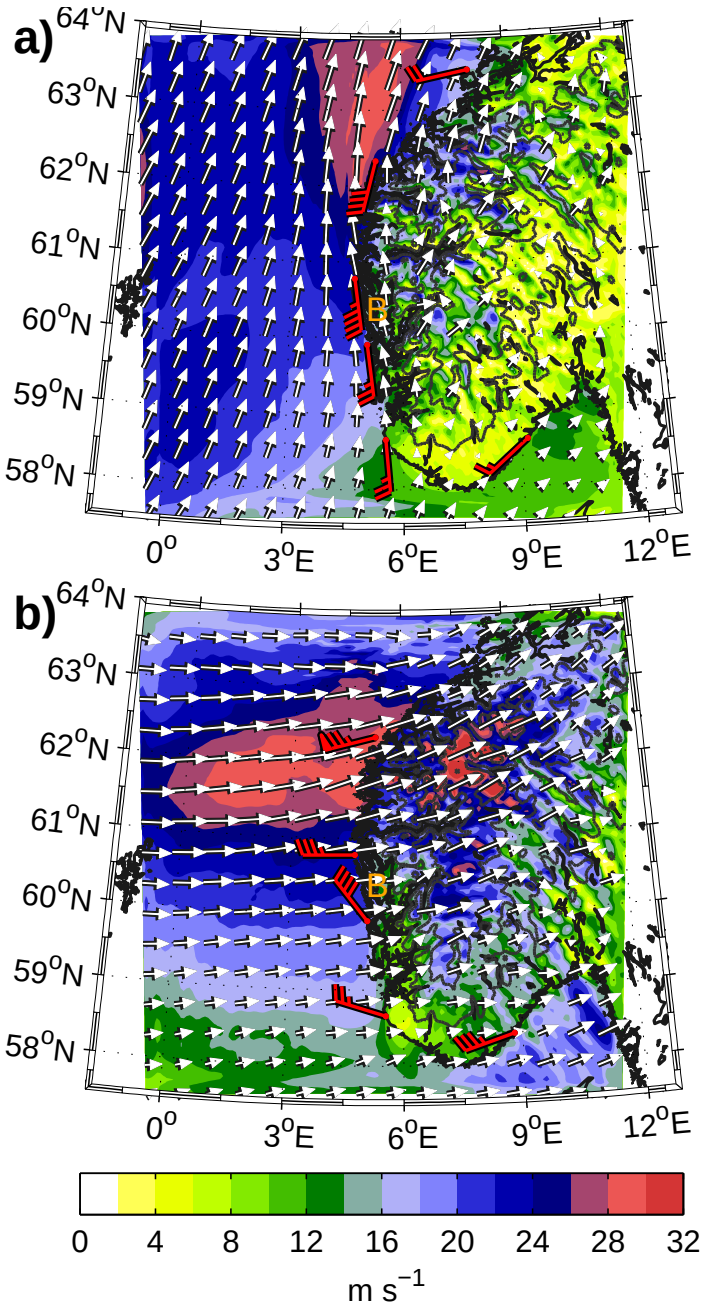

Figure 7. Simulated near surface (19.5 m.a.g.l.) horizontal wind speed at a) 1200 UTC on 11 Januar 2009 and at b) 2100 UTC on 25 December 2011. The results are from the outermost domain (4.5 km horizontal resolution). Observations from selected AWSs along the coast are indicated with red wind barbs. Each barb is 2.5 m s^{-1}. The location of Bergen is indicated with a "B".

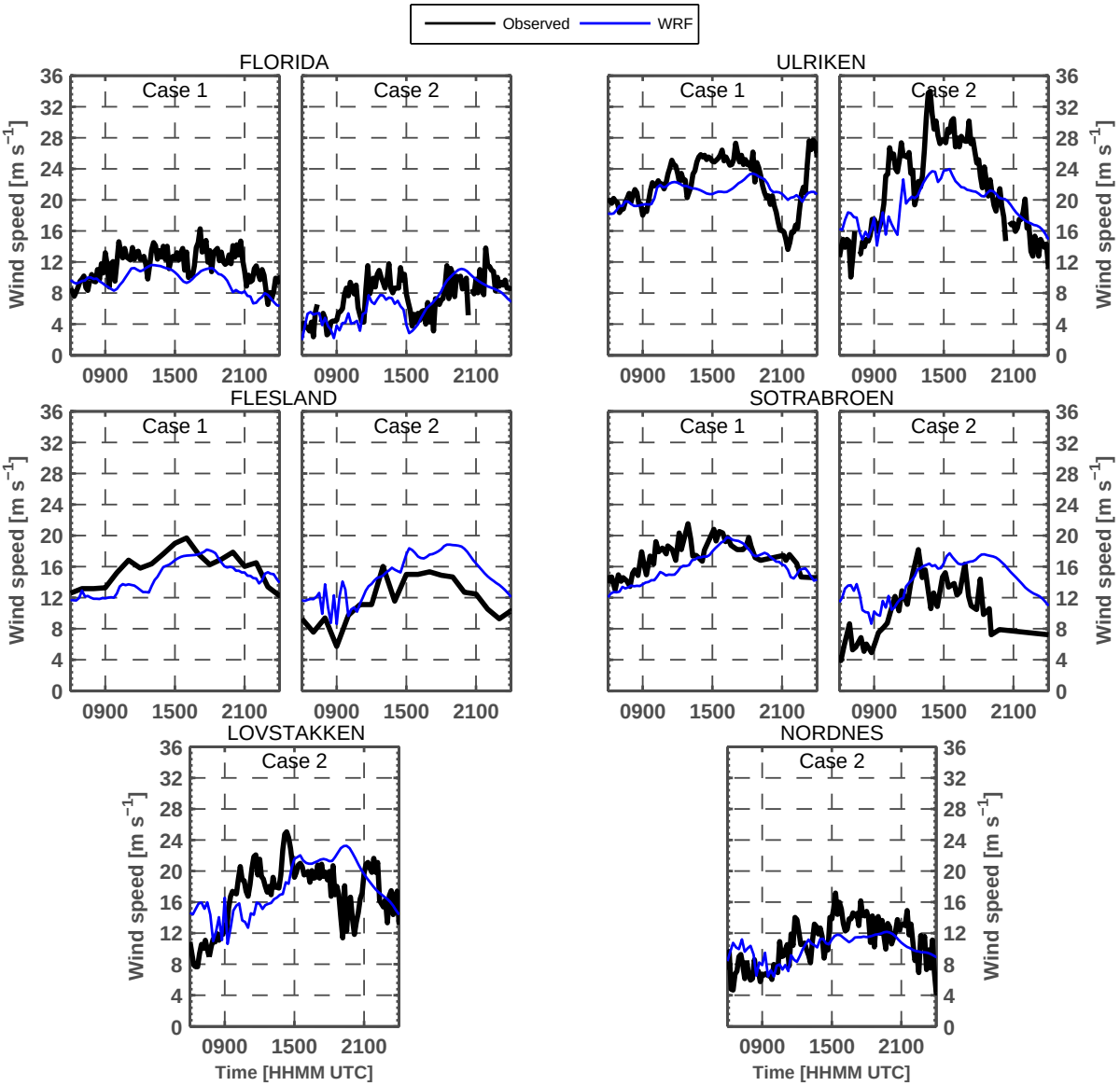

Figure 8. Observed and simulated wind speed at selected AWSs on 10 Januar 2009 (Case 1) and 25 December 2011 (Case 2). The simulation results are from the innermost domain (500 m horizontal resolution).

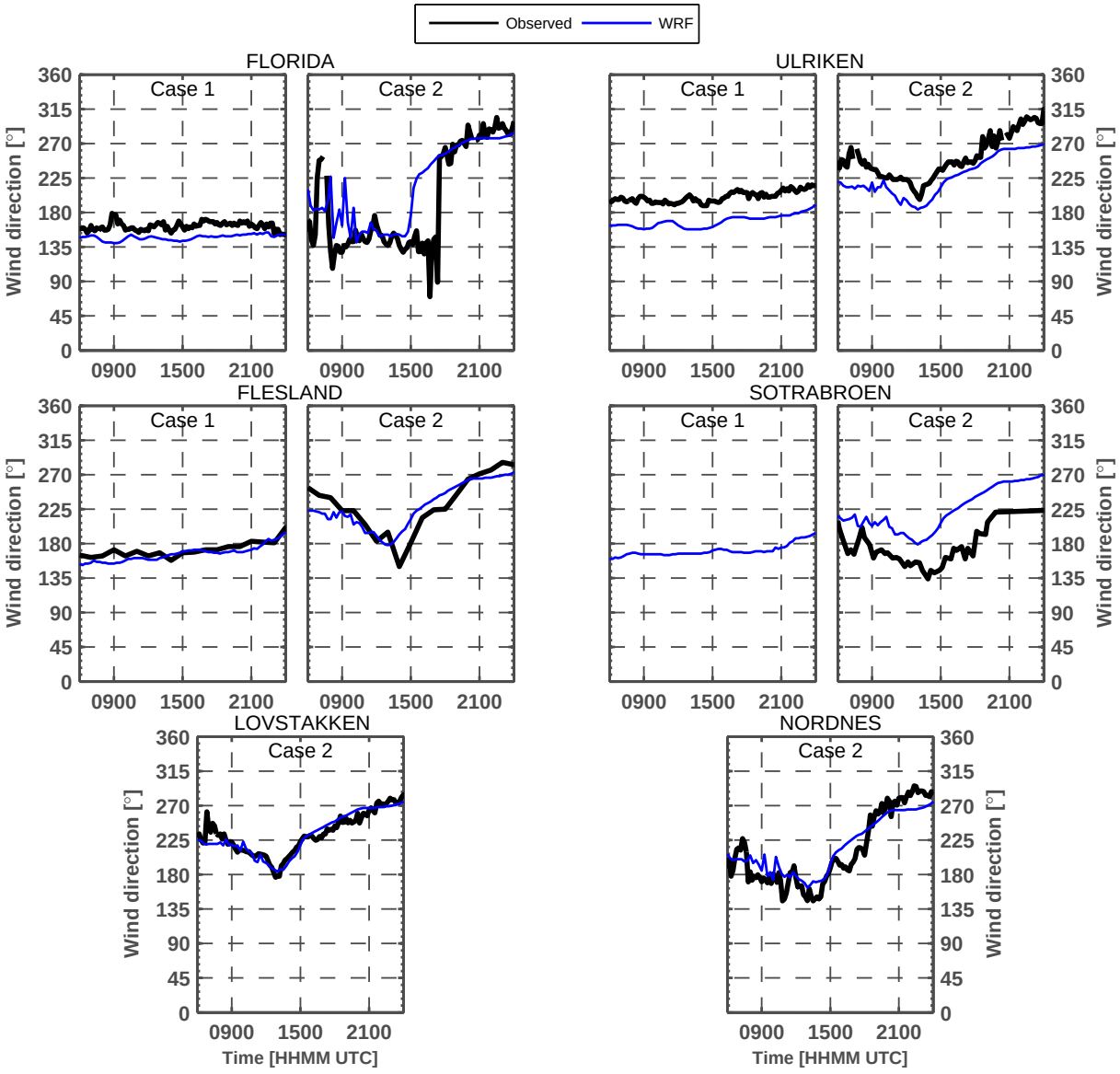

Figure 9. As in Figure 8, but for wind direction.

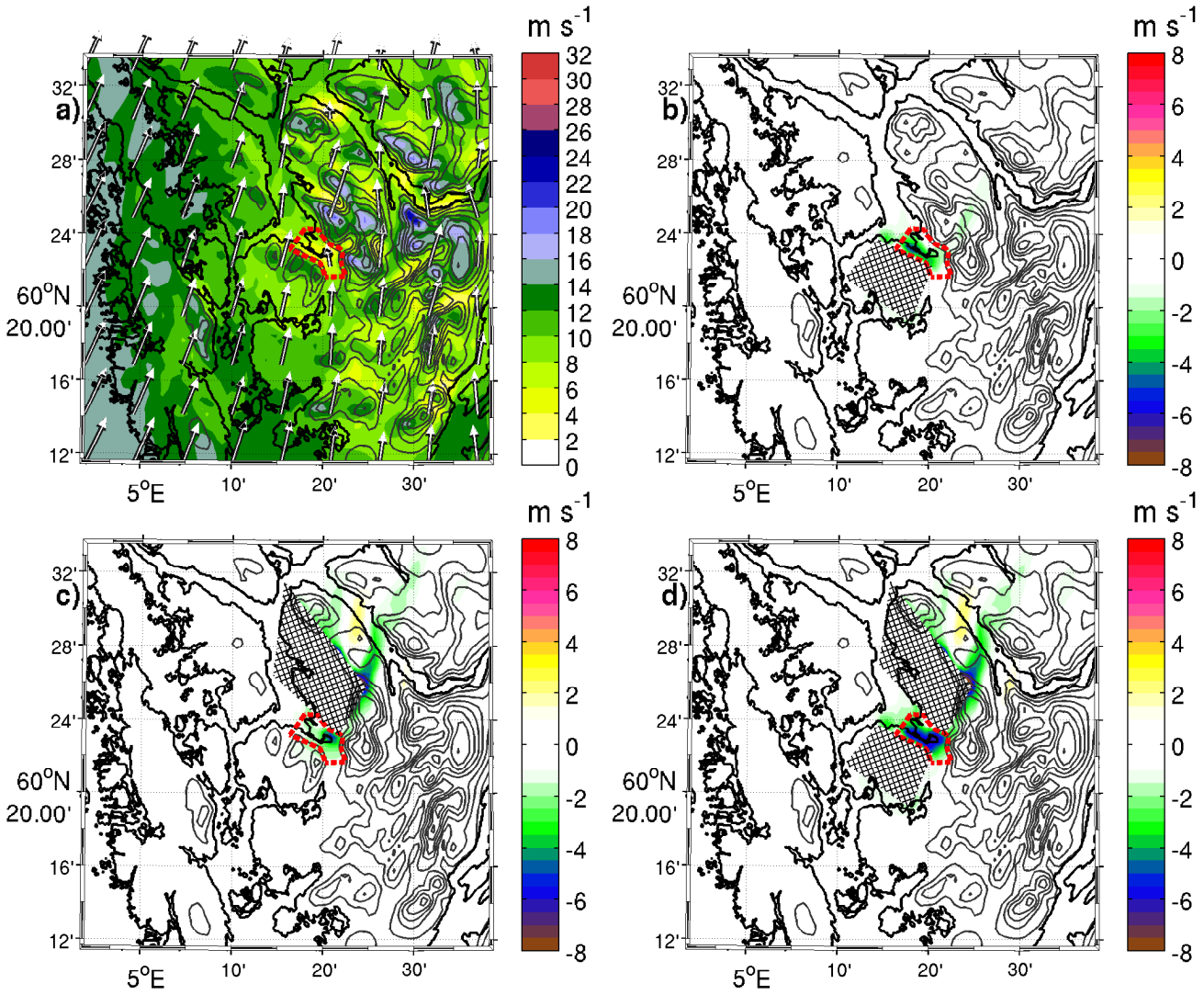

Figure 10. a) near surface wind speed at 0000 UTC on 11 January in the CTRL simulation, b) wind speed in CTRL minus NOL, c) wind speed in CTRL minus NOF, and d) wind speed in CTRL minus NOFL. The dashed, red line indicates the approximate extent of the centre of Bergen.

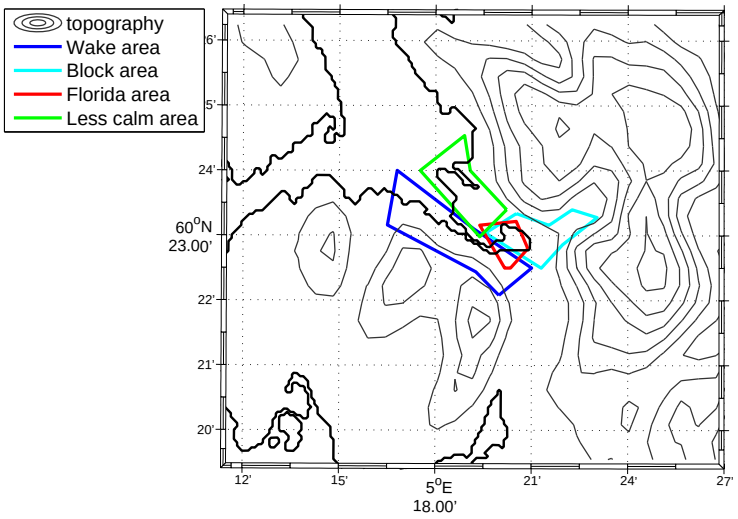

Figure 11. Areas of characteristic location and flow patterns. The terrain height is given with contours every 100 m.

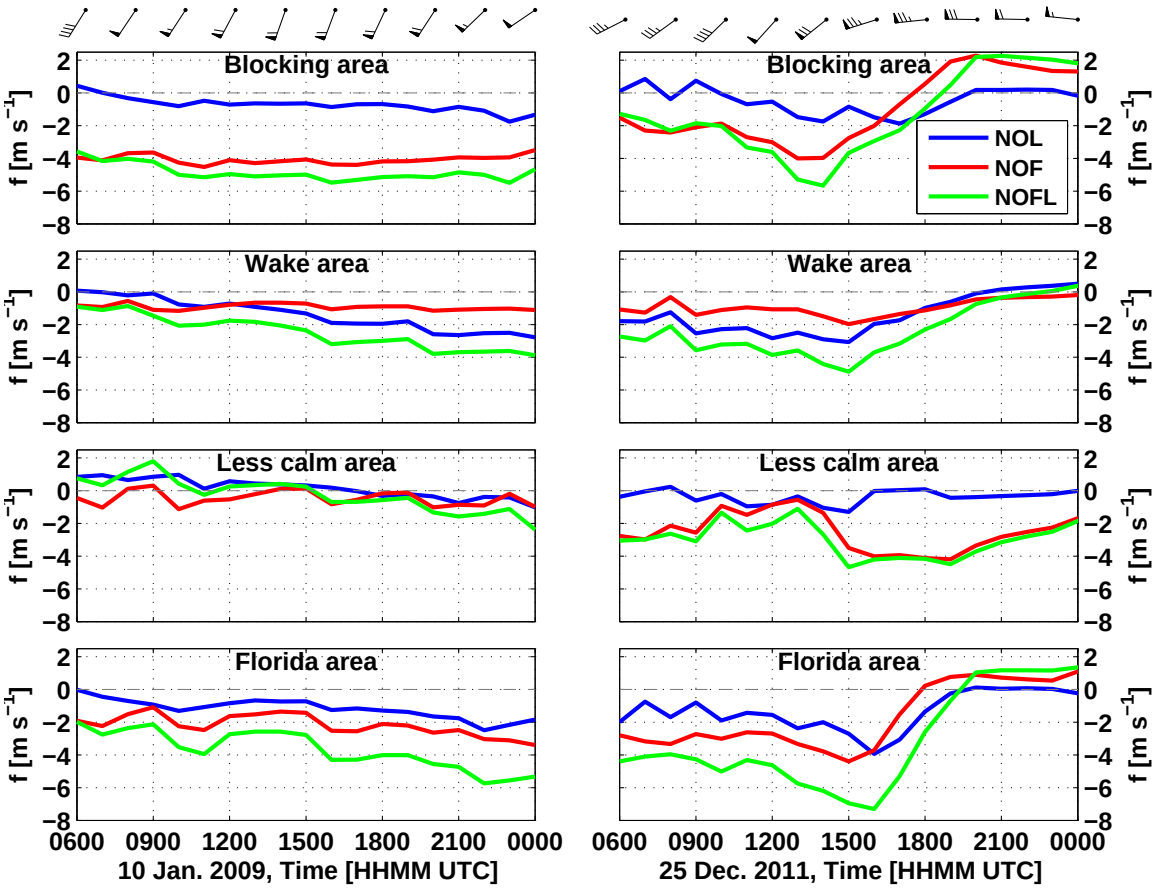

Figure 12. Difference in simulated near surface wind speed between the CTRL and the sensitivity simulations with topography modifications averaged within the areas indicated in Figure 11. The wind barbs at the top of the panels denote the simulated wind speed and direction at 900 hPa averaged within a box centred at 4.3°E and 61°N. Each half barb is 2.5 m s^{-1}.

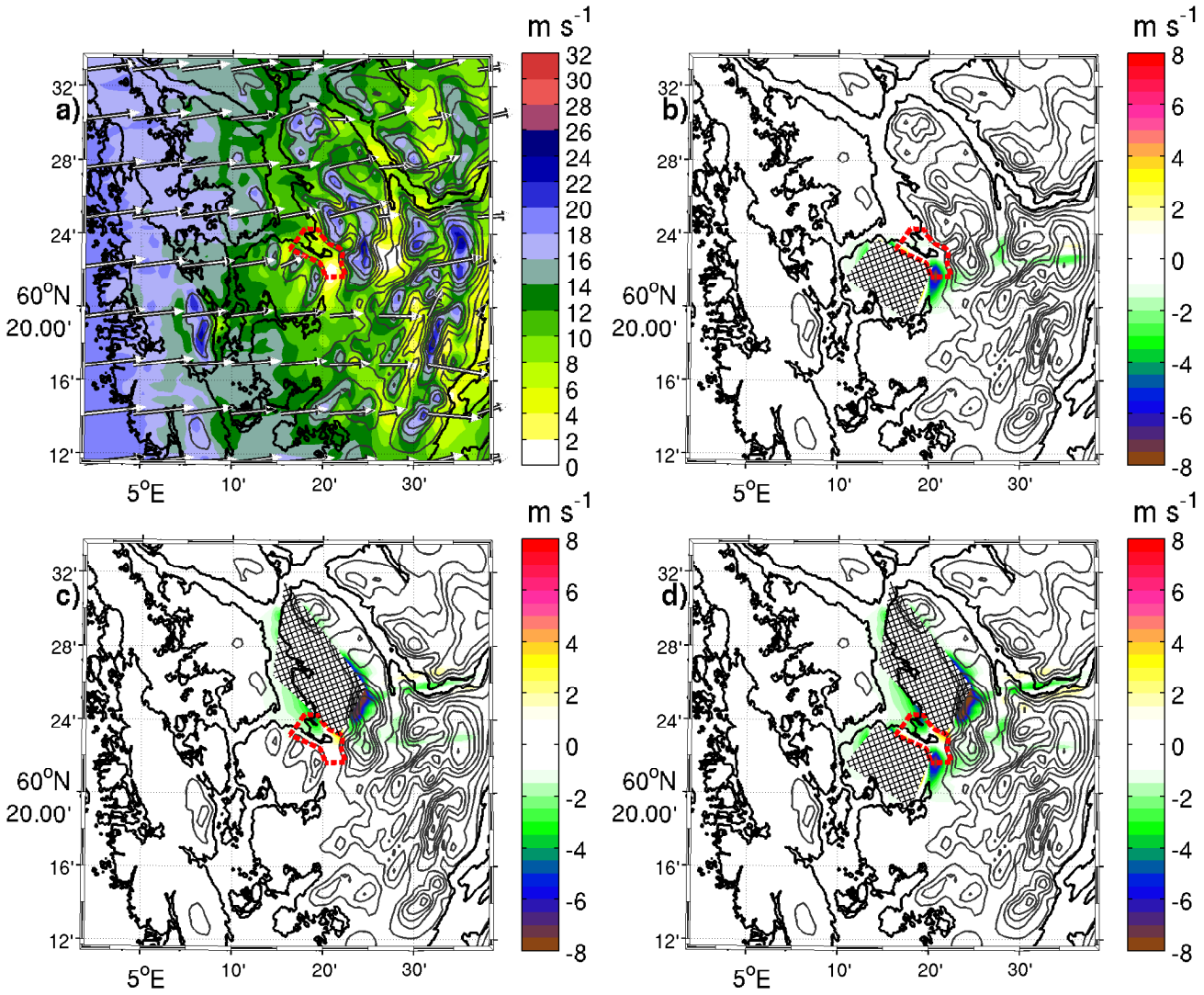

Figure 13. Same as in Figure 10, but for 2100 UTC on 25 December, 2011.

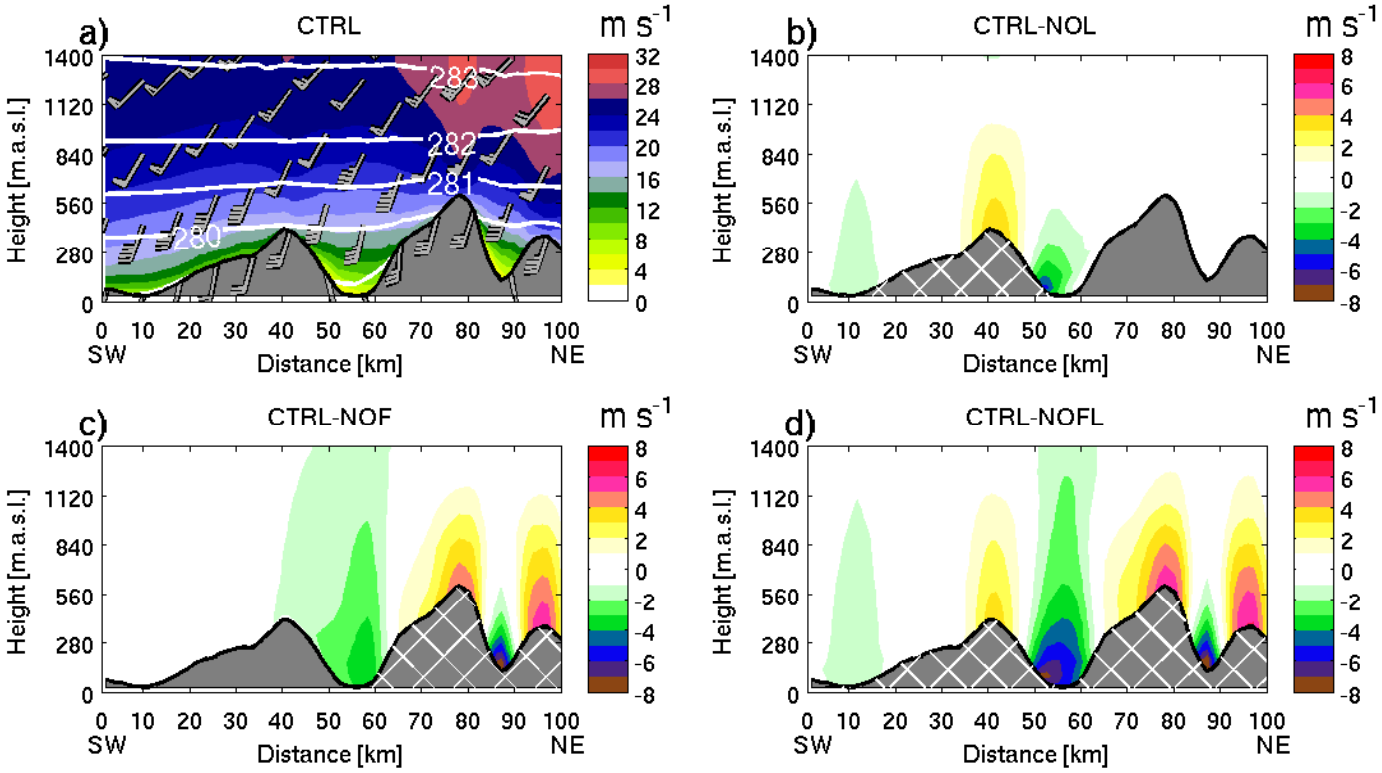

Figure 14. a) cross section of horizontal wind speed at 0000 UTC on 11 January in the CTRL simulation, b) wind speed in CTRL minus NOL, c) wind speed in CTRL minus NOF, and d) wind speed in CTRL minus NOFL. The geographical location of the cross section is indicated in Figure 2.

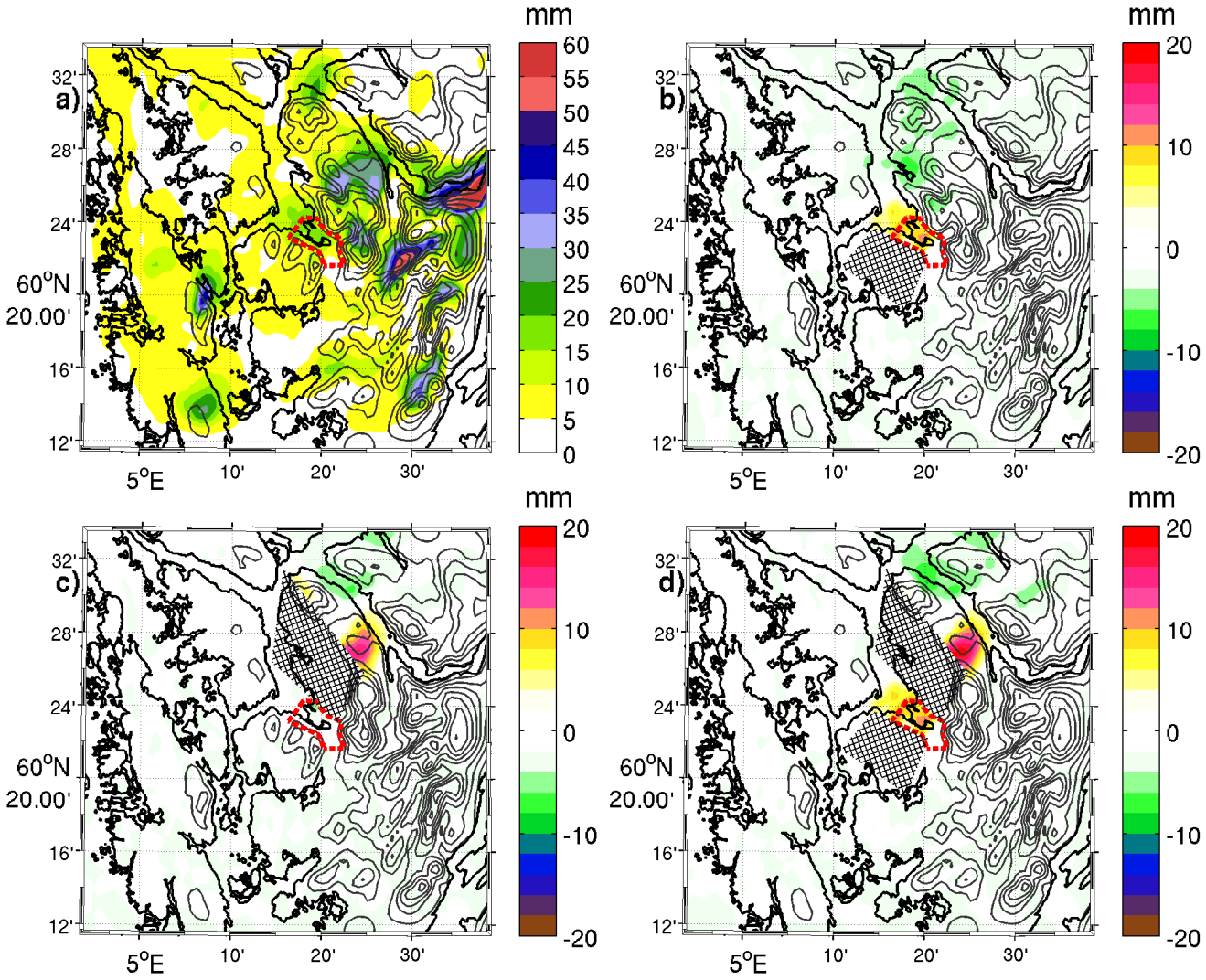

Figure 15. a) 18 hour accumulated precipitation at 0000 UTC on 11 January, 2009, in the CTRL simulation, b) precipitation in CTRL minus NOL, c) precipitation in CTRL minus NOF, and d) precipitation in CTRL minus NOFL.

Paper 3

Impact of surface characteristics on flow over a mesoscale mountain
Jonassen, M. O., Ágústsson, H. and Ólafsson, H.
Submitted to Quarterly Journal of the Royal Meteorological Society

Impact of surface characteristics on flow over a mesoscale mountain

Marius O. Jonassen,[a*] Hálfdán Ágústsson[b] Haraldur Ólafsson[ac]

[a]*Bergen School of Meteorology, Geophysical Institute, University of Bergen*

[b]*Dpt. of Physics, University of Iceland. Institute for Meteorological Research and Icelandic Meteorological Office. Reykjavík Iceland.*

[c]*Dpt. of Physics, University of Iceland and Icelandic Meteorological Office. Reykjavík Iceland.*

[*]Correspondence to: Geophyical Institute, University of Bergen, Allégaten 70, 5007 Bergen, Norway. E-mail: marius.jonassen@gfi.uib.no

Dynamic downscaling of atmospheric flow over Iceland has revealed that downslope wind maxima are not merely a seldom extreme event, but rather a prominent climatological signal. Based on two cases from the international FLOHOF field campaign of flow over and around the Hofsjökull glacier, the impact of surface roughness and surface fluxes on the flow field is explored by means of several numerical sensitivity experiments. The experiments show a very strong sensitivity of the downslope flow acceleration to the surface roughness: a rough surface almost destroys the downslope windstorm at the surface, but increases the winds aloft above the downstream slope. Surface heating too has a detrimental impact on the downslope flow acceleration, but the effect is lower than for the surface roughness. The surface heating's impact is higher for a rough surface than for a smooth surface. The variability of the impact of the surface fluxes on the wind speed can be understood by referring to the vertical wind profile and turbulent mixing. This study is not only of general relevance through its exploration of factors affecting downslope flow acceleration of stably stratified flow, but it is also of interest because glaciers retreat rapidly in a changing climate. Copyright © 0000 Royal Meteorological Society

Key Words: gravity waves, downslope winds, surface roughness, surface heating, Iceland

Prepared using qjrms4.cls

Received

1. Introduction

Several investigations have revealed a detrimental effect of surface friction on mountain waves and downslope flow acceleration (e.g. Richard *et al.* 1989; Georgelin *et al.* 1994; Ólafsson and Bougeault 1997a; Epifanio and Qian 2008). Peng and Thompson (2003) hypothesized that the reduction in mountain-wave amplitude and drag in the presence of surface friction is due to the reduction in the slope of the atmospheric boundary layer (ABL) height as compared to the terrain height, which is based on the comprehensive standpoint of viewing separately the ABL and the stratified layer above. The suppressing effect of surface friction on waves in real flows has also been confirmed for a collection of flows during the PYREX campaign (Ólafsson and Bougeault 1997b) and subsequently on several individual cases of downslope flow.

The thickness of the ABL may be increased by heat from the surface, giving stronger waves when there is surface cooling or weaker waves when there is surface heating. Among the first to document the effect of surface fluxes on mountain flow analytically was Raymond (1972), who solved a non-diabatic form of Long's equation. Using linear theory and idealised simulations, Doyle *et al.* (2005) found that adiabatic cooling acts to increase the wave amplitude and the potential of wave breaking for flow over Greenland. They argued that the cooling acts to augment the effective mountain height. Smith and Skyllingstad (2011) did a series of idealised 2D simulations of mountain flow and found katabatic winds to significantly enhance downslope flow in the presence of surface cooling and a strong low-level inversion. These results on diabatic heating and cooling are in agreement with downslope windstorms being more frequently observed in the night than during daytime (e.g. Brinkmann 1974; Jiang and Doyle 2008; Valkonen *et al.* 2010). To our knowledge, the combined effect of surface roughness and surface heat fluxes has not been studied previously.

The reduction or enhancement of mountain waves through the above described processes, have potentially large impacts on the general atmospheric circulation; orographic drag is a significant sink in the atmospheric momentum budget (e.g. Lilly 1972; Wahr and Oort 1984). On the smaller scale, modification of mountain waves and the horizontal extension of downslope flows caused by changes in the underlaying surface, can have a large impact on local vegetation and general land coverage characteristics.

Mountain flows have been diagnosed through a number of different parameters. A central parameter in this respect is the non-dimensional mountain height Nh/U (e.g. Smith and Grønås 1993), in which N is the Brunt-Väisälä frequency, h is the obstacle (mountain) height, and U the typical wind speed of the upstream background flow. Based on this parameter, Smith (1989) describes the following basic flow regimes: Low values of Nh/U enable the flow to pass over the mountain without any upstream stagnation and typically gentle gravity waves are formed. Nh/U can be seen as a measure of the non-linearity in the flow, and linear theory describes the response well in this range (Gill 1982). For values of Nh/U close to unity, the flow enters a high drag state. In this state, there are typically amplified and even breaking gravity waves and strong downslope flow acceleration on the mountain's lee side. For higher values of Nh/U, the waves become less prominent, while an upstream blocking is a more dominant feature in the flow morphology.

In the present study, flow over the Hofsjökull ice cap in Central Iceland is explored. The flow is simulated with realistic surface conditions and compared to observations that were made during the FLOHOF field campaign in 2007 (Reuder *et al.* 2011). In a set of numerical sensitivity experiments, the flow is also simulated with increased surface friction and no ice cover in the area presently covered by ice. The purpose of the study is primarily to explore the atmospheric flow field over a mesoscale ice cap and the impact of surface friction and surface heating on

the flow. The study is motivated by indications of persistent downlope windstorms over Hofsjökull (Rögnvaldsson *et al.* 2007) and at several other locations in Iceland (Ágústsson and Ólafsson 2007, 2012; Rögnvaldsson *et al.* 2011), but no less of the predictions of climate change leading to the disappearance of the ice cap, leaving a surface that is not only significantly rougher, but also warmer during daytime in the summer.

2. Climatology of summertime northeasterly flow over Iceland and Hofsjökull

We will first consider high resolution (3km in the horizontal) dynamic downscaling of data from the RÁV project (Rögnvaldsson *et al.* 2007) to briefly investigate the climatological mean wind patterns over Iceland in general and Hofsjökull in specific for northeasterly summertime flow.

Figure 1 shows the mean near surface wind speed over Iceland for situations with wind speeds above 5 m s^{-1} and wind directions within the sector 45° +/- 22.5° over the top of Hofsjökull for the months June, July, August and September. At the coast, the lowest wind speeds are found in the northeast and in the southwest of Iceland. These minima's geographical locations and spatial extensions suggest that they are associated with large scale blocking and wake effects. Offshore, the strongest winds are found along the southeastern and northwestern coast. Onshore, the strongest winds are found above the downstream slope of the larger ice caps. A closer look at the Hofsjökull area (Figure 2), shows relatively low wind speeds immediately upstream and a few kilometres downstream of Hofsjökull indicating local blocking and wake effects. The strongest wind speed is located downstream of the mountain top. The cross-section (Figure 3) shows that the downslope acceleration is relatively shallow, while the wake extends far aloft.

3. Observations

3.1. The FLOHOF field campaign

The observational data used in the present study, were obtained during Flow Over and around Hofsjökull (FLOHOF), an international field campaign that took place from 21 July to 24 August, 2007 on and in the vicinity of the Hofsjökull glacier in Central Iceland. The main aim of the campaign was to investigate the response of gravity waves above a mountain to changes of mean inflow with time and wave transience. The campaign was the first to address this topic by observational means. Hofsjökull (1,782 m.a.g.l.) rises some 1000 m above its surroundings and has a diameter of approximately 30-40 km. Its unique, nearly circular shape and smooth ice-covered surface makes it an ideal field laboratory for the study of mountain flows. The limit of permanent snow/ice follows roughly the 1000 m contour. A more detailed description of FLOHOF can be found in Reuder *et al.* (2011).

3.1.1. Automatic weather stations

During the FLOHOF campaign, a network of 19 automatic weather stations (AWS) was erected on and around the glacier, recording the basic meteorological parameters temperature: wind direction, wind speed, relative humidity, pressure and precipitation. The AWSs were placed to obtain an as homogenous network of measurements as possible, but with the restriction of accessibility. Consequently there is some lack of observations in the western and eastern parts of the glacier that proved hard to reach. The AWSs were inspected regularly during the campaign to ensure continous data series, but icing at the wind sensors did occur at some instances, especially during northerly flow on the AWSs situated on the glacier.

3.1.2. Small Unmanned Meteorological Observer - SUMO

The atmospheric profiles used for model validation in the present study were obtained from a location southwest

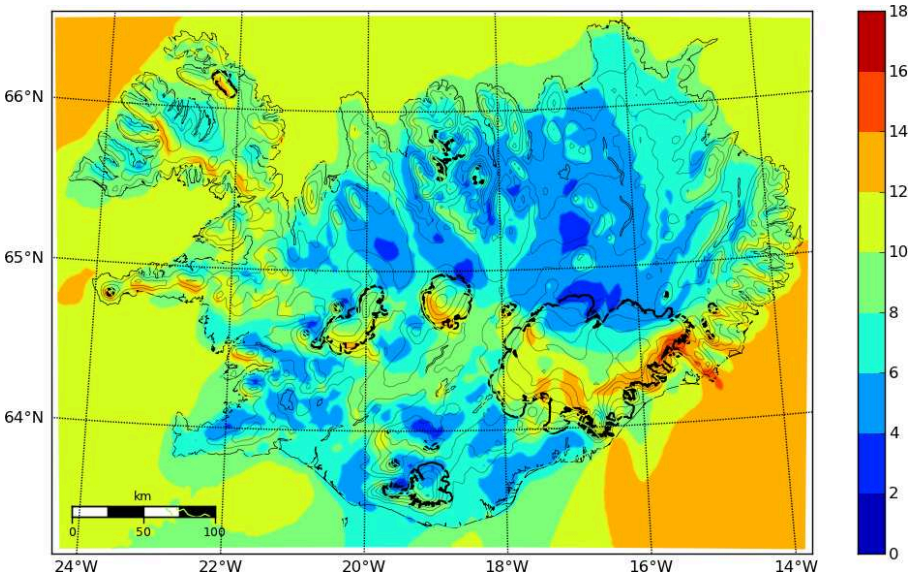

Figure 1. Mean near surface wind speed [m s^{-1}] over Iceland for cases with northeasterly flow. The results are based on ECWMF analysis data downscaled with WRF at a 3 km horiontal resolution for the years 1995-2008. The major glaciers are outlined.

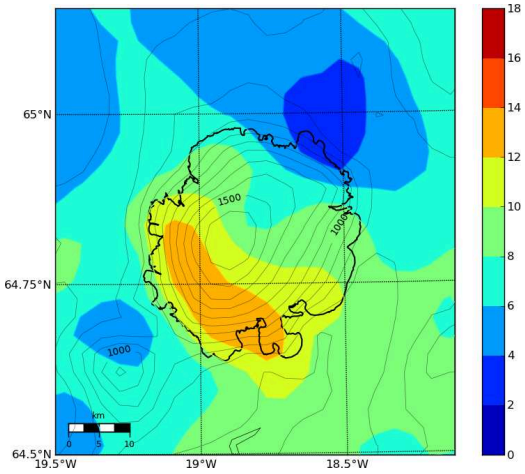

Figure 2. Same as in Figure 1, but for an area around the Hofsjökull glacier in Central Iceland.

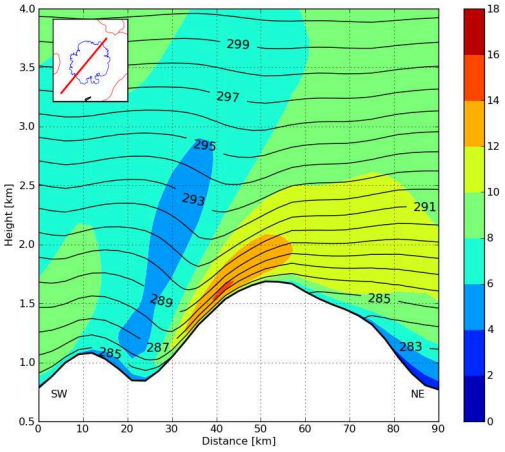

Figure 3. Same as in Figure 2, but for a vertical cross section of horizontal winds over Hofsjökull.

of Hofsjökull (Figure 4) using the Unmanned Aerial System (UAS) SUMO. The SUMO flight pattern used for atmospheric profiling resembles a helix that corresponds to an atmospheric column with a radius of 50-100 m.

Due to SUMO's configuration, reliable wind observations are available from approximately 100 m.a.g.l. and up to around 100 meter below each profile's maximum altitude. Temperature and relative humidity observations are available from the whole vertical extent of the profiles. More detailed information on SUMO can be found in Reuder *et al.* (2009) and Mayer *et al.* (2011).

4. Numerical simulations

4.1. High resolution simulations

The atmospheric flow above Mt. Hofsjökull on 13 and 14 August, 2007 is simulated at high horizontal resolution using the WRF-model (Skamarock *et al.* 2008). The model is initialized and forced at its boundaries with model level data (91 vertical levels) from the ECMWF operational analysis with a horizontal resolution of 0.125 degrees. It is run at a resolution of 9, 3 and 1 km with respectively 85 x 90, 187 x 157 and 82 x 82 gridpoints in the 2-way nested domains (Figure 5).

There are 51 σ-layers in the vertical, which are terrain following at lower levels but flatten gradually towards the top of the model at 50 hPa. The lowermost model half level is at about 9 m.a.g.l. The model is run for a total of 48 hours, starting on 13.08.2007 at 0000 UTC and the first 6 hours are considered as spin-up and thefore not included in the analysis part of this study. The Mellor-Yamada-Janjic scheme (Janjić 2001; Mellor and Yamada 1982; Janjić 1994) is used for boundary layer parameterisation. The RRTM scheme (Mlawer *et al.* 1997) is employed for long wave radiation, the Dudhia scheme (Dudhia 1989) for short wave radiation, and the Unified NCEP/NCAR/AFWA Noah land-surface model (Chen and Dudhia 2001) with soil temperature and moisture in four layers for surface physics. The parameterisation of microphysics is done using the WSM 3-class simple ice scheme (Dudhia 1989; Hong *et al.* 2004), which includes cloud water/ice, and rain/snow as prognostic variables. Apart from the innermost domain, the setup is nearly identical to that of the numerical simulations by Reiknistofa í veðurfræði (RV) which are used for operational forecasting at the Icelandic Meteorological Office (Veðurstofa Íslands) and published online at: "http://belgingur.is" (the HRAS-system). The extents of the Icelandic ice caps in the default WRF landuse dataset from the U.S. Geological Survey (USGS) are far too large. In this study, we therefore use an updated version of the USGS landuse dataset with more realistic ice cap extents provided by RV.

4.1.1. Sensitivity experiments

Four numerical simulations have been made, each with differing combinations of model landuse and roughness length of momentum (z_0) over the Hofsjökull ice cap. Simulation 1) is the control simulation, here named "Smooth glacier (CTRL)" for consistency with the names of the other simulations. In the Smooth glacier simulation, the original 'Snow or ice' landuse is kept and the z_0 over the ice cap is 0.001 m. In simulation 2), "Rough noglacier", the original 'Snow or Ice' landuse on the ice cap of Hofsjökull is replaced with the land surface dominating its surroundings, named 'Mixed Tundra', which has a z_0 of 0.15 m. In Simulation 3), "Rough glacier", the landuse is kept as default, i.e. with an intact ice cap, but with a z_0 for the 'Snow or Ice' landuse category set to 0.15 m. In simulation 4) "Smooth noglacier", the landuse over Hofsjökull is set to a dummy landuse category that shares all properties with 'Mixed Tundra', except z_0, which is equal to that of 'Snow or Ice'. An overview of the simulations and their respective landuse properties are given in Table 1.

Table 1. Numerical sensitivity experiments. The surface type refers to the model landuse covering the extent of the Hofsjökull ice cap, as shown in Figure 4.

Name	z_0 (m)	Surface type
Smooth glacier (CTRL)	0.001	snow or ice
Rough noglacier	0.15	mixed tundra
Rough glacier	0.15	snow or ice
Smooth noglacier	0.001	mixed tundra

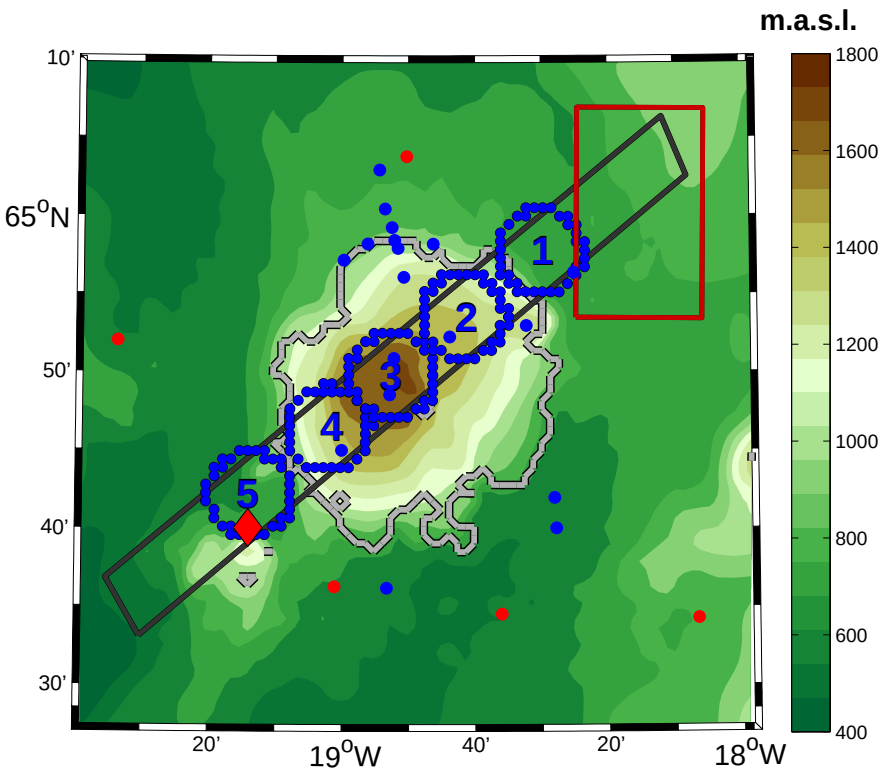

Figure 4. Map over the Hofsjökull area (corresponding to domain 3). The blue, dotted circles indicate the following five areas: 1) Upstream, 2) Upslope, 3) Mountain top, 4) Downslope, and 5) Downstream. The solid, black rectangle running from the southwest to the northeast marks the location of the time averaged wind profiles in Figure 11 and vertical cross section in Figure 14. The red diamond is the UAS SUMO launch location. The location of the Hofsjökull ice cap and thus the area affected by the model landuse modifications done in the sensitivity simulations is encircled by a grey, solid line. Atmospheric data from a 1000 m high vertical column spanning the red rectangle in the upper right corner are used to estimate upstream flow conditions.

5. Results

5.1. *Case studies, 13 and 14 August, 2007*

During 13 and 14 August 2007, Iceland was embedded in a northeasterly flow set up by a low pressure over the British isles and a high pressure over Greenland (Figure 5). Figure 6 gives a detailed overview of the near surface flow over Iceland on 13 August. It shows the simulated near surface (9 m.a.g.l.) wind speed and direction at 1200 UTC in domain 2 (3 km horizontal resolution). The wind field bears close resemblence with the average winds for northeasterly flow situations as calculated from downscaled climate simulations for Iceland (Figure 1). Offshore, the strongest winds are found in the southeast and the weakest winds in the wake to the south of Iceland. Over land, the strongest winds are located above the downstream slopes of the large ice caps. In domain 3 (Figure 7, 1 km horizontal resolution), located over the area of Hofsjökull, the downstream acceleration of winds over the ice cap is more clearly seen. The simulated flow compares reasonably well to available AWS data spread around Iceland for domain 2 and the stations on and around Hofsjökull for domain 3. The wind speed measured by the AWS on the lee-side slope of Hofsjökull confirms the relatively strong wind there. A more detailed model validation against the AWS data can be found in Mayer *et al.* (2010), who used the same basic model setup as in the present study to simulate cases from FLOHOF.

5.2. *The flow aloft in the lee of Hofsjökull*

During both 13 and 14 August, several soundings were made with the UAS SUMO downstream of Hofsjökull. These soundings (Figures 8 and 9) reveal a multi-layered atmospheric structure from the ground level and up to around 1200 m.a.g.l., which is slightly higher than the height at which Hofsjökull reaches above its surroundings.

The wind direction below 1200 m.a.g.l. varies between northeasterly and southeasterly in the first two profiles on 13

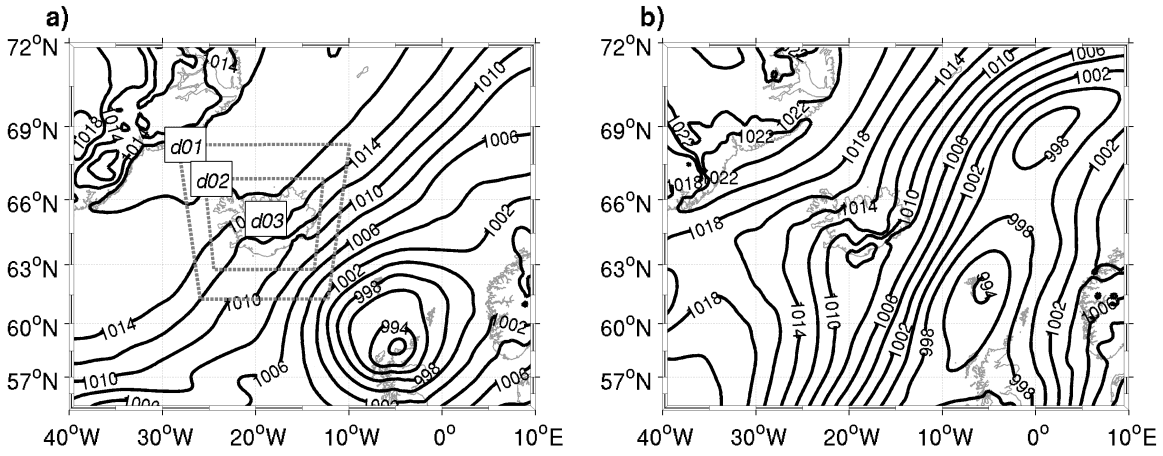

Figure 5. Mean sea level pressure (hPa) on a) 13 and b) 14 August 2007 at 1200 UTC obtained from ECMWF analysis. The locations of the three WRF domains are indicated in a).

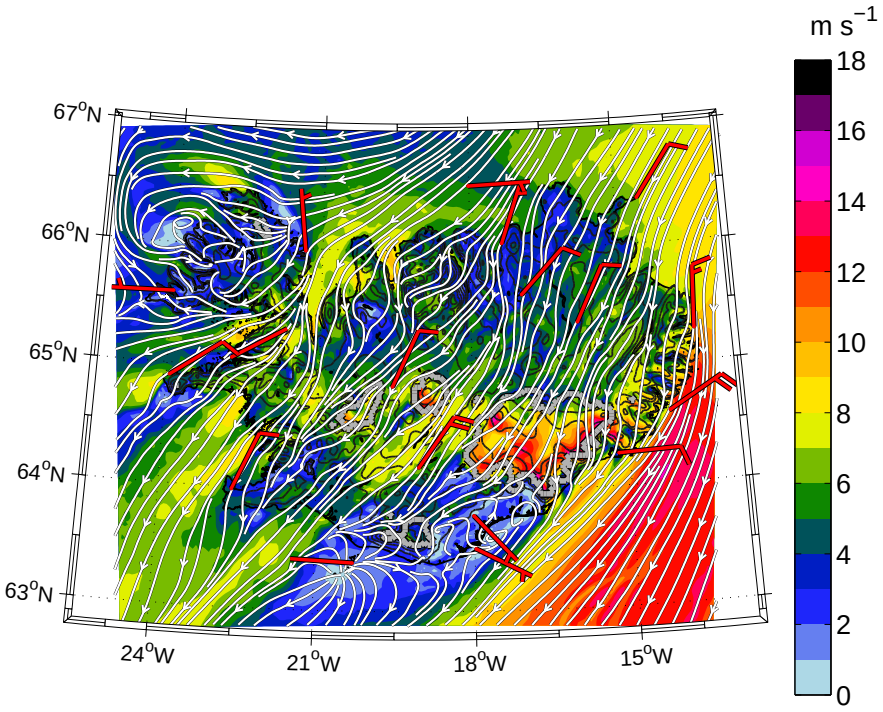

Figure 6. Simulated near surface (9 m.a.g.l.) winds from the CTRL simulation at 1200 UTC on 13 August for domain 2 (3 km horizontal resolution). Surface observations from automatic weather stations are indicated with wind barbs. Each half barb is 2.5 m s^{-1}. Terrain contours are given every 250 m.

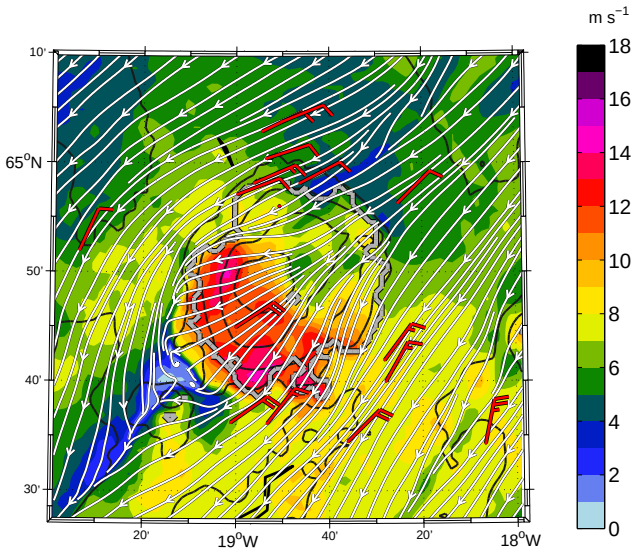

Figure 7. Same as in Figure 6, but for domain 3 (1 km horizontal resolution).

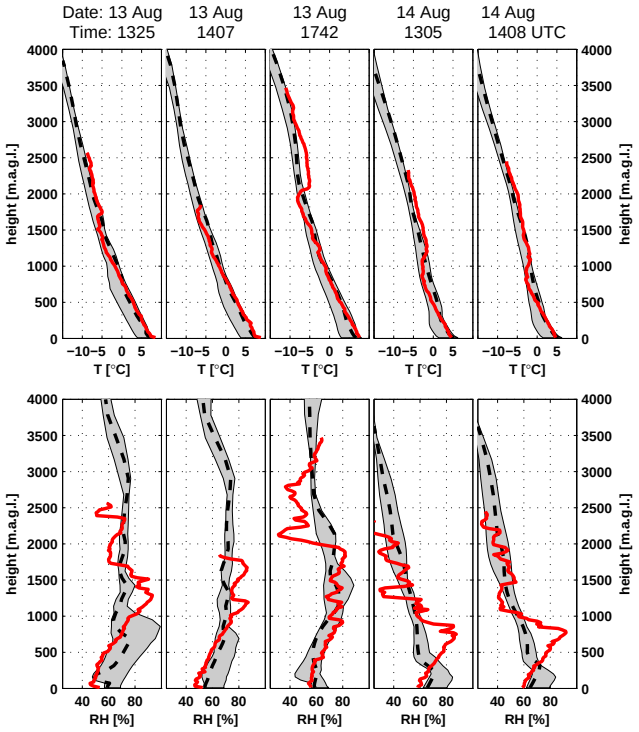

Figure 8. Observed and simulated vertical profiles of temperature [°C] and relative humidity [%] on 13 and 14 August 2007 downstream of Hofsjökull (location indicated in Figure 4). Red lines show the observations and dashed, black lines show the simulated profiles from the grid point closest to the observation location. The grey bands represent the minimum and maximum values within an atmospheric column spanning 4x4 km in the horizontal and centred at the grid point.

August (1325 and 1307 UTC) and the wind speed is below 5 m s^{-1}. The wind direction is more easterly (approximately 45 °) in the last profile on 13 August (1725 UTC) below 1200 m.a.g.l. than in the two first ones, coinciding more closely with what can be considered as the synoptic wind direction found further aloft. This lower layer (below 1200 m.a.g.l.) is capped by a wind minimum in all three profiles from 13 August. Correspondingly, there is a weak inversion and a drop in humidity at the top of this layer.

At higher elevations, 1800-2000 m.a.g.l., there is a stronger temperature inversion. This inversion is situated slightly below a wind maximum exceeding 10 m s^{-1}. A similar inversion is seen in the Keflavík sounding in Southwest Iceland (not shown), which might indicate the presence of a larger-scale subsidence inversion. On 14

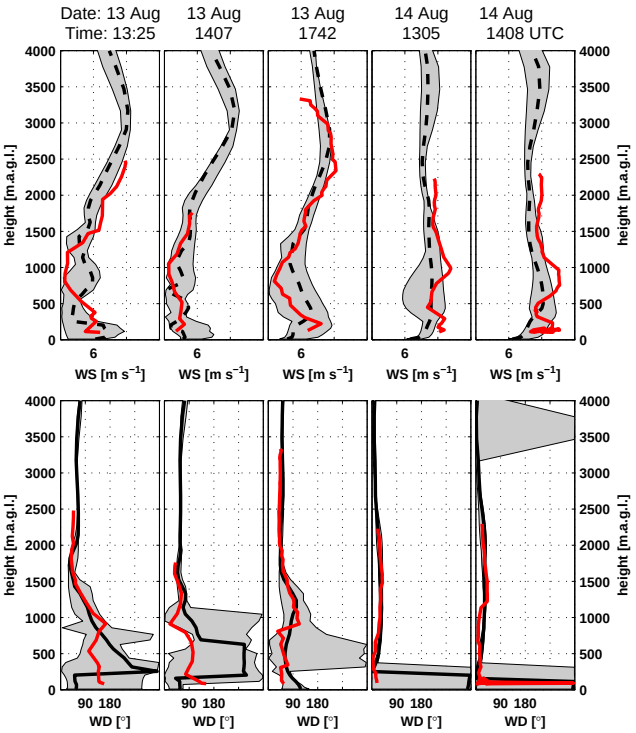

Figure 9. As in Figure 8, but for wind speed [m s^{-1}] and wind direction [°].

August, the winds at lower levels are stronger than on the 13 and the wind direction is north-and northeasterly throughout the probed atmospheric layer. The model simulations suggest that the lower parts of the profiles from 13 August were embedded in the wake of Hofsjökull and the profiles from the 14 August were to the west of the wake. The profiles on 14 August were in fact taken a few kilometres to the east of those on 13 August, which may partly explain these differences.

The large spatial and temporal flow variability taken into consideration, the model reproduces the observed temperature, humidity and wind patterns quite well. The simulated spatial variability in wind is particularly large below 1200 m.a.g.l., as indicated by the grey bars around the simulated profiles, showing the minimum and maximum values within an atmospheric column of size 4x4 km.

5.3. The simulated flow over and around Hofsjökull; sensitivity to surface characteristics

The main results on the sensitivity of the flow over Hofsjökull to the surface characteristics can be deducted from Figure 10. It shows the wind speed across Hofsjökull averaged over the three lowest model levels (9, 35 and 70 m) for the whole simulation period.

The lowest wind speeds are found up- and downstream of the mountain. Over the mountain surface, the low friction simulations have generally higher wind speed than the high friction simulations. Upstream of the ice cap, the difference in wind speed between the simulations is largely negligible. The sensitivitiy to the surface friction is largest over the lee-side slope of the mountain, where the wind speed is consistently lower in the high than in the low friction simulations. The sensitivity in the wind speed to the surface cooling/heating is lower than that to the friction, but also this sensitivity is mainly visible over the lee-side slope. There, a cooler/warmer surface leads to a wind speed increase/decrease of around 1 m s^{-1}. Interestingly, the sensitivity to the heat flux is strongest when the mountain surface is rough. The temporal variability in the above described wind patterns are investigated through the definition of five areas covering approximately 50 km^2, each of which are associated with characteristic locations and flow patterns. The areas are named: 1) Upstream, 2) Upslope, 3) Mountain top, 4) Downslope, and 5)

Downstream. Figure 11 shows timeseries of the near surface wind speed, which is calculated as the average near surface wind within the five areas for the four different simulations. In the Upstream, Upslope and Mountain top areas, the highest wind speeds are found during daytime and the lowest during nighttime. In the Downslope and Downstream areas, there is no clear diurnal signal in the wind speed in any of the simulations. In the low roughness simulations, there is a near consistent shift of the wind maximum from the Mountain top to the Downslope area. In the simulations with high roughness length, on the other hand, the wind speed in the Mountain top and Downslope areas is similar during larger parts of the time (Figure 11 f).

As described in the introduction, variability in flow over mountains can be related to the upstream flow characteristics. Figure 12 shows timeseries of the following simulated upstream flow parameters: the wind speed U, the Brunt Väisälä frequency N and the non-dimensional mountain height Nh/U. Calculating N and U for real atmospheric flow can be a challenging task and several solutions have been proposed. In this study, we use the vertical averaging operator: .

$$\bar{A} = \frac{1}{Z^*} \int_0^{z^*} A \, dz \tag{1}$$

to calculate N and U. The calculations are done separately for each parameter for all model levels between the surface and 1000 m.a.g.l within an atmospheric column located upstream of Hofsjökull (Figure 4). Separate averaging of N and U below mountain top level to calculate Nh/U has also been done by e.g. Chen and Smith (1987) and Georgelin *et al.* (1994) and is discussed in Ólafsson and Bougeault (1997a).

N, the Brunt Väisäla frequency, is defined as:

$$N = \sqrt{\frac{g}{\theta_{avg}} \frac{d\theta}{dz}} \tag{2}$$

where g, θ and z are the acceleration of gravity, the potential temperature and the altitude. In the calculation of Nh/U, we have set h to 1000 m.

The stability N, features a typical diurnal signal; the lowest values of N are found during nighttime and the highest values of N during daytime. The values of Nh/U follow the same temporal pattern. The upstream wind speed U, varies between 8 and 12 m s^{-1}. Only very small differences are found in the upstream flow parameters between the different simulations. The wind speed in the Upstream area is strongly negatively correlated with Nh/U for all four simulations (correlation coefficient of approximately -0.87), indicating the presence of an upstream blocking in the night hours. Such upstream blocking is indeed seen in the simulated horizontal wind field, showing flow stagnation and splitting upstream reaching almost the mountain crest during most of the night (not shown).

Figure 13 shows the near surface wind speed (appr. 9 m.a.g.l.) over Hofsjökull at 1200 UTC on 13 August 2007 for the four different simulations. The flow at this time is found to be typical for the present cases. The wind field patterns are similar to those found through the above investigation of the wind speed in the four characteristic flow areas: the highest near surface wind speeds are located over the lee-side slope of Hofsjökull in the simulations with low surface roughness. Furthermore, there is a slight tendency for the lee-side winds to reach further downslope (3-5 km) in the simulations with an intact ice cap (Smooth glacier and Rough glacier), when compared to the corresponding simulations without the ice cap (Smooth noglacier and Rough noglacier). This trend is more evident in the vertical cross sections in Figure 14. In these cross sections, a feature not seen in the near surface wind field becomes evident: there is a zone of high wind speeds over the downstream slope and downstream of Hofsjökull near the top of the boundary layer in the simulations with a high surface roughness.

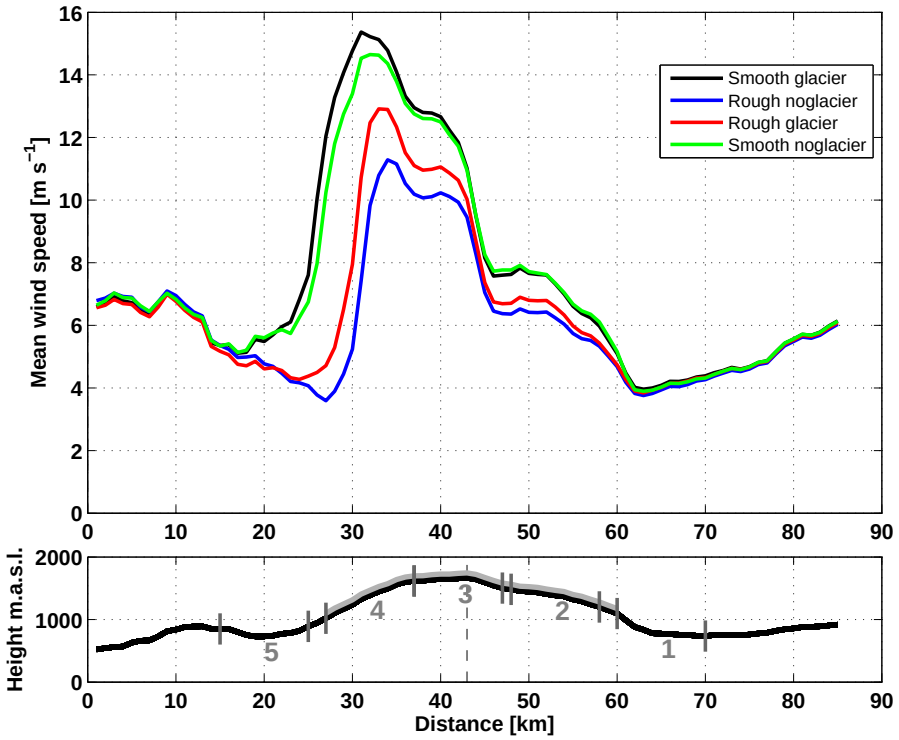

Figure 10. Cross section of mean simulated near surface wind speed [m s^{-1}] (average over the three lowest model levels) on 13 and 14 August, 2007 for the four different WRF simulations. The location of the cross section and areas 1) Upstream, 2) Upslope, 3) Mountain top, 4) Downslope and, 5) Downstream are indicated in this figure's lower panel and in Figure 4. The location of the ice cap is indicated with a solid, grey line in the lower panel.

In the simulations with low surface roughness, there are signs of wave breaking aloft over the leeward slope of Hofsjökull in the form of backwards tilting/overturning isentropes. The waves are not as steep in the high roughness simulations.

5.4. The drag

Figure 15 a) and b) shows the mean sea level pressure (MSLP) in the Upstream and Downslope areas on Hofsjökull. The difference between the upstream and the downslope pressure (Figure 15 c)) can be considered to represent the drag force exerted by the mountain upon the atmosphere. This drag is normalised with the linear drag and presented as a function of Nh/U in Figure 15 d). For the linear drag, we use the 2D estimate as follows:

$$\mathcal{D}_{2D,lin} = \frac{1}{4}\pi\rho_0 NUh^2 \times L_y \qquad (3)$$

Where ρ_0 is set to 1.2 kg m^{-3}, h is set to 1000 m and N and U are calculated as described above. L_y is set to 20000 m, which is the approximate radius of Hofsjökull.

Overall, the upstream pressure appears not to be sensitive to the surface of the mountain. Downslope, there is only small sensitivity of the pressure to the underlying surface. This sensitivity is however not systematic, i.e. the drag is not systematically reduced as the friction is increased.

6. Discussion

The detrimental effect of surface friction on downslope flow is well known and in that aspect the present results are in line with studies such as Richard *et al.* (1989), Georgelin *et al.* (1994), Ólafsson and Bougeault (1997a), and Peng and Thompson (2003). The negative impact of surface heating is also in line with previous research such as Raymond (1972), Smith and Skyllingstad (2011), Valkonen *et al.* (2010), and Doyle *et al.* (2005).

In this study, the two aforementioned effects have been compared systematically for flow over a mesoscale glacier covered Hofsjökull mountain in Iceland for typical

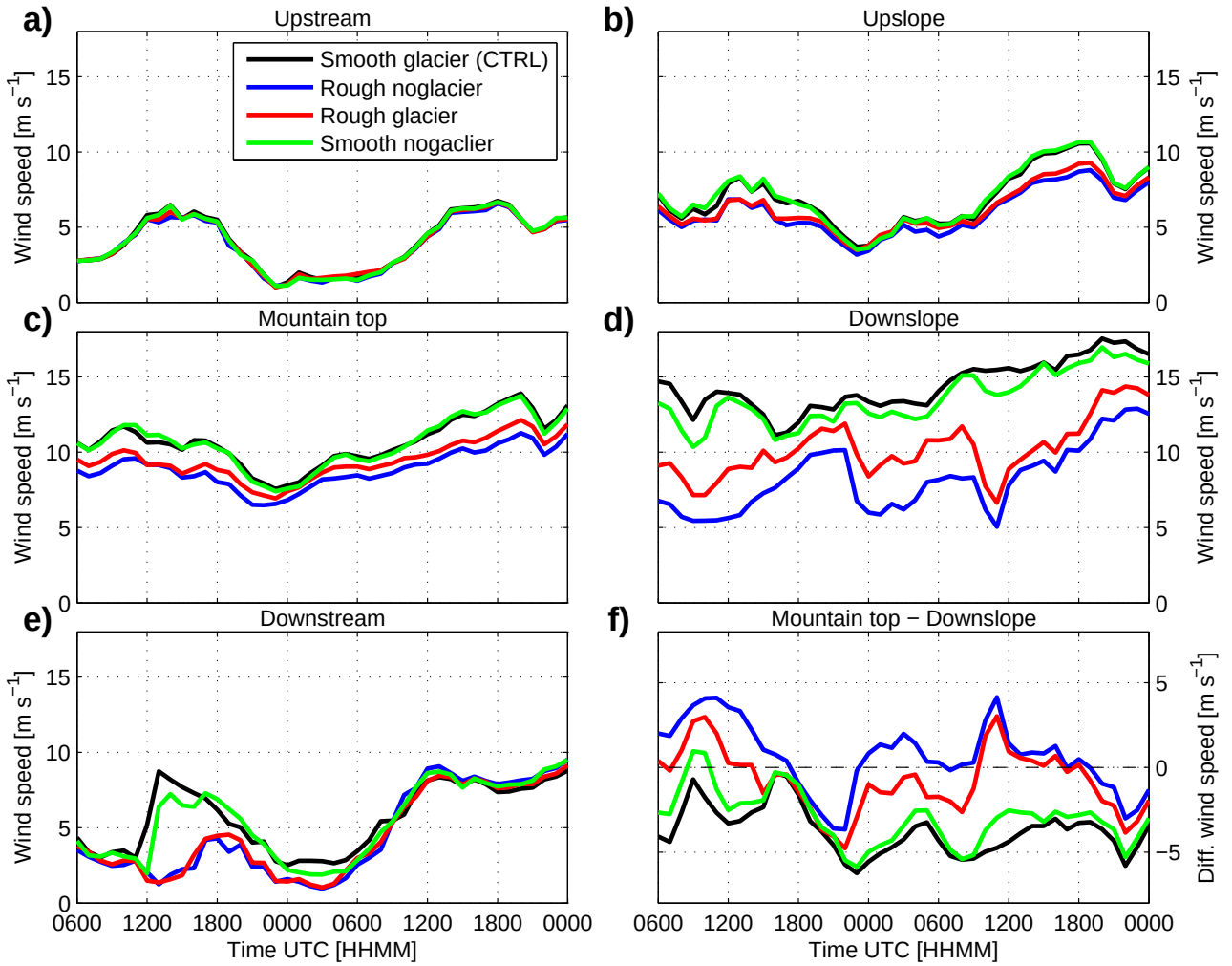

Figure 11. Simulated near surface wind speed [m s^{-1}] (average over the three lowest model levels) on 13 and 14 August, 2007 for five areas on and near Mt. Hofsjökull associated with five characteristic locations and flow patterns: **a)** Upstream, **b)** Upslope, **c)** Mountain top, **d)** Downslope and **e)** Downstream for the four different simulations. The location of the respective areas are indicated in Figure 4. Panel f) shows the difference between the Mountain top and Downslope wind speeds, i.e. the downslope acceleration of the wind.

summertime conditions. Under these conditions, the low surface roughness, and not the presence of a consistently cold mountain surface, is the main contributor to downslope flow acceleration. For larger glaciers, this may not be true; the larger the mountain is, the greater is the impact of the surface heat fluxes on the stratification of the flow and the gravity waves (Doyle *et al.* 2005). The present results show that the surface heating is much more efficient in reducing the downslope wind speed if the surface is rough, than if the surface is smooth. This calls for an explanation. Figure 16 shows the vertical wind and turbulence kinetic energy (TKE) profiles above the Downslope area of Hofsjökull. As expected, the vertical windshear in the lowest ca. 100 m is much greater in the simulations with a rough mountain surface, than in the simulations with a smooth mountain surface. Turbulence due to surface heating counteracts this windshear by bringing constantly high momentum flow down to the surface where it subject to frictional deceleration. Above the smooth surface, the vertical windshear is weaker and the thermals have a smaller impact on the generation of frictional turbulence at the surface. The above indicates that the TKE is increased substantially when surface heating is turned on and the surface is rough, while the corresponding increase of TKE by surface heating is relatively small if the surface is smooth. Figure 16 b) confirms this. The generation of TKE results in a reduction of the momentum of the mean flow and lower wind speed. Consequently, the heating of the surface gives a greater wind reduction if the surface is rough than if the surface is smooth. Upstream, this combined effect of

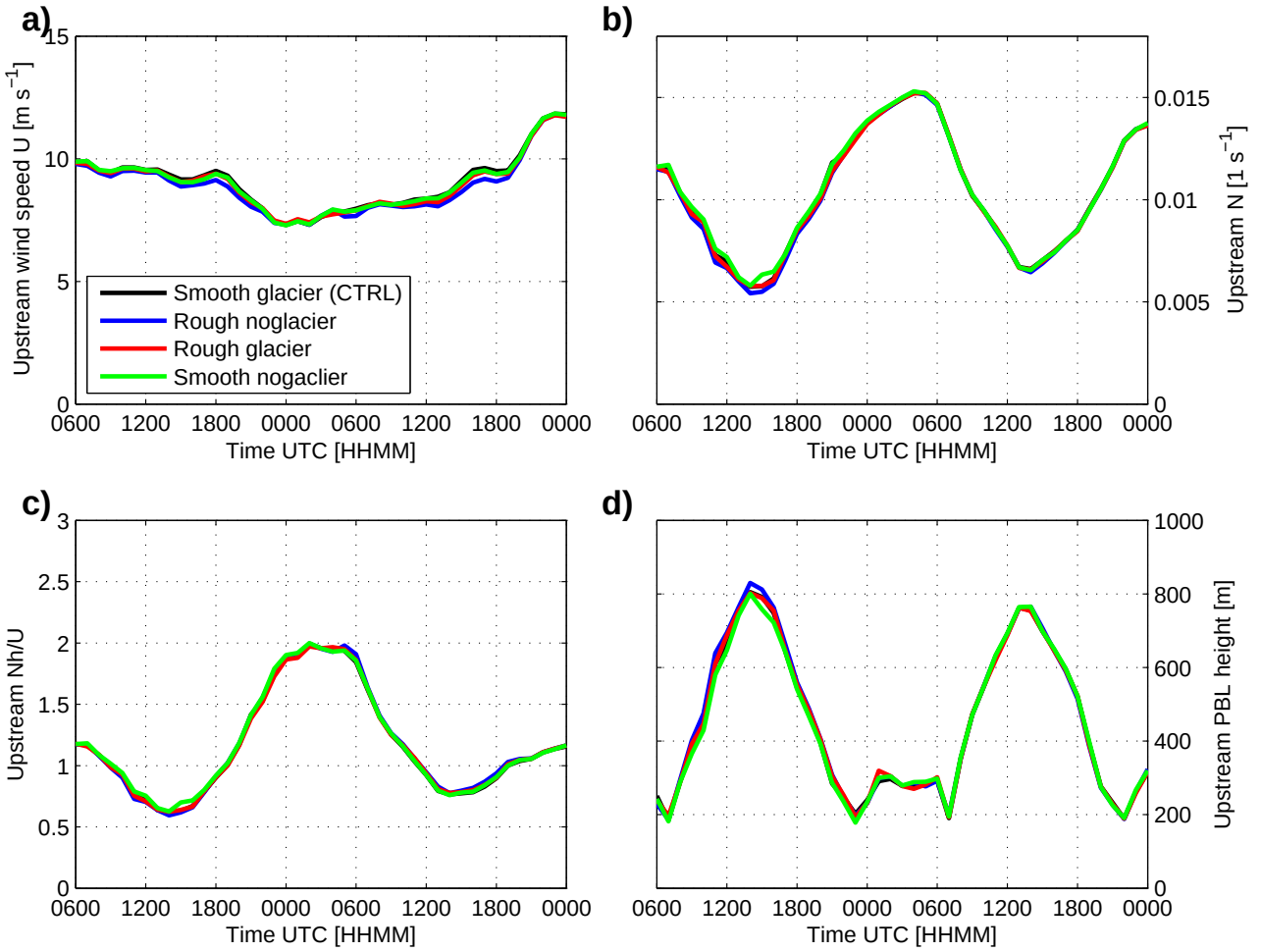

Figure 12. Simulated upstream flow parameters **a)** U, **b)** N and **c)** Nh/U. Each parameter has been calculated separately and averaged over all model levels between the surface and 1000 m.a.g.l within an atmospheric column located upstream of Hofsjökull (Figure 4)

surface roughness and surface heat fluxes are similar, but of a much smaller magnitude. The surface roughness does not only reduce the wind speed over the downslope, but it lifts the low level jet further aloft (Figure 16). This feature agrees with earlier simulations of flow over free-slip surface and rough surface (Peng and Thompson 2003) too and more specifically for different surface roughnesses in Kurbatskii and Kurbatskaya (2011).

In their study of the observations from FLOHOF, Reuder *et al.* (2011) found that the heating of the surface surrounding the Hofsjökull ice cap leads to katabatic winds that reach typically a maximum of 4–6 m s^{-1} at the edge of the glacier. These winds blow away from the glacier in all directions directed towards lower altitude and consequently they contribute to increasing the downslope winds, and reducing the upstream winds. It is difficult to estimate the katabatic contribution to the total flow in our study, but the katabatic winds may be a part of the reason why the surface heating (simulations without the glaciated surface) give consistently a greater deceleration of the wind on the downstream side, than on the upstream side.

As expected, the maximum normalised drag is found at values of Nh/U below 1, while for greater and increasing values of Nh/U, the drag decreases gradually. The impact of friction in the high drag state corresponds with the well established effect of friction on mountain waves (Richard *et al.* 1989) and agrees with the results of Ólafsson and Bougeault (1997a) on drag force. Our data indicates greater drag with increased roughness for high values Nh/U, but the impact is not as great as could have been expected in the view of the results of Ólafsson and Bougeault (1997a). The difference between Ólafsson and Bougeault (1997a) and the

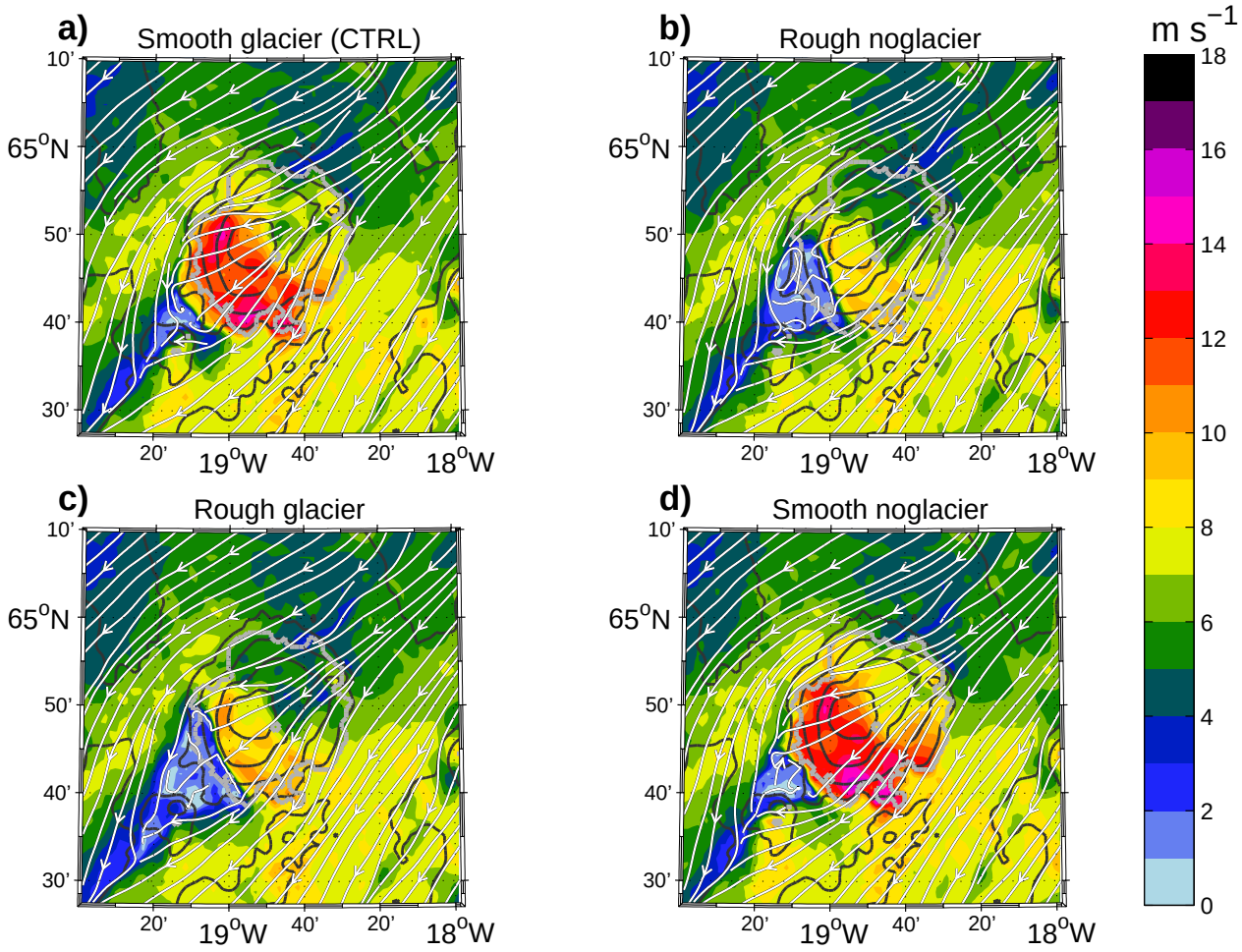

Figure 13. Simulated near surface wind speed (m s^{-1}) (lowest model half-level, 9 m.a.g.l) over Hofsjökull at 1200 UTC on 13.08.2007 from **a)** the simulations: **a)** Smooth glacier (CTRL), **b)** Rough noglacier **c)** Rough glacier **d)** Smooth noglacier. The grey, solid line around Hofsjökull indicates the location of the ice cap. The terrain height is given with contours every 250 m.

present results, may be related to the range of values of the surface roughness or the limited spatial extent of the surface roughness changes in the present study.

7. Summary and conclusions

Recent dynamical downscaling of the flow over Iceland indicates persistent downslope winds over the larger ice caps. In this study, our main goal has been to find the reason for this flow pattern. Previous studies have shown both surface friction and surface heating to have a detrimental effect on mountain waves and downslope accelerated flow. Ice caps are characterised by both a relatively cold and a smooth surface, and hence both effects should potentially be present. Through a series of numerical sensitivity experiments using the WRF model, we have investigated the flow over the meso-scale sized Hofsjökull mountain in central Iceland. The investigations have focused on two real flow cases from the FLOHOF campaign, summer 2007. The results reveal that the wind speed maximum on the downstream side of the mesoscale ice cap is primarily a result of low surface roughness over the ice. The impact on the wind upstream of the mountain top is small in all the experiments. Furthermore, we find that the impact of surface fluxes increases with an increased surface roughness; the enhancement of the downslope winds is larger when going from a warm surface to a cold surface when the surface is rough than when it is smooth. We explain this by refering to the vertical wind profile and different turbulent mixing. The results from the present study are relevant not only for the understanding of factors affecting downslope acceleration of stably stratified flow, but also because the glaciers are observed to reatreat

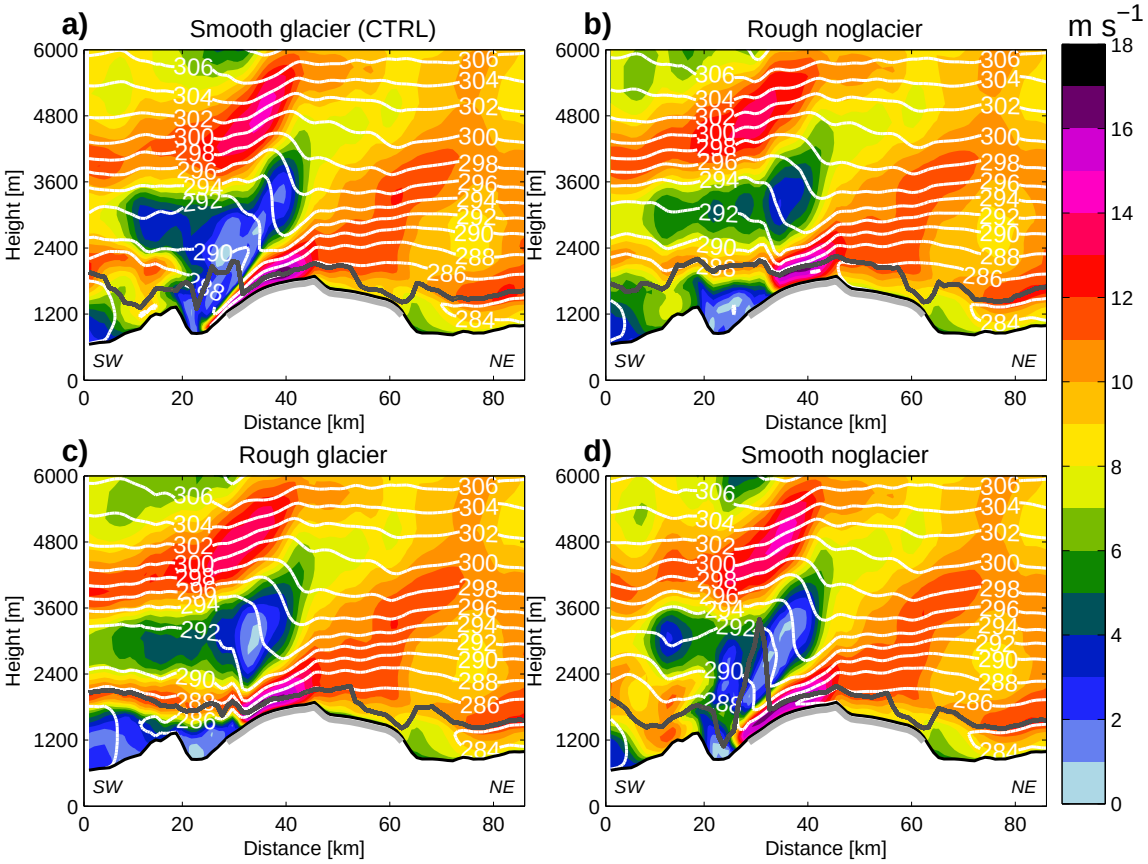

Figure 14. Vertical cross section of simulated wind speed (m s^{-1}) over Hofsjökull at 1200 UTC on 13 August, 2007 from the simulations **a)** Smooth glacier (CTRL) simulation, **b)** Rough noglacier **c)** Rough glacier and **d)** Smooth noglacier. The grey, solid line along the mountain surface indicates the location of the ice cap and thus the area affected by the landuse modifications. The dark grey, solid line is the model diagnosed boundary layer height. The geographical location of the cross section is indicated in Figure 4.

in response to a warming climate. The resulting impacts on the local scale to changes in the ice caps in Iceland can be expected to be seen in e.g. vegetation patterns.

References

Ágústsson H, Ólafsson H. 2007. Simulating a severe windstorm in complex terrain. *Meteorologische Zeitschrift* **16**(1): 111–122.

Ágústsson H, Ólafsson H. 2012. The bimodal downslope windstorms at kvísker. *Meteorology and Atmospheric Physics* **116**: 27–42.

Brinkmann WAR. 1974. Strong Downslope Winds at Boulder, Colorado. *Mon. Wea. Rev.* **102**: 592–602.

Chen F, Dudhia J. 2001. Coupling an Advanced Land Surface-Hydrology Model with the Penn State-NCAR MM5 Modeling System. Part 1. Model Implementation and Sensitivity. *Mon. Wea. Rev.* **129**: 569–585.

Chen WD, Smith RB. 1987. Blocking and deflection of airflow by the alps. *Mon. Wea. Rev.* **115**: 2578–2597.

Doyle JD, Shapiro MA, Jiang Q, Bartels DL. 2005. Large-Amplitude Mountain Wave Breaking over Greeland. *J. Atmos. Sci.* **62**: 3106–3126.

Dudhia J. 1989. Numerical study of convection observed during the winter monsoon experiment using a mesoscale two-dimensional model. *J. Atmos. Sci.* **46**: 3077–3107.

Epifanio CC, Qian T. 2008. Wave-Turbulence Interactions in a Breaking Mountain Wave. *J. Atmos. Sci.* **65**: 3139–3158.

Georgelin M, Richard E, Petitdidier M, Druilhet A. 1994. Impact of Subgrid-Scale Orography Parameterization on the Simulation of Origraphic FLows. *Mon. Wea. Rev.* **122**: 1509–1522.

Gill AE. 1982. Atmosphere-Ocean Dynamics : 662.

Hong S, Dudhia J, Chen S. 2004. A revised approach to ice microphysical processes for the bulk parameterization of clouds and precipitation. *Mon. Weather. Rev* **132**: 103–120.

Janjić ZI. 1994. The step-mountain eta coordinate model: Further development of the convection, viscous sublayer, and turbulent closure schemes **122**(5): 927 – 945.

Janjić ZI. 2001. Nonsingular implementation of the Mellor-Yamada level 2. 5 scheme in the NCEP meso model. Scientific report Office note 437, National Center for Environmental Prediction.

Jiang Q, Doyle JD. 2008. On the Diurnal Variation of Mountain Waves. *J. Atmos. Sci.* **65**: 1360–1377.

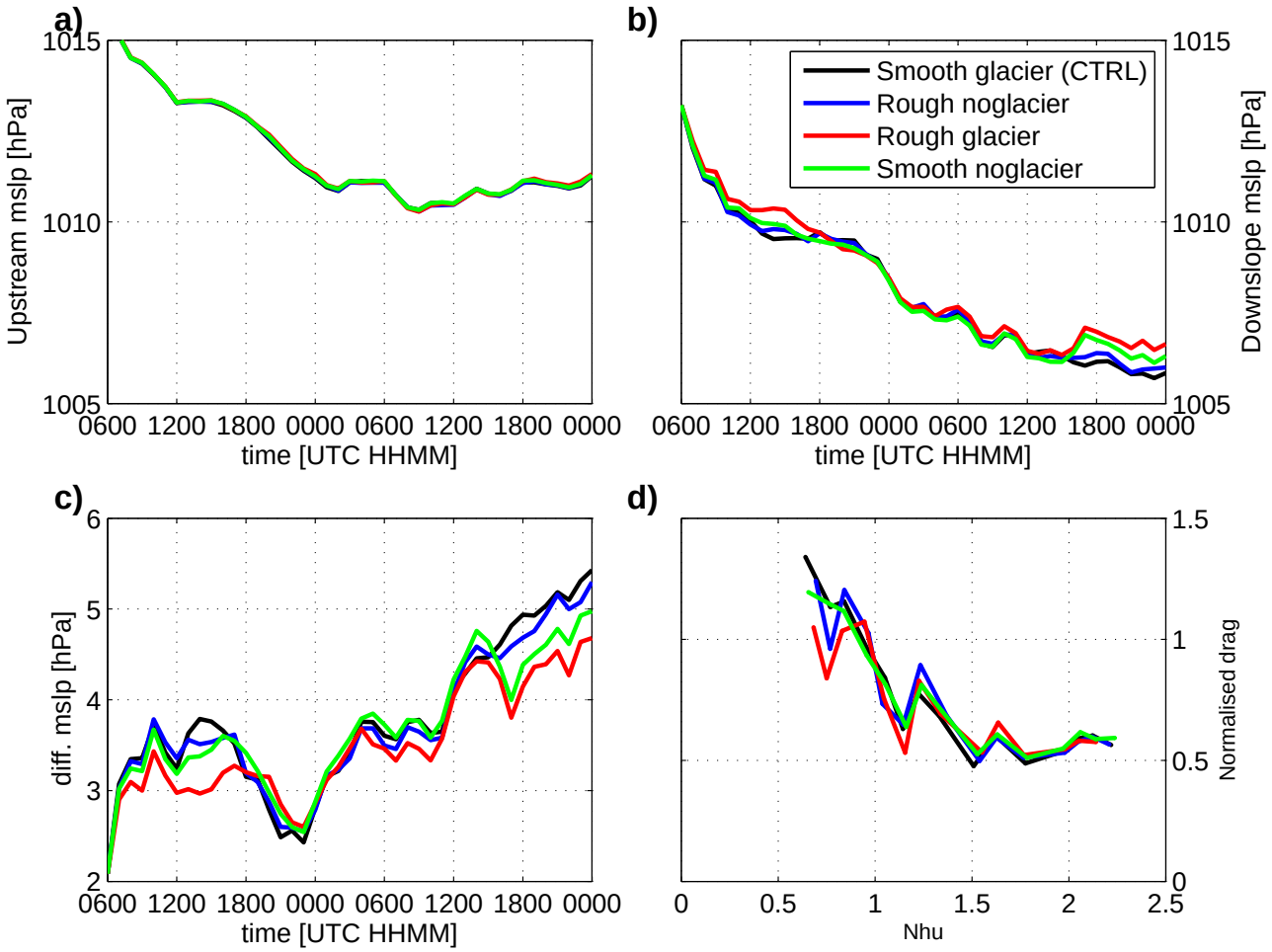

Figure 15. The MSLP averaged over a), the Upstream area and b), the Downslope area. c) shows the difference between the two (a-b) and d) shows the normalised drag as a function of Nh/U

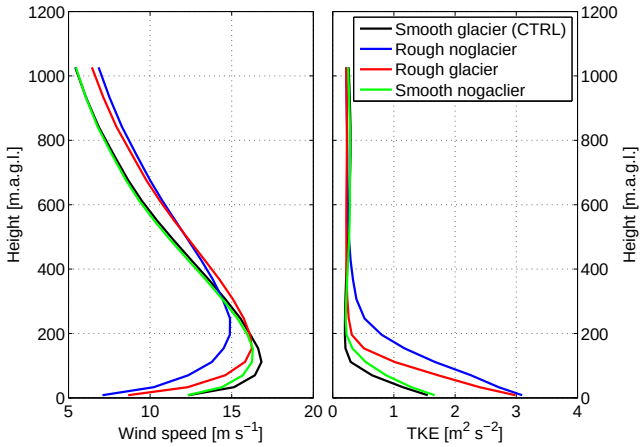

Figure 16. Vertical profiles of a), simulated horizontal wind speed and b), TKE over the Downslope area of Hofsjökull.

Kurbatskii AF, Kurbatskaya LI. 2011. The Wind-Field Structure in a Stably Stratified Atmospheric Boundary Layer over a Rough Surface. *Atmospheric and Oceanic Physics* **47**: 281–289.

Lilly DK. 1972. Wave momentum flux - A GARP problem. *Bull. Amer. Meteor. Soc.* **53**: 17–23.

Mayer S, Hattenberger G, Brisset P, Jonassen MO, Reuder J. 2011. A 'no-flow-sensor' wind estimation algorithm for Unmanned Aerial Systems. *International Journal of Micro Air Vehicles* In press.

Mayer S, Sandvik A, Jonassen MO, Reuder J. 2010. Atmospheric profiling with the UAS SUMO: a new perspective for the evaluation of fine-scale atmospheric models. *Meteorol. Atmos. Phys.* .

Mellor GL, Yamada T. 1982. Development of a turbulence closure model for geophysical fluid problems **20**: 851 – 875.

Mlawer EJ, Taubman SJ, Brown PD, Iacono MJ, Clough SA. 1997. Radiative transfer for inhomogeneous atmospheres: RRTM, a validated correlated-k model for the longwave. *J. Geophys. Res.* **102**: 16 663 – 16 682.

Ólafsson H, Bougeault P. 1997a. The Effect of Rotation and Surface Friction on Orographic Drag. *J. Atmos. Sci.* **54**: 193–210.

Ólafsson H, Bougeault P. 1997b. Why was there no wave breaking in PYREX? *Beitr. Phys. Atmos.* **70**.

Peng MS, Thompson WT. 2003. Some aspects of the effect of surface friction on flows over mountains. *Q. J. R. Meteorol. Soc.* **129**: 2527–2557.

Raymond DJ. 1972. Calculation of Airflow Over an Arbitrary Ridge Including Diabatic Heating and Cooling. *J. Atmos. Sci.* **29**: 837–843.

Reuder J, Ablinger M, Ágústsson H, Brisset P, Brynjólfsson, Garhammer M, Jóhannesson T, Jonassen M, Kühnel R, M L, de Lange T, Lindenberg C, Malardel S, Mayer S, Müller M, Ólafsson H, Rögnvaldsson O, Schäper W, Spengler T, Zängl G, Egger J. 2011. FLOHOF 2007: An overview of the mesoscale meteorological field campaign at Hofsjökull, Central Iceland. *Meteorol. Atmos. Phys.* : DOI: 10.1007/s00 703–010–0118–4.

Reuder J, Brisset P, Jonassen MO, Müller M, Mayer S. 2009. The Small Unmanned Meteorological Observer SUMO: A new tool for atmospheric boundary layer research. *Meteorol. Z.* **18**: 141 – 147.

Richard E, Mascart P, Nickerson EC. 1989. The Role of Surface Friction in Downslope Windstorms. *J. Appl. Meteor.* **28**: 241–251.

Rögnvaldsson O, Ágústsson H, Einarson EM, Ólafsson H, Björnsson H, Sveinsson OGB. 2007. Status report for year one of the RAV project (In Icelandic) Http://thjarkur.orkugardur.is/wordpress/wp-content/uploads/RAVarsskyrsla2007.pdf.

Rögnvaldsson O, Bao JW, Ágústsson H, Ólafsson H. 2011. Downslope windstorm in Iceland âĂŞ WRF/MM5 model comparison. *Atmospheric Chemistry and Physics* **11**: 103–120.

Skamarock WC, Klemp JB, Dudhia J, Gill DO, Barker DM, Duda MG, Huang XY, Wang W, Powers JG. 2008. A description of the Advanced Research WRF Version 3. *NCAR Tech. Note* **TN-475+STR**: 125.

Smith CM, Skyllingstad ED. 2011. Effects of Inversion Height and Surface Heat Flux on Downslope Windstorms. *Mon. Wea. Rev.* **139**: 3750–3764.

Smith RB. 1989. Hydrostatic airflow over mountains. *Advances in Geophysics* **31**: 59–81.

Smith RB, Grønås S. 1993. Stagnation points and bifurcation in 3-D Mountain flow. *Tellus 45A* : 28–43.

Valkonen T, Vihma T, Kirkwood S, Johansson MM. 2010. Fine-scale model simulations of gravity waves generated by Basen nunatak in Antarctica. *Tellus* **62A**: 319–332.

Wahr MJ, Oort AH. 1984. Friction- and Mountain-Torque Estimates from Global Atmospheric Data. *J. Atmos. Sci.* **41**: 190–204.

Paper 4

Improving High-Resolution Numerical Weather Simulations by Assimilating Data from an Unmanned Aerial System

Jonassen, M. O., Ólafsson, H., Ágústsson, H. Rögnvaldsson, Ó. and Reuder, J.
Accepted for publication in Monthly Weather Review, 2012

Improving High Resolution Numerical Weather Simulations by Assimilating Data from an Unmanned Aerial System.

Marius O. Jonassen

*University of Bergen, Bergen, Norway

Haraldur Ólafsson

University of Bergen, Bergen, Norway.

Dpt. of Physics, University of Iceland. Icelandic Meteorological Office, Reykjavik, Iceland.

Hálfdán Ágústsson

Dpt. of Physics, University of Iceland, Reykjavik, Iceland.

Institute for Meteorological Research, Reykjavik, Iceland.

Ólafur Rögnvaldsson

University of Bergen, Bergen, Norway.

Institute for Meteorological Research, Reykjavik, Iceland.

Joachim Reuder

University of Bergen, Bergen, Norway.

Corresponding author address: Marius O. Jonassen, Geophysical institute, University of Bergen, Allegaten 70, 5007 Bergen.

E-mail: marius.jonassen@gfi.uib.no

Abstract

In this study, it is demonstrated how temperature, humidity and wind profile data from the lower troposphere obtained with a light weight Unmanned Aerial System (UAS) can be used to improve high resolution numerical weather simulations by four dimensional data assimilation (FDDA). The combined UAS and FDDA system is applied to two case studies of northeasterly flow situations in Southwest Iceland from the international Moso field campaign on 19 and 20 July, 2009. Both situations were characterised by high diurnal boundary layer temperature variation leading to thermally driven flow, predominantly in the form of sea-breeze circulation along the coast. The data assimilation leads to an improvement in the simulation of the horizontal and vertical extension of the sea-breeze as well as of the local background flow. Erroneously simulated fog over the Reykjanes peninsula on 19 July, that leads to a local temperature underestimation of 8 K, is also corrected by the data assimilation. Sensitivity experiments show that both the assimilation of wind data and temperature and humidity data are important for the assimilation results. UAS represents a novel instrument platform with a large potential within the atmospheric sciences. The presented method of using UAS data for assimilation into high resolution numerical weather simulations is likely to have a wide range of future applications such as wind energy and improvements of targeted weather forecasts for instance for search and rescue missions.

1. Introduction

A numerical weather model's ability to accurately simulate atmospheric dynamical and physical processes depends critically on several factors. These are amongst others the spatial grid resolution and the parameterisation schemes used to represent processes connected to e.g. clouds, radiation, precipitation and turbulence (e.g. Pleim and Xiu 1995; Alapaty et al. 2001; Teixeira et al. 2008). In addition, the quality of the data used to initialise and force the model is essential for the success of a numerical simulation. These data often originate from global atmospheric analyses or forecasts, e.g. from the Global Forecasting System (GFS) or the European Centre for Medium-Range Weather Forecasts (ECMWF) with resolutions typically being 15-50 km in the horizontal and 3-6 hours in time. These atmospheric data are often not accurate enough for high-resolution simulations of local features which may be sensitive to small errors in the large scale flow, as pointed out by e.g. Nance and Durran (1997) in their study of lee waves. The quality of the analysis data depends mainly on two factors. One is the technique used to compile the analysis, i.e., the numerical weather prediction model used to generate the first guess and the statistical methods used to combine the first guess information and the observations. The second factor is the quality and coverage of the observations used to create the analysis (e.g. Langland et al. 1999). Observations can be particularly sparse over areas such as the world's oceans and the Arctic and Antarctic.

To improve numerical weather simulations, the initial and forcing data are often supplemented with additional in-situ or remote sensing observations through a method called nudging, or Four Dimensional Data Assimilation (FDDA) (e.g. Anthes 1974; Stauffer and Seaman 1990, 1994; Stauffer et al. 1991). When applied to observational data, as done in the present study, this assimilation method 'nudges' the modelled atmospheric state towards the observations by introducing an artificial forcing term in the model's governing equations. The forcing term is based on the difference between the modelled and observed atmospheric state. Compared to alternative data assimilation methods, like 3D or 4D var and Kalman-ensemble filter methods, nudging is conceptually simple and computationally inexpensive

(e.g. Stauffer and Seaman 1990; Fast 1995; Reen and Stauffer 2010).

The provision of corresponding data for assimilation and also for model validation, however, poses major technical challenges. This is especially valid for high resolution numerical simulations of the atmospheric boundary layer (ABL), as the operational network of automatic weather stations and radiosondes generally is too sparse and unevenly distributed to accurately describe the temperature, wind and moisture structure with high temporal and spatial resolution (e.g. Otkin et al. 2011). Conventional in-situ instrument platforms like towers and captive balloons and remote sensing technologies as lidars, radars, sodars and satellites have the potential of aiding towards the desired datasets for assimilation and validation. For some applications, like meteorological field campaigns that are targeted towards specific ABL phenomena in remote areas, and which are limited in time and by a small budget, these instrument platforms may, however, be too expensive. They may furthermore be too demanding to operate in the field, e.g. due to the requirement of expert personnel, limited in-field mobility and infrastructural requirements like a continuous demand for electricity. In this context, unmanned aerial systems (UASs) have the potential to become an invaluable tool in ABL research. These systems, consisting mainly of an unmanned aircraft and a ground control station, were for the first time used for atmospheric measurements in the 1970's (Konrad et al. 1970). Following the recent development in micro electrical components, both with respect to avionics as well as instrumentation and sensors for atmospheric measurements, these have now become significantly more viable and feature amongst other things fully autonomous navigation and advanced mission planning tools.

Examples of such systems include M^2AV (Van den Kroonenberg et al. 2008; Martin et al. 2011), the Aerosonde (Curry et al. 2004) and the Small Unmanned Meteorological Observer (SUMO) (Reuder et al. 2009). These light weight UASs represent a novel and very flexible instrument platform which is generally user friendly and cost-efficient to operate. Furthermore, they are able to provide a unique data coverage in both space and time and thereby have the potential to augment and fill the observational gap between the aforementioned

conventional instrument platforms. They are able to provide in-situ data, not reliant on similarity or propagation assumptions, and they are undisturbed by clouds. Data delivery is fast or even instantaneous. Their low infrastructural requirements allow them to be used in otherwise data-sparse regions, such as the polar areas where the mentioned UASs have already been successfully operated.

In this article, we demonstrate a combined UAS and FDDA system, where profile data of temperature, humidity and wind obtained with the UAS SUMO are assimilated into the Weather Research and Forecasting model (WRF) (Skamarock et al. 2008) using the FDDA technique. The system is applied to two case studies of weather situations that took place during the international Moso field campaign on 19 and 20 July, 2009, in Southwest Iceland. The weather situations were characterised by strong diurnal boundary layer temperature variation leading to thermally driven winds, predominantly in the form of sea-breeze circulation along the coast.

Sea-breeze is recognized to have a great influence on the local to meso-scale flow in coastal areas. Knowledge on and predictability of this circulation may play an important role in e.g. local weather forecasting for aviation and transport at sea. Sea-breeze is also found to be of large importance for the formation and movement of thunderstorm complexes (e.g. Pielke 1974) and transport of pollutants (e.g. Warner et al. 1978; Soler et al. 2011). Sea-breeze is a widely studied phenomenon, and reviews are given by e.g. Stull (1988) and Pielke (2002). Very few studies, however, focus on sea-breeze at high latitudes. One such study is that by Grønås and Sandvik (1998) who studied sea-breeze at latitudes higher than 60° north. With a main focus on Norway and Spitsbergen they found through idealised numerical simulations that the sea-breeze is well developed at these latitudes in summertime. Another study of sea-breeze at higher latitudes is that of Gahmberg et al. (2010) who focused on the interaction between sea-breeze and synoptic flow. They found amongst other things the strongest sea-breeze for moderate large-scale flows blowing 45 - 90° anticlockwise from the offshore direction perpendicular to the coast.

Sea-breeze in Iceland is mentioned in the paper of Bromwich et al. (2005), who made a high resolution regional climate simulation of Iceland for 1991 - 2000. They concluded that sea-breeze appears to be an integral part of the summertime weather along most of the coastline. Jónsson (2002) investigated wind speed and wind directions recorded by automatic weather stations throughout Iceland for the month of June and found observational evidence of the climatological presence of sea-breeze in Iceland.

Sea-breeze circulations are finely balanced systems and typically a challenge for operational numerical weather prediction systems to accurately reproduce in both time and space (e.g. Fuentes et al. 2005). How the numerical simulations reproduce the surface and boundary layer flow and temperature including the sea-breeze circulation, with and without the assimilation of all and parts of the UAS temperature, humidity and wind data, is the main topic of this study. In addition, several sensitivity experiments on different nudging parameters are carried out.

2. Observations

The Moso field campaign

The international Moso field campaign was conducted in Southwest Iceland in the period from 9 to 20 July, 2009. The campaign, which name is short for "Mosfellsbær", a small settlement outside Reykjavik, was dedicated to the study of thermally driven and orographically modified meso-scale flow. In the first part of the campaign, the formation of weak gravity waves was studied using the UAS SUMO and a network of automatic weather stations in the vicinity of Reykjavik. Using the same observational tools, two weather situations dominated by sea-breeze circulation along the southwest coast of Iceland on 19 and 20 July were observed in a second part the campaign. The present study focuses on the results from this second part, while the first part will be the subject of a future study.

The study region can be divided into an eastern and a western area as naturally separated

by the Reykjanes mountain range (ca. 350-800 m.a.s.l.) (Figure 1). The eastern area is the area of main interest and the UAS soundings were made at Eyrarbakki. The central parts of the eastern region mostly consist of relatively flat, farmed land, while the outskirts of the area are dominated by more complex topography, most markedly by the Eyjafjallajökull (1666 m.a.s.l.) and Myrdalsjökull (1450 m.a.s.l.) massif in the south east (north of AWSs Steinar and Hvammur) and the Reykjanes mountain range in the west.

AWS data from the western area are included as complementary information to investigate the spatial extension of the impact of the data assimilation.

Near surface observations, automatic weather stations (AWSs)

In Southwest Iceland, there is a rather dense network of AWSs, run mainly by the Icelandic Meteorological Office (Veðurstofa Íslands) and the Icelandic Road Administration (ICERA/Vegagerðin). The AWS data in this study are based on 10 minutes averages and obtained with a temporal resolution of 1 hour. Temperature and relative humidity are measured at 2 m above the ground level and the wind is observed at 10 m or at the top of a 6 m high mast raised approximately 1 m above its immediate surroundings (Skalholt). Most stations are located below 50 m.a.s.l.

Smal/l Unmanned Meteorological Observer, SUMO

The atmospheric profiles used in this study were made with the UAS SUMO (Reuder et al. 2009) that has been developed in a collaboration between the Geophysical institute, University of Bergen and Martin Müller engineering, Germany. SUMO consists of three main parts: a small model aircraft, a ground control station and a remote control. It is equipped with an autopilot system that is developed under the open-source Paparazzi project supervised by the French school for civil aviation (Ecole Nationale de l'Aviation Civile, ENAC) (Brisset et al. 2006). In its current version, the SUMO airframe is the commercially

153 available FunJet construction kit from Multiplex. With a weight of only 0.58 kg, wingspan
154 of 0.8 m and length of 0.75 m, the airframe is relatively small and light weight and thus ideal
155 for use in e.g. remote areas and complex terrain with a minimum of infrastructural facilities.
156 The system is very quickly deployed in the field and is ready for operation within 10 - 15
157 minutes from arriving at the measurement site. The aircraft is electrically powered by lithium
158 polymer batteries giving a typical flight endurance of 20 to 45 minutes, depending mainly
159 on the flight pattern, wind speed and the atmospheric temperature. Within this time-frame,
160 a maximum altitude of around 5 km can be reached. During the Moso field campaign, the
161 system was equipped with sensors for the measurement of temperature, relative humidity and
162 pressure. The manufacturer (Sensirion) of the combined temperature and humidity sensor
163 (SHT 75) gives an absolute accuracy of respectively 0.3 C° and 1.8 %. Wind direction and
164 wind speed is estimated indirectly by a method relying on the on-board GPS data and an
165 assumption of constant true-airspeed and constant pitch angle. The method is described
166 in more detail by Mayer et al. (2012). The flight pattern used for atmospheric profiling
167 resembles a helix that corresponds to an atmospheric column with a radius of 50-100 m.
168 The aircraft has relatively high ascent and descent speeds (5-8 m/s) and due to a relatively
169 slow sensor response, the temperature and humidity data have been corrected using a method
170 outlined in Jonassen (2008).

171 SUMO was used for the first time during the FLOHOF field campaign (Reuder et al.
172 2011) in Central Iceland, 2007. Data from SUMO have subsequently been used to validate
173 WRF boundary layer schemes for case studies from FLOHOF (Mayer et al. 2010).

174 The SUMO measurements have been verified against and shown to have a quality similar
175 to that of well established sounding systems like radiosondes (Mayer et al. 2012; Jonassen
176 2008) and the authors are therefore confident in using these data for assimilation and model
177 validation.

178 During take-off and landing, the SUMO is operated manually and wind data from the
179 lowest tens of metres above the ground level are therefore not included in the data assim-

ilation. Each of the profiles is averaged in 20 m height intervals. The descent data are used for the assimilation since these are found to have the better quality as the descent rate is slightly lower than the ascent rate. The lower descent rate gives the temperature and humidity sensor better time to adjust to its ambient surroundings, thus reducing the effect of slow sensor response while also allowing for a more accurate determination of the wind vector.

An overview over the SUMO flights on 19 and 20 July is given in Table 1.

3. The numerical simulations

The numerical simulations are performed using the Advanced Research Weather Research and Forecasting model (WRF ARW) Version 3.2.1 (Skamarock et al. 2008). The modelling system is fully compressible and is in this study run in non-hydrostatic mode using 3 two-way nested domains with a horizontal resolution of 9, 3 and 1 km. The outermost domain (855 x 810 km) covers Iceland and the surrounding waters (50-100 km offshore) while the innermost domain (250 x 190 km) covers Southwest Iceland. 51 vertical terrain following model levels are used with an increased resolution towards the ground. The lowest half level is at approximately 9 m.a.g.l.

Two sets of 24 hour simulations are performed, the first starting at 0000 UTC on 19 July and the second at 0000 UTC on 20 July, 2009. The first 6 hours of each simulation are considered as spin-up. The RRTM (Mlawer et al. 1997) scheme is used for long wave radiation parameterisation, the Dudhia scheme (Dudhia 1989) for short wave radiation, and the Unified NCEP/NCAR/AFWA Noah land-surface model (Chen and Dudhia 2001) with soil temperature and moisture in four layers for surface physics. Furthermore, the Yonsei University Scheme (Hong et al. 2006), a non-local-k theory, first order scheme with an explicit entrainment layer, is used for the parameterisation of boundary layer physics.

Operational analysis from the European Centre for Medium-Range Weather Forecasts

(ECMWF) at 91 model levels and 0.125 degrees horizontal resolution is used to initialise and force the model at its boundaries every 6 hour.

The extent of the ever reatreating edges of the ice caps in Iceland is too large in the standard 24 categories USGS landuse dataset compared to reality. An updated version of the 24 categories USGS landuse dataset with more realistic ice cap extents provided by the Institute for Meteorological Research (Reiknistofa í Veðurfræði/Belgingur) is therefore used in the simulations of this study (Rögnvaldsson et al. 2007).

Four-dimensional data assimilation, FDDA

The four-dimensional data assimilation (FDDA) technique has been described and employed in several studies (e.g. Anthes 1974; Stauffer and Seaman 1990, 1994; Schroeder et al. 2006). Various datasets from a range of atmospheric measurement platforms have been assimilated using FDDA, both for local and regional hindcasting, nowcasting and forecasting applications. However, to the knowledge of the authors, data from UASs have never before been used for these purposes.

There are two main types of nudging available in the WRF FDDA system (Liu et al. 2005). One is the analysis nudging where the model state is nudged towards a gridded analysis field, which is often used at larger scales for coarse grid resolutions. The second is the observation nudging, which is used in this study. In observation nudging, each observation is used to nudge the model within a certain horizontal radius surrounding its location and within a given time window. The nudging is controlled by the nudging term, being proportional to the difference between the observed and simulated atmospheric state. The nudging is reduced as the distance in time and space from the observation to the model grid points increases. The parameters being nudged are the horizontal wind components u and v, the specific humidity and the temperature.

The nudging's influence in time is limited to 40 minutes before and after each observation, with the strength of the nudging being ramped down towards the beginning and end of each

time interval.

The strength of the nudging is controlled through the nudging coefficients (G). The horizontal radius of influence (R) determines the size of the area that is directly affected by the nudging. Studies have shown that the values of G and R can be important for the data assimilation results (e.g. Xu et al. 2002). In this study, several FDDA sensitivity experiments are carried out and validated against AWS observations with the aim to find the optimal combination of these two parameters. The values tested for G are the default $6 \cdot 10^{-4} \mathrm{s}^{-1}$ in addition to $3 \cdot 10^{-4} \mathrm{s}^{-1}$ and $12 \cdot 10^{-4} \mathrm{s}^{-1}$. The parameter R is given the value 100 km, which covers approximately the innermost domain, and thus the area of main interest, as well as 50 and 150 km. In each of the simulations, the same values for G and R are used for all the nudged parameters and nested domains. In these experiments, all 17 UAS soundings from Case 1 (19 July) and all 11 UAS soundings from Case 2 (20 July) are used for assimilation. Both the mass fields (temperature and humidity) and the horizontal wind fields are assimilated.

Table 2 gives an overview over the values of R and G used for the corresponding FDDA sensitivity experiments.

A third factor, that influences the nudging, is the weighting function used to apply the nudging. Changing this is not as straight forward as changing the R and G parameters and is therefore left to a future study.

The results from the FDDA sensitivity experiments with different values of R and G are presented in the first part of the results section in this article. The best combination of R and G is defined as the one giving the best validation against AWS data. In the second part of the results section, a CTRL setup using no data assimilation is compared against four different FDDA setups using the best combination of R and G. In the FDDA-all setup, all UAS soundings are assimilated. In the FDDA-nomass and FDDA-nowind setups, the mass fields and wind fields are respectively left out of the assimilation. These latter experiments are performed to evaluate the relative importance of assimilating the wind and

mass parameters for the case studies. In the FDDA-single setup, both the mass and the wind fields are assimilated, but only the first sounding in each case is used. This latter experiment is included to evaluate how long lasting the impact of assimilating a single profile is and can be considered a dynamical initialisation.

No observations from the AWSs are used for assimilation in any of the FDDA simulations.

4. Results

The near-surface flow

During 19 and 20 July, 2009, Iceland was under the influence of a northeasterly synoptic flow, set up by a low pressure system over the British isles to the south-east of Iceland and a high pressure ridge over Greenland to the northwest (Figure 2). At the observation site of Eyrarbakki, the skies were dominated by a layer of stratocumulus clouds that increased in thickness and horizontal extension during the course of both these days.

Figure 3 gives a more detailed overview of the flow over Iceland. The simulated flow compares reasonably well against AWS observations spread throughout Iceland and it can be seen that the general flow in Case 2 (20 July) is somewhat stronger than in Case 1 (19 July).

Determining the optimal combination of the radius of influence (R) and the nudging coefficient (G)

As outlined in Section 3, an effort is made to determine the best combination of the R and G parameters in the FDDA setup. Figure 4 shows root mean square and mean errors (RMSE and bias) between the available AWS data and the CTRL and FDDA experiments using different values of R and G. A clear trend towards an improvement in both the temperature and wind is seen for both Case 1 and Case 2 when comparing the error statistics of the

CTRL experiment to the FDDA experiments. For the temperature in Case 1, the RMSE lies in the range 1.5 to 1.7 K for the FDDA simulations and it has a value of 2.1 K for the CTRL simulation. For Case 2, the temperature RMSE is 1.6 K for all the FDDA simulations and 1.9 K for the CTRL simulation.

For the wind speed and wind direction error statistics, the vector wind difference (VWD) is used. VWD is defined as follows:

$$VWD = [(u_o - u)^2 + (v_o - v)^2]^{1/2} \tag{1}$$

Where (u_0,v_0) and (u,v) respectively are the observed and simulated horizontal wind components. The RMSE of the VWD is in Case 1 reduced from 3.7 m/s in the CTRL simulation to 3.3-3.4 m/s in the FDDA simulations. Similarly, the RMSE of the VWD is reduced from 5.0 m/s to 4.6-4.7 m/s in Case 2.

The statistics for the specific humidity, on the other hand, give more variable results with no such consistent improvement.

Overall, there are only marginal differences in the error statistics between the different FDDA experiments and an investigation of the horizontal fields of temperature, humidity and wind confirms this impression (not shown). The default G of $6 \cdot 10^{-4}\mathrm{s}^{-1}$ and a moderate R of 100 km are therefore used in the rest of this study. The R of 100 km covers approximately domain 3, which is the area of interest in this study.

General results

In both the studied cases, sea-breeze circulation dominated the atmospheric flow characteristics and surface fields of temperature and humidity. Thus, in the following evaluation of the numerical simulations, special attention is paid to how the model manages to capture the sea-breezes' onset, maximum horizontal extension and final decay with and without the UAS data assimilated. The model results are verified against available AWS data using the

sea-breeze front as the main diagnostic. The inland progression of the sea-breeze is marked by its front, which might be viewed upon as a meso-scale cold front. The passage of this front typically encompasses a drop in surface temperature in the order of several K, an increase in humidity and a turn in wind direction.

Figures 5, 6 and 7 show the simulated and observed wind speed and wind direction, temperature and specific humidity at selected AWSs in Southwest Iceland on 19 (Case 1) and 20 July (Case 2), 2009.

In the following, the results from each of the two cases are described separately. Case 2 is described in less detail than Case 1 and a main emphasis in the description of Case 2 is put on where the results from the two cases differ the most.

1) Case 1, 19 July

On 19 July, the first signs of sea-breeze are seen at Hella. The onset of the sea-breeze, which takes place at 1000 UTC, can be detected by an abrupt halt in the increase of temperature (Figure 6). This is associated with the winds turning to the southeast (Figure 5). The halt in the temperature increase is captured by the model, but it takes place 2-3 hours earlier. The onshore flow at Hella is visible in the 1200 UTC near-surface wind field (Figure 3). The largest difference between the WRF simulation using only one UAS profile (FDDA-single) and the simulation using all 17 profiles (FDDA-all) at Hella is found in the temperature from 1800 UTC to around 2100 UTC. Between those hours, the temperature is underestimated by 2-3 K in the FDDA-single simulation and lies within 1 K in the FDDA-all simulation. The temperature at Hella in the simulation using all UAS profiles, but no wind information (FDDA-all-nowind) lies much closer to the FDDA-all than does the FDDA-all-nomass at Hella throughout the simulation.

The sea-breeze is stronger and penetrates further inland in the FDDA-all simulation than in the CTRL simulation (Figure 8). There is also a local enhancement of the synoptic-scale flow, opposing the sea-breeze in the FDDA-all simulation.

The observed maximum inland penetration of the sea-breeze on 19 July takes place around 1600 UTC. It then touches upon Kalfholl, as marked by an observed intermittent shift from northerly to southerly flow and a short lived increase in humidity at this station. The increased humidity follows closely the observed increase in the FDDA simulations, except in the FDDA-all-nomass simulation which, similarly to CTRL, lacks such an increase. Thus, the horizontal extension of the sea-breeze is longer in the FDDA simulations (except FDDA-all-nomass) than in the CTRL simulaton, and the validity of the longer inland sea-breeze penetration is confirmed by observations, at least for the area represented by Kalfholl.

As for virtually all AWSs, there is a nearly consistent temperature underestimation in the CTRL simulation at Kalfholl, but at this station, it is still significant (3-4 K in Case 1) even after assimilating all UAS profiles using both the mass and wind fields.

At Eyrarbakki, the UAS operation site, the sea-breeze starts between 1200 and 1300 UTC, which is marked by a drop in the observed temperature and a shift from northeasterly to southwesterly winds. The FDDA-all simulation corrects for a temperature underestimation that is seen in the CTRL simulation at Eyrarbakki from 1200 UTC until around 2000 UTC, when the bias in the CTRL simulation reaches 2-3 K. The FDDA-single simulation temperature gradually degrades from a near perfect match with the observation at Eyrarbakki at 1200 UTC to a similar value as in the CTRL simulation at around 1900 UTC.

At Hellisheidi, there are no observed signs of sea-breeze at any time of the day. This absence of sea-breeze is most likely due to the station's elevated location (360 m.a.s.l.). With the exception of the morning hours (before 1200 UTC), 1700 UTC and towards midnight, the temperature is underestimated by some 2-3 K in the CTRL simulation. In the FDDA-all simulation, on the other hand, the temperature is reproduced very well with observation-model differences of the order of 0-1 K. In the FDDA-single simulation, the temperature bias lies somewhere between the CTRL and FDDA-all simulation (1-2 K) from 1200 UTC and onwards for most of the day. After 1700 UTC, the FDDA-all-nomass simulation performs better than the CTRL simulation with respect to 2 m temperature. The underestimated

temperature in the CTRL simulation can at least in part be related to a shift from the observed northeasterly to northwesterly flow in the CTRL simulation between 1600 and 1800 UTC.

Further inland, at Skalholt (approximately 40 km from the coast), there are also no observed signs of sea-breeze. Similar to Kalfholl, the temperature is significantly underestimated in all the simulations, but not as much in the FDDA-all-nowind as in the FDDA-all-nomass and CTRL simulations. As at Kalfholl, the improvement in the FDDA-single simulation temperature is relatively short lived and is gone after approximately 6 hours.

The simulated wind speed at Skalholt is very low (less than 2.5 m/s) at 1600 UTC and it has a southerly component, coinciding with the sea-breeze direction. The simulated humidity, however, does not show any increase for any of the simulations at this location (not shown), which would have been expected if the sea-breeze had reached it.

The largest changes in temperature from the CTRL to the FDDA simulations are found in Area West, where the CTRL simulation temperatures are largely underestimated in the area around Reykjavik and over parts of the Reykjanes peninsula. This bias is connected to two interdependent phenomena. A shallow (50-100 m) fog resides from early morning hours (0600 UTC) to late evening (2100 UTC) along the Reykjanes peninsula to the southwest of Reykjavik in the CTRL simulation (e.g. Figure 8). In the FDDA simulations, this fog disappears before 1400 UTC. In the CTRL simulation, there is an onshore flow from the aforementioned fog, advecting cold and moist air into the region. This is evident in the form of low temperatures and relatively high values of humidity at the stations in the area in the CTRL simulation (e.g. Reykjavik and Grindavik, Figure 7). In the observations and also mostly correctly in the FDDA simulations, the flow to the north and west of Reykjavik is from the north (Figure 8). Both the assimilation of only the UAS wind profiles (FDDA-all-nomass) and the assimilation of only the UAS temperature and humidity profiles (FDDA-all-nowind) aid in removing this fog, with the effect of the latter being larger.

2) Case 2, 20 July

On 20 July, the sea-breeze sets on later than in Case 1 and the first signs of a sea-breeze are again found at Hella, taking place between 1200 and 1300 UTC. Except for the CTRL and FDDA-all-nomass simulations, the model times the correspondent change to southerly wind quite accurately, while the drop in temperature lags some 1-2 hours behind what is observed in all the simulations.

In contrast to Case 1, the sea-breeze in Case 2 penetrates further inland in the CTRL than in the FDDA-all simulation. A sea-breeze is never observed at Kalfholl. In the CTRL, FDDA-all-nowind and FDDA-single simulations, however, there is an onset of sea-breeze at Kalfholl at around 1600 UTC and it lasts until at least 2200 UTC. The remaining FDDA simulations correctly contain no sea-breeze between 1600 UTC and 1800 UTC at Kalfholl, but in these simulations the sea-breeze erroneously reaches the station at around 2000 UTC. The presence of the sea-breeze is evident by the increase in humidity at Kalfoll at respectively 1500-1600 UTC in CTRL, FDDA-all-nowind and FDDA-single and 1900-2000 UTC in FDDA-all and FDDA-all-nomass.

At Eyrarbakki, the sea-breeze is only observed for a short period of time around 2000 UTC. In all the simulations, on the other hand, there is an onset of sea-breeze at Eyrarbakki at 1500 UTC. This is marked by a sharp drop in the simulated near surface temperature in the CTRL, FDDA-all-nomass and FDDA-single simulations, whereas in the FDDA-all and FDDA-all-nowind simulations, the temperature keeps closer to the observed one with a discrepancy of around 2 K.

The FDDA-all-nowind and FDDA-single simulations erroneously contain sea-breeze at Hellisheidi between 1600 and 2200 UTC and so do also the rest of the simulations between 2000 and 2200 UTC.

In contrast to the results of Case 1, there is seemingly no, or only very little, improvement with respect to temperature in the FDDA-single simulation for any of the stations for Case 2. While the simulated sea-breeze did not reach Skalholt in Case 1, the CTRL and FDDA-

single simulations of Case 2 do contain sea-breeze at Skalholt, setting on at 1800 UTC and lasting until at least 2200 UTC, which is identified in terms of both a southerly wind and a lowered temperature at this location. The remaining FDDA simulations, improve on this situation and they do not contain sea-breeze at Skalholt before 2200 UTC, at which they show an erroneous southerly wind direction. As in Case 1, relatively large underestimations of temperature are found at Kalfholl and Skalholt.

3) Error statistics

The root mean square error (RMSE) and mean bias statistics of the simulated and observed near surface temperature, specific humidity and wind (Figures 10 and 11), largely support the impression gained by the above subjective analysis of the WRF simulations against the AWS observations. A main effect of assimilating the UAS data is the reduction of a nearly consistent model temperature underestimation. The largest contribution in mitigating this bias comes from the assimilation of the UAS temperature and humidity data. The error reduction is largest in the FDDA-all simulations, where the average RMSE between the modelled and observed (AWS) 2 m temperature in Case 1 is reduced from 2.1 to 1.5 K and the corresponding averaged biases from 1.5 to 0.7 K. In Case 2, the reduction is somewhat smaller, with the average RMSE being reduced from 1.9 to 1.6 K and average bias from 0.4 to 0 K.

The effect of only assimilating the wind data (FDDA-all-nomass) is least among the FDDA simulations in this regard, but still positive with an average RMSE of 1.9 K and average bias of 1.3 K for Case 1 and an average RMSE of 1.8 K and average bias of 0.3 K for Case 2.

In Case 1, the RMSE reduction from the FDDA-single simulation lies between the CTRL and FDDA-all simulations with an average RMSE of 1.7 K and average bias of 1.1 K. It should, however, be noted that the observation-model difference for the FDDA-single simulation increases with time, as shown above, starting at differences similar to the FDDA-

all simulation and slowly approaching the CTRL simulation in accuracy and the two are very similar after 6-7 hours at most stations. In Case 2, there is no such consistent improvement in the FDDA-single simulation, and for some AWSs the error statistics is the same as or even worse than for the CTRL simulation. It can also be seen in the previously presented timeseries from the selected AWSs that the improvement is very short lived in Case 2 when compared to Case 1 in the FDDA-single simulations.

For specific humidity, there is no consistent improvement when using FDDA. Nevertheless, for individual stations like Reykjavik, there is still an improvement in Case 1 which is caused by the false presence of fog along the nearby coast in the CTRL simulation, as commented on earlier.

The average of the RMSE VWD in Case 1 is reduced from 3.7 m/s in the CTRL simulation to 3.4 m/s in the FDDA-all simulation. The main contribution comes from the assimilation of the wind as the average VWD RMSE assimilating only the wind is 3.5 m/s, whereas when assimilating only the mass parameters it is 3.6 m/s. The largest improvements in VWD among the stations when using FDDA in Case 1 is found at the AWSs of Arnes and Mork. This improvement is caused by a more accurate description (higher wind speeds) of the local component of the northeasterly synoptic flow, as evident in the horizontal 10 m wind field (Figure 8). Also in Case 2, there is an improvement in the VWD statistics when assimilating the UAS wind data. The average RMSE of the VWD is reduced from 5.0 (CTRL) to 4.6 m/s (FDDA-all).

The flow aloft

In the study of the flow aloft, we focus mainly on the location of Eyrarbakki, where the UAS soundings were made. A main emphasis is put on the description of the vertical development of the sea-breeze circulation and how this is captured by the model, with and without all and only parts of the UAS data assimilated. As for the surface flow, the flow aloft in Case 1 and Case 2 is described separately and a main emphasis in the description of

Case 2 is put on where the two cases differ the most.

4) Case 1, 19 July

Figure 12 and Figure 13 show timeseries of observed and simulated atmospheric profiles of temperature, specific humidity, wind speed and wind direction on 19 and 20 July. The first UAS profile (1238 UTC, 19 July) was measured just after the onset of the sea-breeze at Eyrarbakki. The sea-breeze is identifiable in the first four UAS profiles as a layer of low temperatures and relatively high humidity below approximately 250 m.a.g.l. In this shallow layer, winds are from the sea contrasting the northeasterly synoptic flow further aloft. Approximately at the top of this layer, the on- and offshore flows meet and there is a distinct wind speed minimum. Using the criteria of low wind speed, a turn in wind direction, an increase in temperature and decrease in humidity, the highest vertical extension of the sea-breeze of 250-300 m.a.g.l. is reached sometime between 1400 UTC and 1600 UTC. At 1900 UTC, there are no longer any signs of sea-breeze in neither the UAS profiles nor in the AWS observations.

The simulated temperature, humidity and wind profiles in the FDDA-all simulations are, not surprisingly, considerably closer to the observed data from the UAS and should not be used for direct comparison with the other simulations. The FDDA-single profiles are not discernable from the FDDA-all profiles at 1238 UTC.

The temperatures in what may be interpreted as the boundary layer (below an inversion at 1-1.2 km) are underestimated in the CTRL simulation by 2-3 K compared to the three first UAS profiles (1238, 1358 and 1604 UTC). The specific humidity, however, is well reproduced by the model in these first three profiles, while there are larger discrepancies in the two last profiles (1743 and 1914 UTC).

The temperature underestimations of the lower troposphere are similar in magnitude to the average underestimation in the simulations of temperature at the AWSs. These temperature and humidity differences are reflected in the RMSE and BIAS values averaged

over all profiles throughout the day (Figure 14).

The sea-breeze layer is not evident in the two first profiles (1238 and 1358 UTC) of temperature and humidity in the CTRL run, whereas it is present in the observations. The wind direction, however, shows southerly flow below 500 m.a.g.l. in these profiles. Judging by the wind direction, this indicates an approximately 250 m deeper sea-breeze in the CTRL simulation than in the observations and FDDA simulation. The simulated wind speed between 250 and 500 m.a.g.l. is, however, very weak (below 2 m/s).

Towards the evening on 19 July (1744 and 1915 UTC profiles), the sea-breeze is still evident in the CTRL simulation, both in temperature, humidity as well as in wind direction. The CTRL simulation profiles of temperature above 250 m.a.gl. agree well with the observed and FDDA simulated profiles for these two latter instances. Below, however, there is a temperature deficit of 2-3 K, indicating that the sea-breeze is still present at Eyrarbakki in the CTRL simulation, while it is almost gone in the FDDA-all and FDDA-all-nowind simulations. At 1914 UTC, the sea-breeze is gone in the observations, still somewhat present in the lowermost atmospheric layer in FDDA-all simulation and evident in the CTRL simulation.

Figure 15 shows a vertical cross section of wind speed, wind direction and specific humidity at 1600 UTC.

The moist, southerly sea-breeze layer penetrates about 40 km inland in the FDDA-all simulation, which is 20-30 km further than in the CTRL simulation along this cross section. In the FDDA-all simulation, the sea-breeze layer over the sea contains stronger winds than in the CTRL simulation.

5) Case 2, July 20

On 20 July, clear signs of sea-breeze in the displayed profiles are only found at 1809 and 2025 UTC (Figures 12 and 13). The former and its subsequent profile (1932 UTC, not shown) were measured some 18 km to the east of Eyrarbakki and the sea-breeze set on slightly earlier at this location than at Eyrarbakki. At 1809 UTC, the sea-breeze is clearly

514 evident, but it is less than 200 metres deep at this time. At 2025 UTC, there is sea-breeze
515 at Eyrarbakki and it reaches around 500 m.a.g.l.

516 The temperature of the lower troposphere is generally better reproduced by the model
517 for the shown profiles than in Case 1 and only in the 1809 and 2025 UTC profiles and the
518 lower part of the 1507 UTC profile there are underestimations larger than 3 K.

519 As for the surface data, the approximation towards the CTRL values in the FDDA-single
520 experiments happens considerably faster in Case 2 than in Case 1.

521 While the average temperature underestimations are about the same aloft as at the AWSs
522 in Case 1, they are slightly larger aloft than at the AWSs in Case 2.

523 As seen in the horizontal wind and humidity fields (Figure 9), the sea-breeze penetrates
524 shorter inland in the FDDA-all than in the CTRL simulation. Along the investigated cross
525 section (Figure 16), this difference amounts to around 40 km. The sea-breeze layer is also gen-
526 erally shallower in the FDDA-all simulation. The offshore wind speed, however, is markedly
527 stronger (more than 10 m/s) in the FDDA-all than in the CTRL simulation.

528 5. Discussion

529 In this study, it has been shown how profile data from a small UAS can be used for
530 assimilation through the FDDA technique to improve high resolution numerical simulations.
531 The method has been applied to two summertime fair weather situations that took place in
532 Southwest Iceland during the Moso field campaign, on 19 and 20 July 2009.

533 The simulated near surface flow compares generally well against observations from a
534 relatively dense network of AWSs. Aloft, however, with exception to the 1200 UTC Keflavik
535 radiosoundings which compare well with the model (not shown), only the soundings made
536 with the UAS were available for validation. It is therefore hard to estimate the validity of
537 the impact of the assimilation on the flow field aloft. Similar future studies can definitely
538 benefit from more soundings of this kind, both for validation and also for assimilation.

Previous studies (e.g. Xu et al. 2002) have shown that the choice of nudging coefficients and radius of influence can have an important effect on the FDDA data assimilation result. Thus, as a first step in this study, several FDDA sensitivity experiments were carried out using different combinations of the two parameters. The results reveal only a marginal sensitivity to the choice of these parameters for our case studies and for any of the tested combinations of the parameters the results are markedly better than when using no FDDA at all. The default nudging coefficient of $6 \cdot 10^{-4}\mathrm{s}^{-1}$ and a radius of influence of 100 km, covering the area of interest, were therefore used for the rest of the study. These results are likely case dependent and more experiments with e.g. differing radii of influence for different domains and differing nudging coefficients for different parameters could prove beneficial, but are left for a future study.

The impact of the data assimilation on the model's representation of the sea-breeze circulation, which dominated the weather of southwestern Iceland during both studied situations, is large and positive, but it differs between the two investigated cases. In Case 1, the assimilation leads to a sea-breeze that penetrates further inland and the sea-breeze also has a sharper front. Away from the coast, further inland, the assimilation of the UAS data gives a local enhancement of the synoptic-scale flow, opposing the sea-breeze. The correctness of this latter flow enhancement is confirmed by two AWSs (Arnes and Mork) in the area. The sharpening of the sea-breeze front associated with increased speed of the sea-breeze and stronger opposing winds is consistent with the findings of Gahmberg et al. (2010) on sea-breeze and its relationships to synoptic flow. In Case 2, on the other hand, the assimilation of the UAS data leads to a sea-breeze that is weaker and which penetrates shorter inland.

Interestingly, the improvement seen when only assimilating the first profiles in each case (FDDA-single) is significantly larger and more long lasting in Case 1 than in Case 2. A possible explanation for this might be found in the differing synoptic conditions. Both cases had a northeasterly large-scale flow, but in Case 2 it was stronger which could potentially eradicate the impact of the assimilation faster than what is the case with the weaker flow in

Case 1.

A detailed physical interpretation of the FDDA simulation results is made difficult by the fact that the FDDA technique is based on terms in the prognostic model equations that are strictly speaking non-physical. However, the impacts of the nudging coefficients are related to time scales of true physical processes and they should ideally be determined based on location and flow dependent investigations. Nevertheless, the locally enhanced flow to the north of the investigated area in Case 1 can be mainly attributed to a modification of the Southwest Iceland thermal low, which is induced by higher boundary layer temperatures through the data assimilation. No such increase in wind speeds are seen when the UAS temperature data are left out of the assimilation.

Vastly underestimated surface temperatures are found in the vicinity of Reykjavik (e.g. up to 8 K in Reykjavik) in the simulation of Case 1 without data assimilation. This underestimation is caused by a fog that resides in the area for most of 19 July (see Figures 7 and 8). All FDDA-simulations aid in removing this erroneous fog, with the effect of assimilating the mass data being the largest. The fog may be removed through at least two processes: The higher boundary layer temperatures induced by assimilating the UAS temperature data may evaporate the fog and the enhanced northerly flow to the north of Reykjavik (due to lower surface pressure over Southwest Iceland) may transport the fog away. This northerly flow is also warmer than the air it replaces.

In both case studies, particularly large underestimations of the 2 m temperatures are found inland at the locations of Skalholt and Kalfholl. A detailed comparison of the USGS landuse dataset and official maps of the area reveals that the landuse contains too large water bodies or a too high a percentage of wetlands. The two mentioned stations are actually situated over water bodies in the model, while in reality they are only close to these. An additional simulation of Case 1 in which all inland water bodies in the south of Iceland were removed yielded a temperature increase of some 2-4 K at the aforementioned stations during daytime, even giving an overestimated temperature at some instances using an FDDA-all

setup. The effect of this landuse modification was, however, very local and its impact on the general flow field was negligible. This nevertheless underlines the sensitivity of the local boundary layer temperatures to the underlying surface. This may seem obvious, but ever since the publication of Einarsson (1971), there has been consensus that temperatures in Iceland are governed by synoptic scale advection and not local heat fluxes. Thus, future simulations of the local weather in the area could most likely benefit from a new and updated landuse dataset. Implementing such a dataset would, however, be a study in its own right and is therefore considered beyound the scope of the present study.

A clear advantage of the UAS system over for example AWSs is that it provides observations not only from near the surface, but also from an atmospheric column further aloft. Thereby, one can avoid several issues connected to e.g. the assimilation of only surface temperature observations, which are known to be especially problematic (e.g. Reen and Stauffer 2010). One such issue is connected to the surface heat flux, as its sign can change if the surface temperature is slightly increased by nudging the model towards observed surface temperatures. Such a switch in sign may lead to a drastic reduction in the boundary layer height. It is also well known that the assimilation of surface temperature observations can lead to an erroneous spread of temperatures not representative for the whole vertical extension of the ABL, as e.g. in the presence of a strongly stably stratified surface layer during nighttime or a superadiabatic surface layer during daytime (e.g. Stauffer and Seaman 1990). Solutions of various degrees of complication to these problems have been proposed. The switch in the surface heat flux can be avoided by nudging also the soil temperature (e.g. Reen and Stauffer 2010) and by making adjustments to the surface sensible and latent heat fluxes (Alapaty et al. 2001). Nudging a shallower layer when there are inversions and the whole ABL during events of free convection can mitigate the problem connected to strong temperature gradients near the surface. Nevertheless, these techniques are not optimal solutions and frequent profile observations as those provided by the UAS SUMO have the potential of avoiding the need to use them.

The inland penetration of the two investigated sea-breezes was in this study deduced by manually investigating the AWS observations and corresponding model point estimations and horizontal fields. Future studies, including more cases and experiments, could benefit from a more statistical approach, as the objective technique proposed by Case et al. (2004).

The presented combination of WRF-FDDA and data acquired with a UAS is not limited to only sea-breeze studies, but is likely to have a wide range of future applications. One example application in which one needs accurate high resolution simulations and observations is investigations of flow in connection to existing and future wind farms. A related system is already proposed by Liu et al. (2011), where observations are combined with very high resolution LES simulations using FDDA. The UAS SUMO would be an ideal tool for the verification and provision of atmospheric data for assimilation in such a system. SUMO has already been utilised to measure atmospheric turbulence in and around a small wind farm in Denmark, during spring 2011, as an integral part of the the joint research project "Autonomous Aerial Sensors for Wind Power Meteorology" (Giebel et al. 2012; Reuder et al. 2012).

Another potential future application for the SUMO-WRF-FDDA system is weather nowcasts or forecasts for search and rescue (SAR) missions, as proposed by Rögnvaldsson (2011). Such missions depend critically on accurate weather information, both as the safety of the field personnel must be secured and as the missions must be run as efficiently as possible. Rescue missions often take place in remote areas or regions severely affected by natural catastrophes. For the provision of in-situ meteorological data from the affected area, UAS represents a unique tool that can provide in-situ data from such regions where conventional instrument platforms may not be applicable and manned flights too dangerous. An example of another modelling system for emergency response applications is that by Warner et al. (2004).

6. Summary and conclusions

Two summertime situations with northeasterly synoptic flow in Southwest Iceland have been explored with a network of AWSs and the UAS SUMO.

Both flow situations are characterised by strong diurnal variation in boundary layer temperatures leading to thermally driven winds, predominantly in the form of sea-breeze circulation along the coast. These winds are to some extent reproduced by numerical downscaling of a state of the art ECMWF operational analysis using the WRF model. However, by assimilating profile data from the UAS measured at Eyrarbakki in Southwest Iceland using the FDDA technique, substantial improvements of wind, temperature and humidity in the region are achieved.

The Southwest Iceland sea-breeze of 19 July 2009 penetrates about 40 km inland and reaches 250-300 m height at the coast. On this day, a modification of the thermal low over Southwest Iceland generated through the assimilation of data from the UAS SUMO contributes to enhanced northerly flow at the west coast of Iceland, north of Reykjavik City. Thus, the penetration of cold and humid maritime air towards the city is inhibited and temperatures remain 6-8 K higher than in the simulation without the UAS data assimilated.

This study furthermore shows that accurate simulations of coastal weather at high latitudes are very dependent on a correct description of the boundary layer.

Envisioned future applications of the presented UAS SUMO and WRF-FDDA system include wind energy, e.g. siting for wind farms and intra wind farm measurements and simulations and the improvement of local scale nowcasts and forecasts for e.g. search and rescue missions.

7. Acknowledgments

The authors are grateful for the assistance in field by Dubravka Rasol and Sigurður Jónsson during Moso and the technical support on the UAS SUMO by Martin Müller and Chris-

tian Lindenberg. The work was in part funded by the Icelandic Technology Development Fund (grant number 110338-0611). The helpful comments of three anonymous reviewers are greatly appreciated.

References

Alapaty, K., N. L. Seaman, N. D. S., and A. F. Hanna, 2001: Assimilating Surface Data to Improve the Accuracy of Atmospheric Boundary Layer Simulations. *J. Appl. Meteor.*, **40**, 2068–2082.

Anthes, R., 1974: Data assimilation and initialization of hurricane prediction models. *J. Atmos. Sci.*, **31**, 702 – 718.

Brisset, P., A. Drouin, M. Gorraz, P. Huard, and J. Tyler, 2006: The Paparazzi Solution. Http://www.recherche.enac.fr/paparazzi/papers_2006/mav06_paparazzi.pdf.

Bromwich, D. H., L. Bai, and G. G. Bjarnason, 2005: High-Resolution Regional Climate Simulations over Iceland Using Polar MM5. *Mon. Wea. Rev.*, **133**, 3527 – 3547.

Case, J. L., J. Manobianco, J. E. Lane, C. D. Immer, and F. J. Merceret, 2004: An Objective Technique for Verifying Sea Breezes in High-Resolution Numerical Weather Prediction Models. *Wea. Forecasting*, **19**, 690–705.

Chen, F. and J. Dudhia, 2001: Coupling an Advanced Land Surface-Hydrology Model with the Penn State-NCAR MM5 Modeling System. Part 1. Model Implementation and Sensitivity. *Mon. Wea. Rev.*, **129**, 569–585.

Curry, J. A., J. Maslanik, G. Holland, and J. Pinto, 2004: Applications of Aerosondes in the Arctic. *Bull. Amer. Meteor. Soc.*, **85 (12)**, 1855–1861.

Dudhia, J., 1989: Numerical study of convection observed during the winter monsoon experiment using a mesoscale two-dimensional model. *J. Atmos. Sci.*, **46**, 3077–3107.

Einarsson, M. A., 1971: Meteorology (in Icelandic) . 99pp.

Fast, J. D., 1995: Mesoscale Modeling and Four-Dimensional Data Assimilation in Areas of Highly Complex Terrain. *J. Appl. Meteor.*, **34**, 2762 – 2782.

Fuentes, M., L. Chen, J. M. Davis, and G. M. Lackmann, 2005: Modeling and predicting complex space-time structures and patterns of coastal wind fields. *Environmetrics*, **16**, 449–464.

Gahmberg, M., H. Savijärvi, and M. Leskinen, 2010: The influence of synoptic scale flow on sea breeze induced surface winds and calm zones. *Tellus*, **62A**, 209–217.

Giebel, G., S. U. Paulsen, J. Bange, A. la Cour Harbo, J. Reuder, S. Mayer, and A. van den Kroonenberg, 2012: *Autonomous Aerial Sensors for Wind Power Meteorology - A Pre-Project*. Risø DTU, report R-1798(EN). ISBN 978-87-550-3945-2, 94 pp.

Grønås, S. and A. D. Sandvik, 1998: Numerical simulations of sea and land breezes at high latitudes. *Tellus*, **50A**, 468–489.

Hong, S.-Y., Y. Noh, and J. Dudhia, 2006: A new vertical diffusion package with an explicit treatment of entrainment process. *Mon. Wea. Rev.*, **134**, 2318–2341.

Jonassen, M. O., 2008: The Small Unmanned Meteorological Observer (SUMO) - Characerization and test of a new meaurement system for atmospheric boundary layer research. *Master's thesis. Geophysical institute, University of Bergen. http://web.gfi.uib.no/forskning/Master/Master_Jonassen.pdf.*

Jónsson, T., 2002: A brief investigation of diurnal variation of wind speed and wind directions in June (In Icelandic). *Veðurstofa Íslands (Icelandic meteorological office)* , **Tech. Rep. 02030**, 12pp.

Konrad, T., M. Hill, J. Rowland, and M. J.H., 1970: A small, radio-controlled aircraft as a platform for meteorological sensors. *Appl. Phys. Lab. Tech. Digest*, **11**, 11–19.

Langland, R. H., et al., 1999: The North Pacific Experiment (NORPEX-98): Targeted Observations for Improved North American Weather Forecasts. *Bull. Amer. Meteor. Soc.*, **80**, 1363–1384.

720 Liu, Y., A. Bourgeois, T. Warner, S. Swerdin, and J. Hacker, 2005: Implementation of
721 observation-nudging based FDDA into WRF for supporting ATEC test operations. *6th*
722 *WRF/15th MM5 Users Workshop, Boulder, Colorado, NCAR.*

723 Liu, Y., et al., 2011: Simultaneous nested modeling from the synoptic to the LES scale for
724 wind energy applications. *J. Wind Eng. Ind. Aerodyn.*, **99**, 308 – 319.

725 Martin, S., J. Bange, and F. Beyrich, 2011: Meteorological profiling of the lower troposphere
726 using the reaserch UAV "M2AV Carolo". *Atmos. Meas. Tech.*, **4**, 705 – 716.

727 Mayer, S., G. Hattenberger, P. Brisset, M. O. Jonassen, and J. Reuder, 2012: A 'no-flow-
728 sensor' wind estimation algorithm for Unmanned Aerial Systems. *Int. J. Micro Air Vehi-*
729 *cles*, **4**, 15–29.

730 Mayer, S., A. Sandvik, M. O. Jonassen, and J. Reuder, 2010: Atmospheric profiling with
731 the UAS SUMO: a new perspective for the evaluation of fine-scale atmospheric models.
732 *Meteor. Atmos. Phys.*, doi: 10.1007/s00703-010-0063-2.

733 Mlawer, E. J., S. J. Taubman, P. D. Brown, M. J. Iacono, and S. A. Clough, 1997: Radiative
734 transfer for inhomogeneous atmospheres: RRTM, a validated correlated-k model for the
735 longwave. *J. Geophys. Res.*, **102**, 16 663 – 16 682.

736 Nance, L. B. and D. R. Durran, 1997: A Modeling Study of Nonstationary Trapped Mountain
737 Lee Waves. Part I: Mean-Flow Variability. *J. Atmos. Sci.*, **54**, 2275 – 2291.

738 Otkin, J. A., D. C. Hartung, D. D. Turner, R. A. Petersen, W. F. Feltz, and E. Janzon, 2011:
739 Assimilation of Surface-Based Boundary Layer Profiler Observations during a Cool-Season
740 Weather Event Using An Observing System Simulation Experiment. Part I: Analysis Im-
741 pact. *Mon. Wea. Rev.*, **139**, 2309 – 2326.

742 Pielke, R. A., 1974: A Three-Dimensional Numerical Model of the Sea Breezes Over South
743 Florida. *Mon. Wea. Rev.*, **102**, 115 – 139.

744 Pielke, R. A., 2002: *Mesoscale meteorological modelling, 2nd edition.* Academic Press, San
745 Diego, 676 pp.

746 Pleim, J. E. and A. Xiu, 1995: Development and Testing of a Surface Flux and Planetary
747 Boundary Layer Model for Application in Mesoscale Models. *J. Appl. Meteor.*, **34**, 16–31.

748 Reen, B. P. and D. R. Stauffer, 2010: Data Assimilation Strategies in the Planetary Boundary
749 Layer. *Bound.-Lay. Meteor.*, **137**, 237 – 269.

750 Reuder, J., P. Brisset, M. O. Jonassen, M. Müller, and S. Mayer, 2009: The Small Unmanned
751 Meteorological Observer SUMO: A new tool for atmospheric boundary layer research.
752 *Meteor. Z.*, **18**, 141 – 147.

753 Reuder, J., M. O. Jonassen, and H. Ólafsson, 2012: The Small Unmanned Meteorological
754 Observer SUMO: Recent developments and applications of a micro-UAS for atmospheric
755 boundary layer research,. *Accepted in Acta Geophys.*

756 Reuder, J., et al., 2011: FLOHOF 2007: An overview of the mesoscale meteorological field
757 campaign at Hofsjökull, Central Iceland. *Meteor. Atmos. Phys.*, DOI: 10.1007/s00 703–
758 010–0118–4.

759 Rögnvaldsson, O., 2011: Search and rescue, Weather prediction system assists huminatarian
760 aid. *Meteorological technology international*, 76 – 78.

761 Rögnvaldsson, O., H. Ágústsson, E. M. Einarson, H. Ólafsson, H. Björnsson, and
762 O. G. B. Sveinsson, 2007: Status report for year one of the RAV project (In Icelandic).
763 Http://thjarkur.orkugardur.is/wordpress/wp-content/uploads/RAVarsskyrsla2007.pdf.

764 Schroeder, A. J., D. R. Stauffer, N. L. Seaman, A. Deng, A. M. Gibbs, G. K. Hunter, and
765 G. S. Young, 2006: An Automated High-Resolution, Rapidly Relocatable Meteorological
766 Nowcasting and Prediction System. *Mon. Wea. Rev.*, **134**, 1237 – 1265.

767 Skamarock, W. C., et al., 2008: A description of the Advanced Research WRF Version 3.
768 *NCAR Tech. Note*, **TN-475+STR**, 125.

769 Soler, M. R., R. Arasa, M. Merino, and M. Olid, 2011: Modelling Local Sea-Breeze Flow
770 and Associated Dispersion Patterns Over a Coastal Area in North-East Spain: A Case
771 Study. *Bound.-Lay. Meteor.*, **140**, 37–56.

772 Stauffer, D. R. and N. L. Seaman, 1990: Use of four-dimensional data assimilation in a
773 limited-area mesoscale model. Part I: Experiments with synoptic-scale data . *Mon. Wea.*
774 *Rev.*, **118**, 1250 – 1277.

775 Stauffer, D. R. and N. L. Seaman, 1994: Multiscale Four-Dimensional Data Assimilation. *J.*
776 *Appl. Meteor.*, **33**, 416 – 434.

777 Stauffer, D. R., N. L. Seaman, and F. S. Binkowski, 1991: Use of four-dimensional data
778 assimilation in a limited-area mesoscale model. Part II: Effects of data assimilation within
779 the planetary boundary layer . *Mon. Wea. Rev.*, **119**, 734 – 754.

780 Stull, R. B., 1988: *An Introduction to Boundary Layer Meteorology*. Kluwer Academic Pub-
781 lishers, 666 pp.

782 Teixeira, J., et al., 2008: Parameterization of the atmospheric boundary layer: A view from
783 just above the inversion. *Bull. Amer. Meteor. Soc.*, **89**, 453 – 458.

784 Van den Kroonenberg, A., T. Martin, M. Buschmann, and P. Bange, J. Vörsmann, 2008:
785 Measuring the wind vector using the autonomous Mini Aerial Vehicle M2AV. *J. Atmos.*
786 *Ocean. Technol.* , **25**, 1969 – 1982.

787 Warner, T. T., R. A. Anthes, and A. L. McNab, 1978: Numerical Simulations with a Three-
788 Dimensional Mesoscale Model. *Mon. Wea. Rev.*, **106**, 1079 – 1099.

Warner, T. T., J. F. Bowers, S. P. Swerdlin, and B. A. Beitler, 2004: A Rapidly Deployable Operational Mesoscale Modeling System for Emergency-Response Applications. *Bull. Amer. Meteor. Soc.*, **85**, 709 – 716.

Xu, M., Y. Liu, C. A. Davis, and T. T. Warner, 2002: Sensitivity study on nudging parameters for a mesoscale FDDA system. *Preprints, 15th Conf. On Numerical Weather Prediction, San Antonio, TX, 10-16 August.*

List of Tables

TABLE 1. SUMO flights made on 19 and 20 July 2009 during the Moso field campaign. The time is the average time during the flight descent. The lowest altitude with temperature and humidity observations is 10 metres and for wind it is 70 metres.

ID	Time [UTC]	Max alt. [m.a.g.l.]	Duration [min.]
		19 July	
1	1238	3001	18
2	1300	1236	8
3	1319	1082	10
4	1339	1097	8
5	1358	1124	8
6	1518	1098	7
7	1541	1480	8
8	1605	953	7
9	1633	2830	14
10	1651	1204	9
11	1708	1437	13
12	1744	1200	10
13	1755	725	5
14	1822	1443	10
15	1841	1452	12
16	1856	1144	8
17	1914	1820	13
		20 July	
1	1109	2991	14
2	1157	1497	7
3	1306	1578	10
4	1410	1980	15
5	1507	1804	11
6	1607	2144	14
7	1710	1422	8
8	1809	1966	9
9	1832	1993	14
10	1932	607	8
11	2025	806	4

TABLE 2. WRF FDDA sensitivity experiments with different radii of influence (R) and nudging coefficients (G).

name	**R [km]**	**G [s^{-1}]**
FDDA R1G1	100	$6 \cdot 10^{-4}$
FDDA R2G1	50	$6 \cdot 10^{-4}$
FDDA R3G1	150	$6 \cdot 10^{-4}$
FDDA R1G2	100	$3 \cdot 10^{-4}$
FDDA R1G3	100	$12 \cdot 10^{-4}$

List of Figures

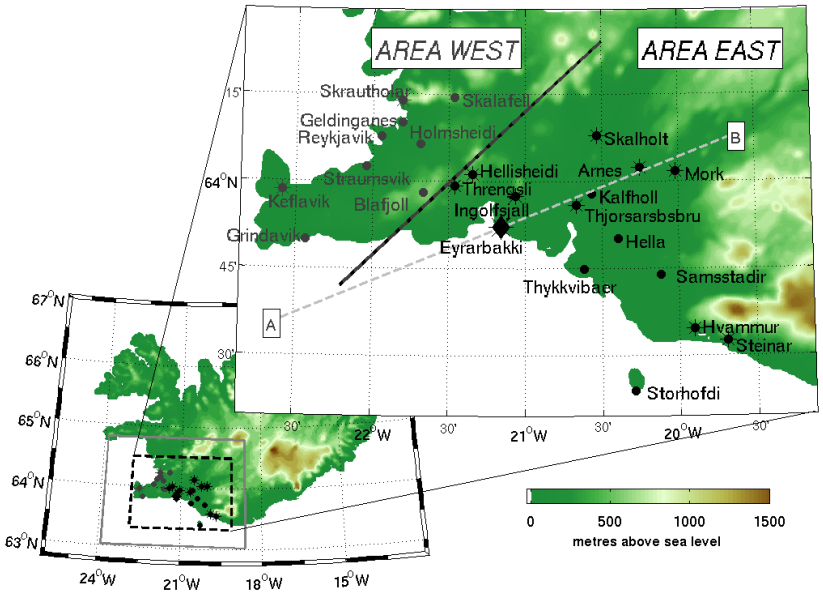

FIG. 1. Overview over the experiment area (large panel, upper right). The area is slightly smaller than domain 3 (grey box in smaller panel, lower left). The locations of the automatic weather stations are indicated by dots and names. The stations additionally marked with a star do not measure relative humidity. The main observation site for the UAS SUMO, Eyrarbakki, is marked by a diamond. Area East is the area of main interest where the studied sea-breeze events took place. The geographical division between Area East and Area West is indicated by a black line. The grey, dashed line (from A to B) indicates the position of the vertical cross sections of wind speed and specific humidity in Figures 15 and 16.

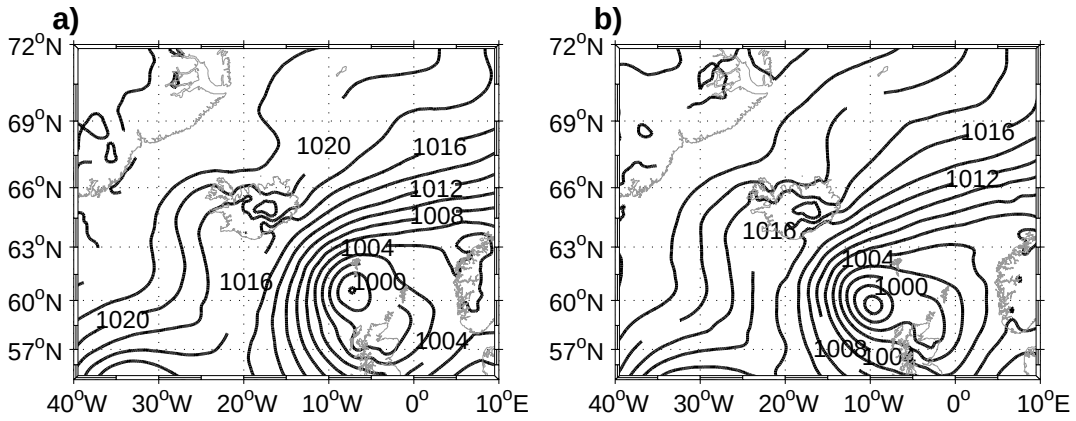

FIG. 2. Mean sea level pressure (hPa) at 1200 UTC on a) 19 July, and b) 20 July 2009, based on analysis from ECMWF.

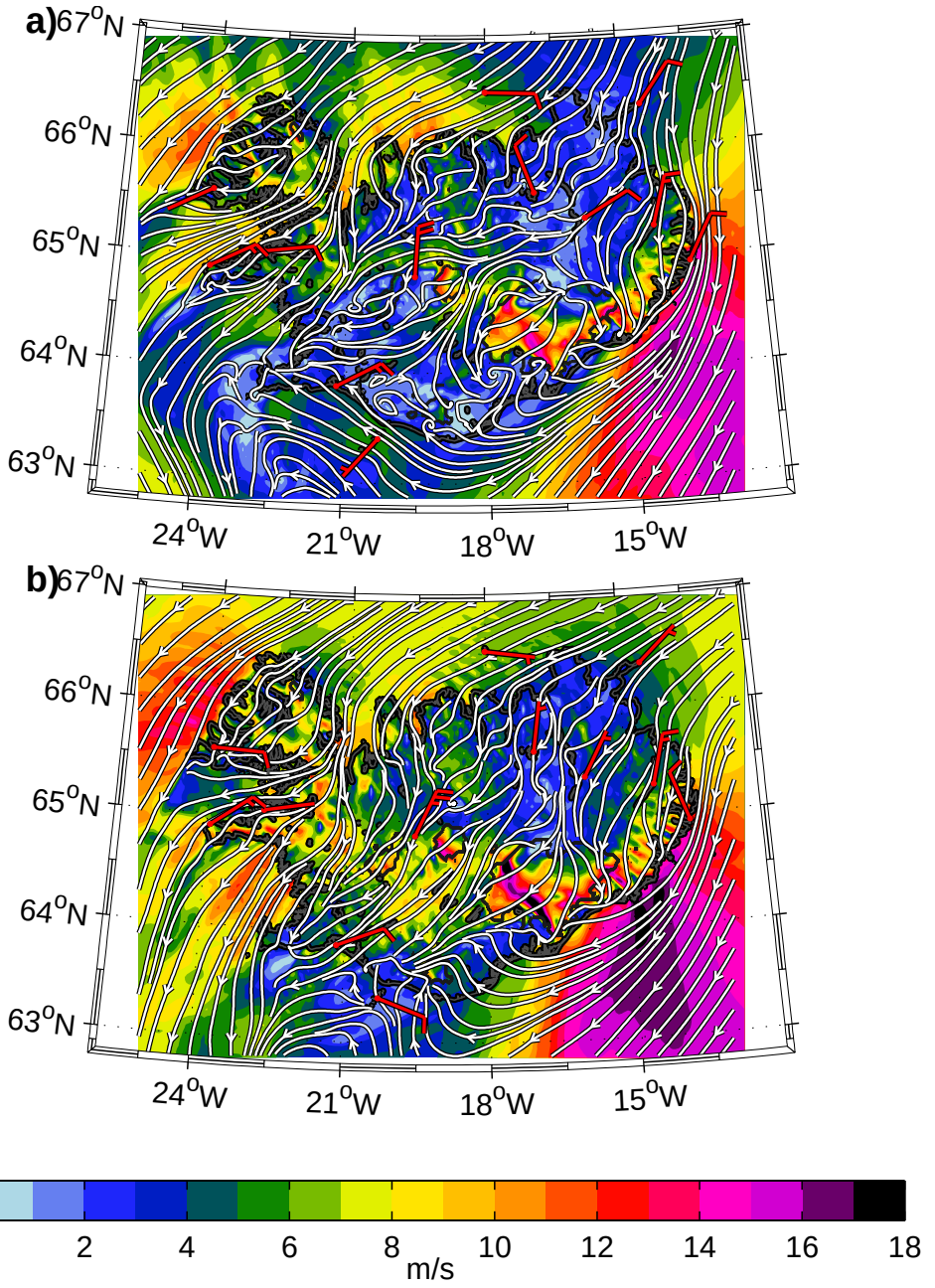

FIG. 3. Simulated near surface (10 m) winds from the CTRL simulations at 1200 UTC on a) 19 July and b) 20 July for domain 2 (3 km horizontal resolution). Surface observations from AWSs are indicated with red wind barbs. Each half barb represents 2.5 m/s.

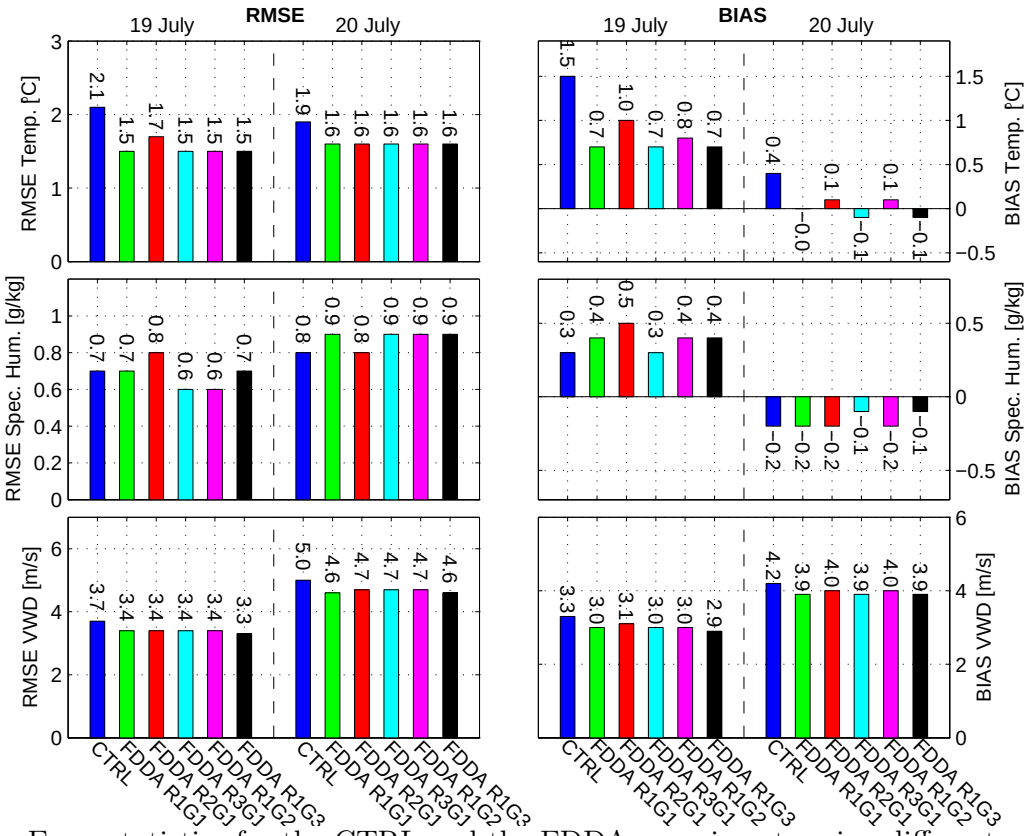

FIG. 4. Error statistics for the CTRL and the FDDA experiments using different combinations of the radius of influence (R) and nudging coefficients (G). Table 2 lists and explains the different experiments.

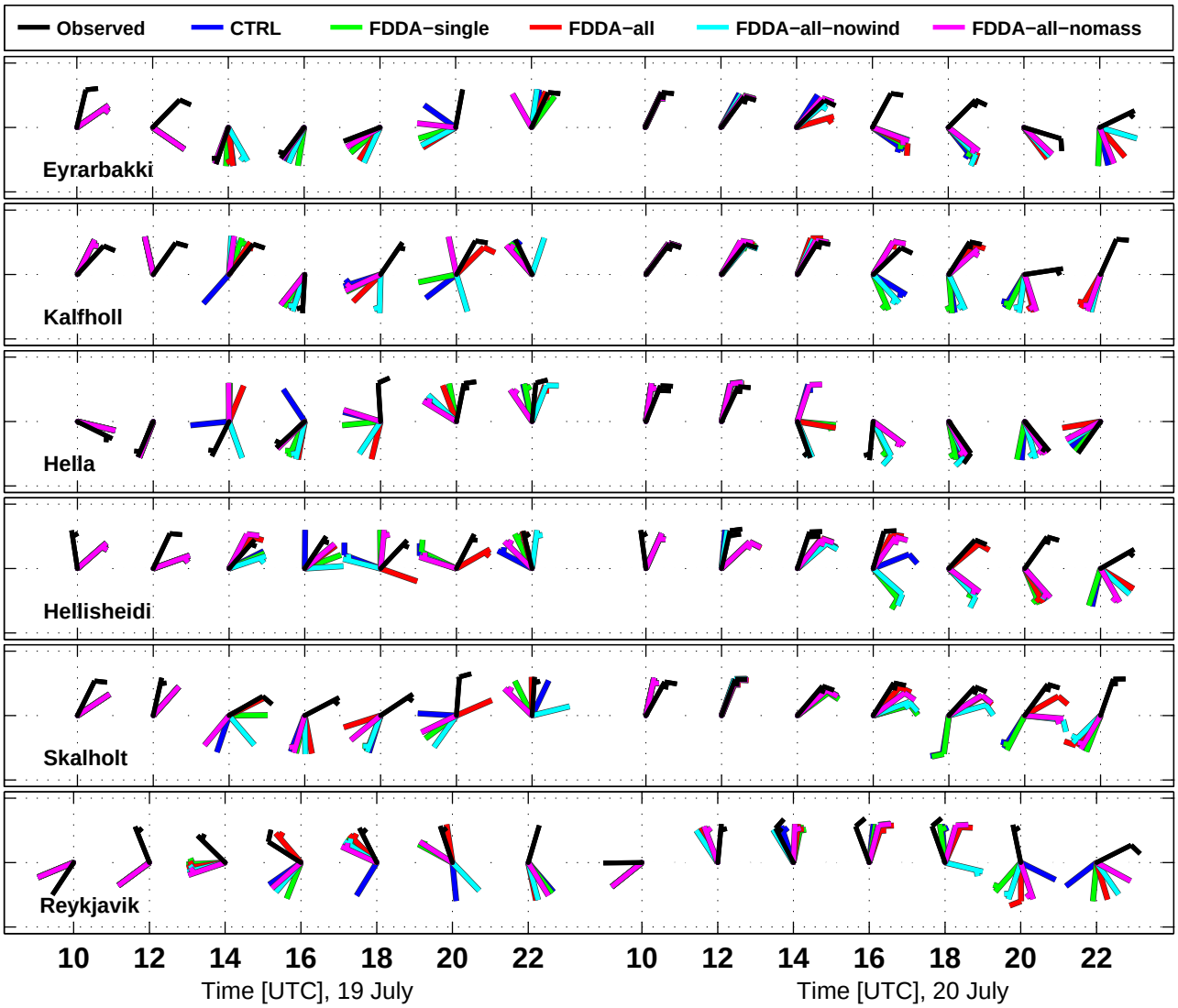

FIG. 5. Observed and simulated 10 m wind direction [°] and wind speed [m/s] at selected surface stations on 19 and 20 July, 2009. Each half barb represents 2.5 m/s. The simulation results are from domain 3 (1 km horizontal resolution).

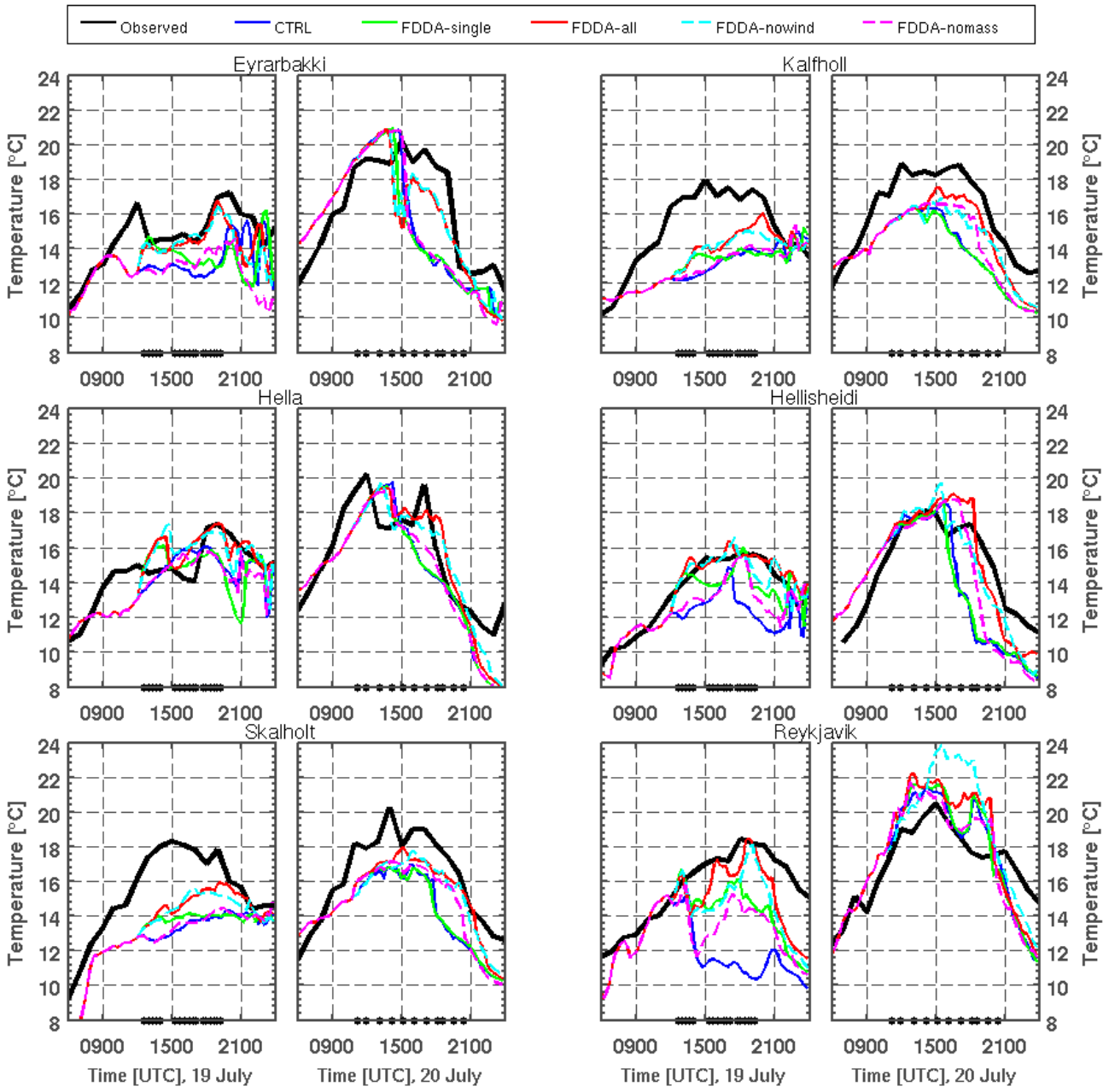

FIG. 6. Observed and simulated 2 m temperature [°C] at selected AWSs on 19 and 20 July, 2009. The simulation results are from domain 3 (1 km horizontal resolution). Black dots at the bottom-line of each panel's x-axis indicate the time of UAS soundings.

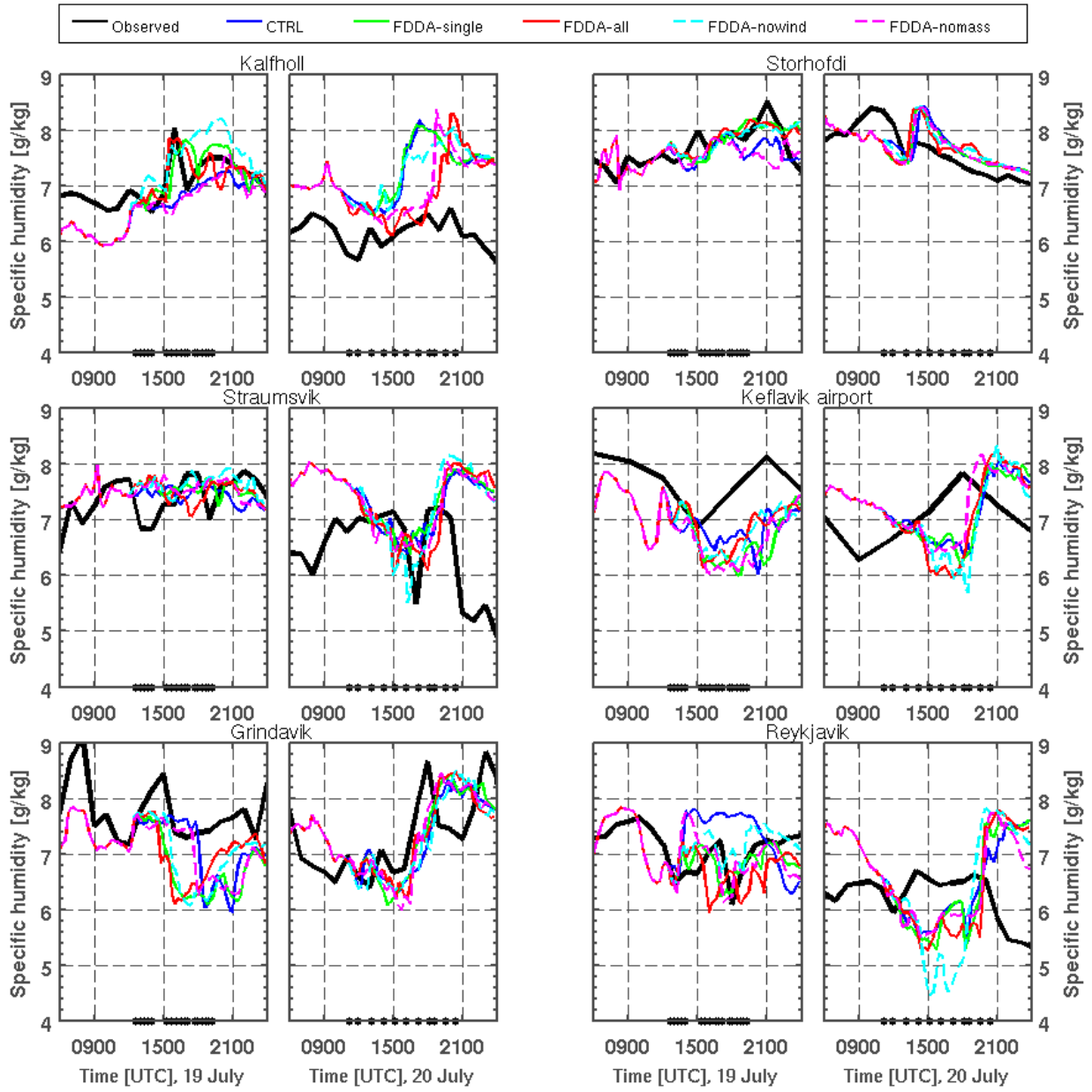

FIG. 7. Observed and simulated 2 m specific humidity [g/kg] at selected AWSs on 19 and 20 July, 2009. The simulation results are from domain 3 (1 km horizontal resolution). Black dots at the bottom-line of each panel's x-axis indicate the time of UAS soundings.

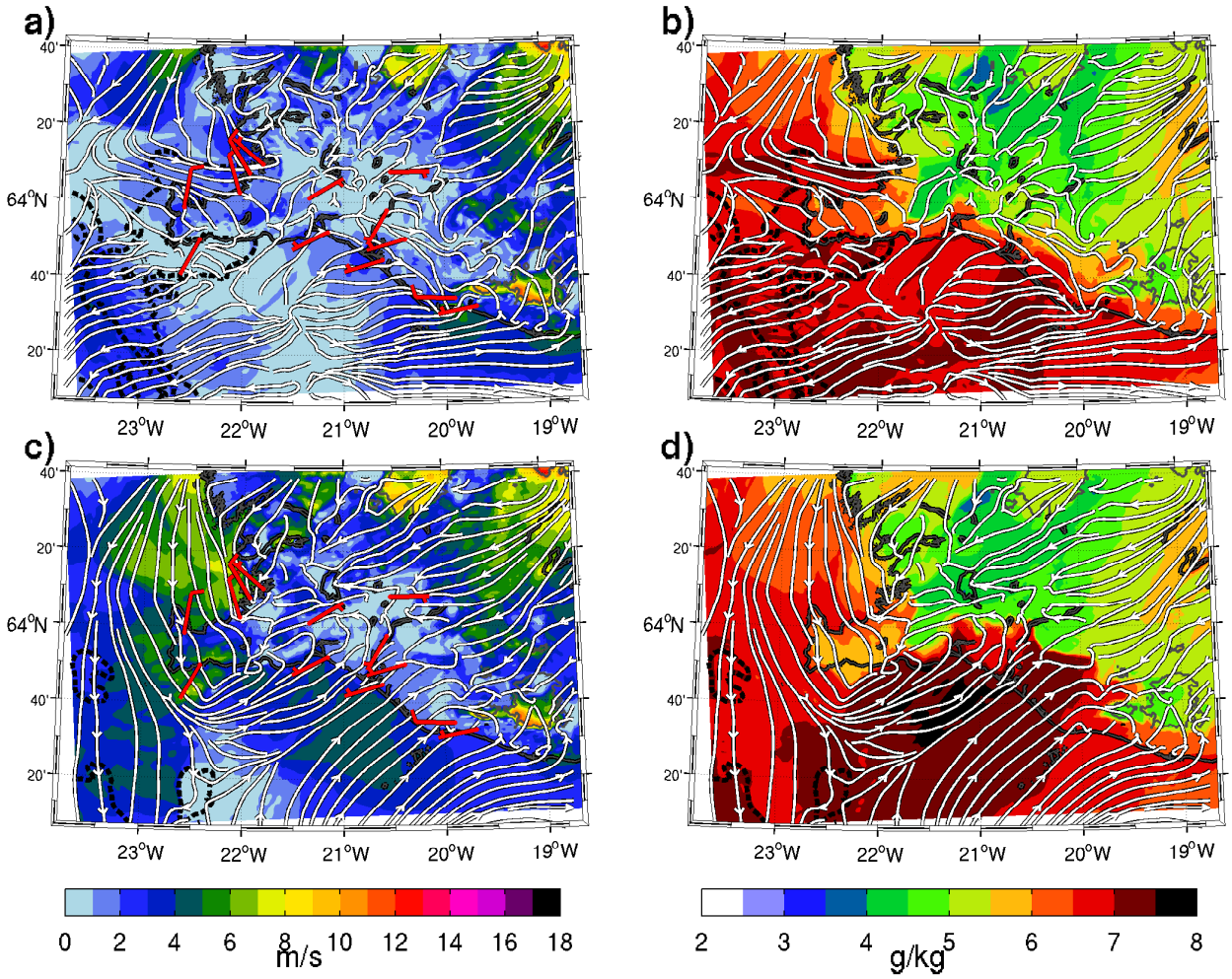

FIG. 8. Simulated 10 m wind speed [m/s] and wind direction and specific humidity [g/kg] from the lowermost model half level (approximately 9 m.a.g.l.) in domain 3 (1 km horizontal resolution) at 1600 UTC on 19 July 2009 for the CTRL simulation (**a)** and **b)**), and the FDDA-all simulation (**c)** and **d)**). Observations of wind speed and wind direction at selected surface stations are included as well (red wind barbs). Each half barb represents 2.5 m/s. Areas with over 98 % relative humidity are encircled by a black, dashed line.

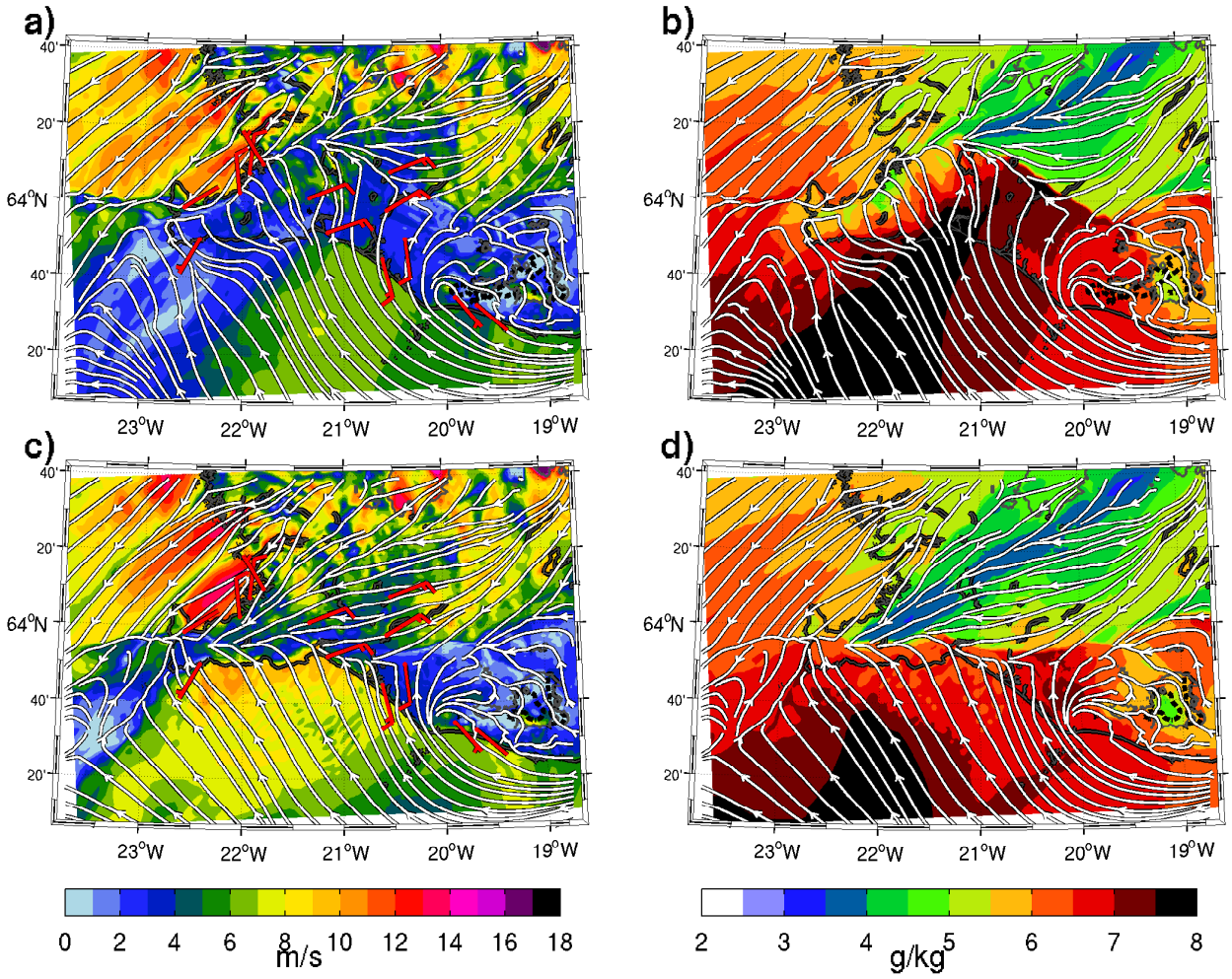

FIG. 9. Same as in Figure 8, but for 1800 UTC on 20 July, 2009.

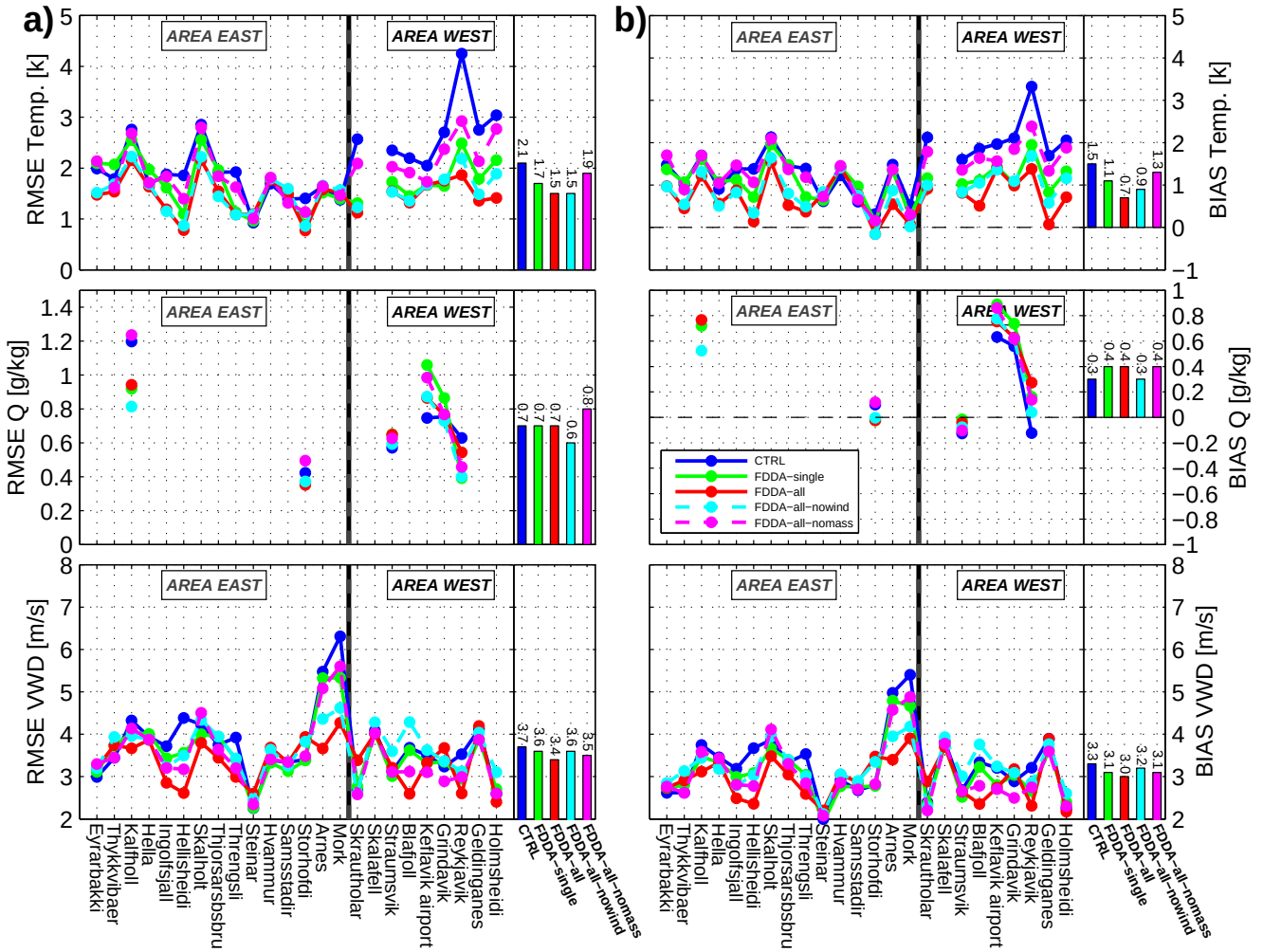

FIG. 10. Root mean square error (RMSE) (a) and bias (mean error) (b) between observed and simulated 2 m temperature, 2 m specific humidity and 10 m vector wind difference (VWD) for 19 July, 2009. Mean values of the RMSE and bias for all stations for each simulation are given with vertical bars. Area East is where the studied sea-breeze events took place.

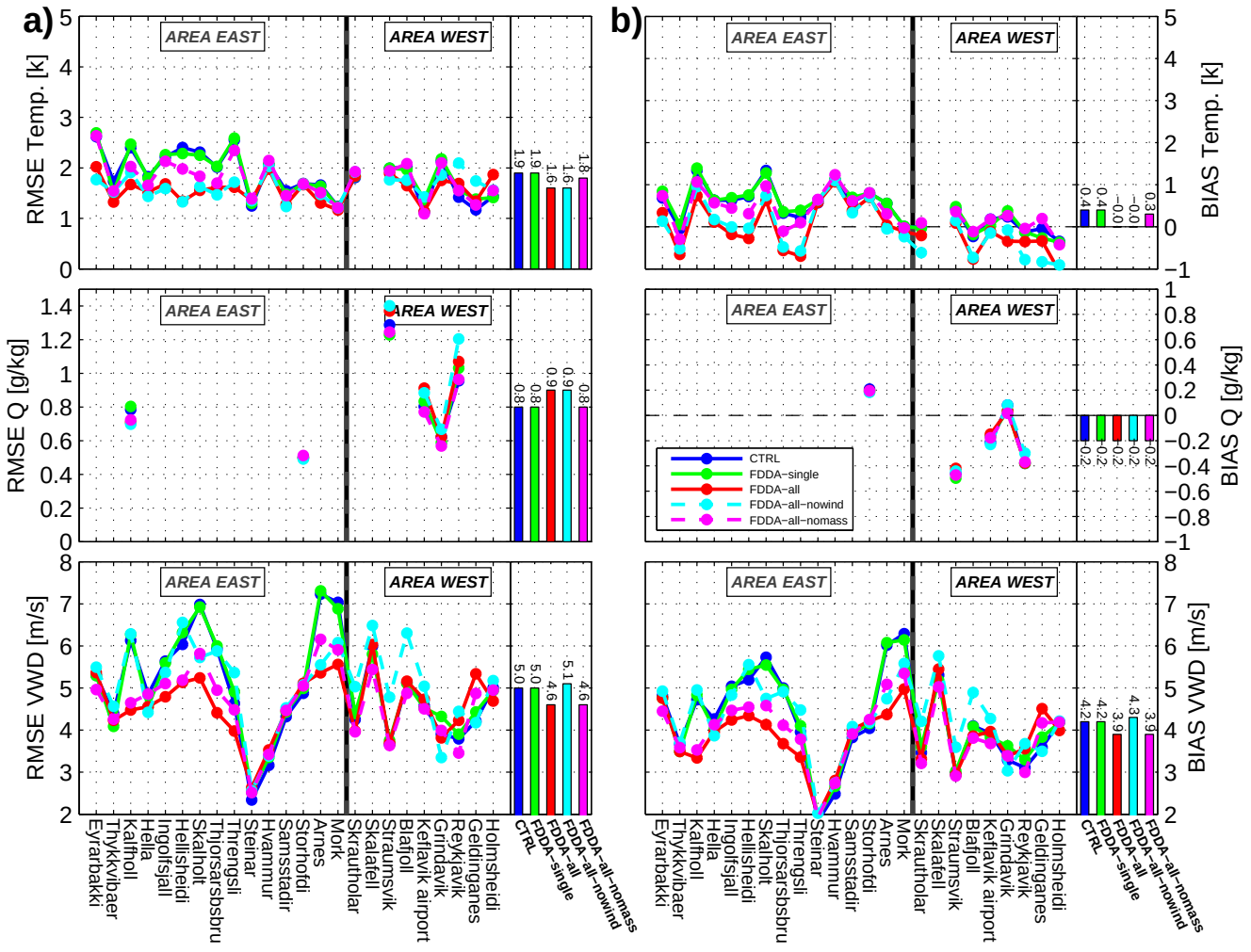

FIG. 11. Same as in Figure 10, but for 20 July, 2009.

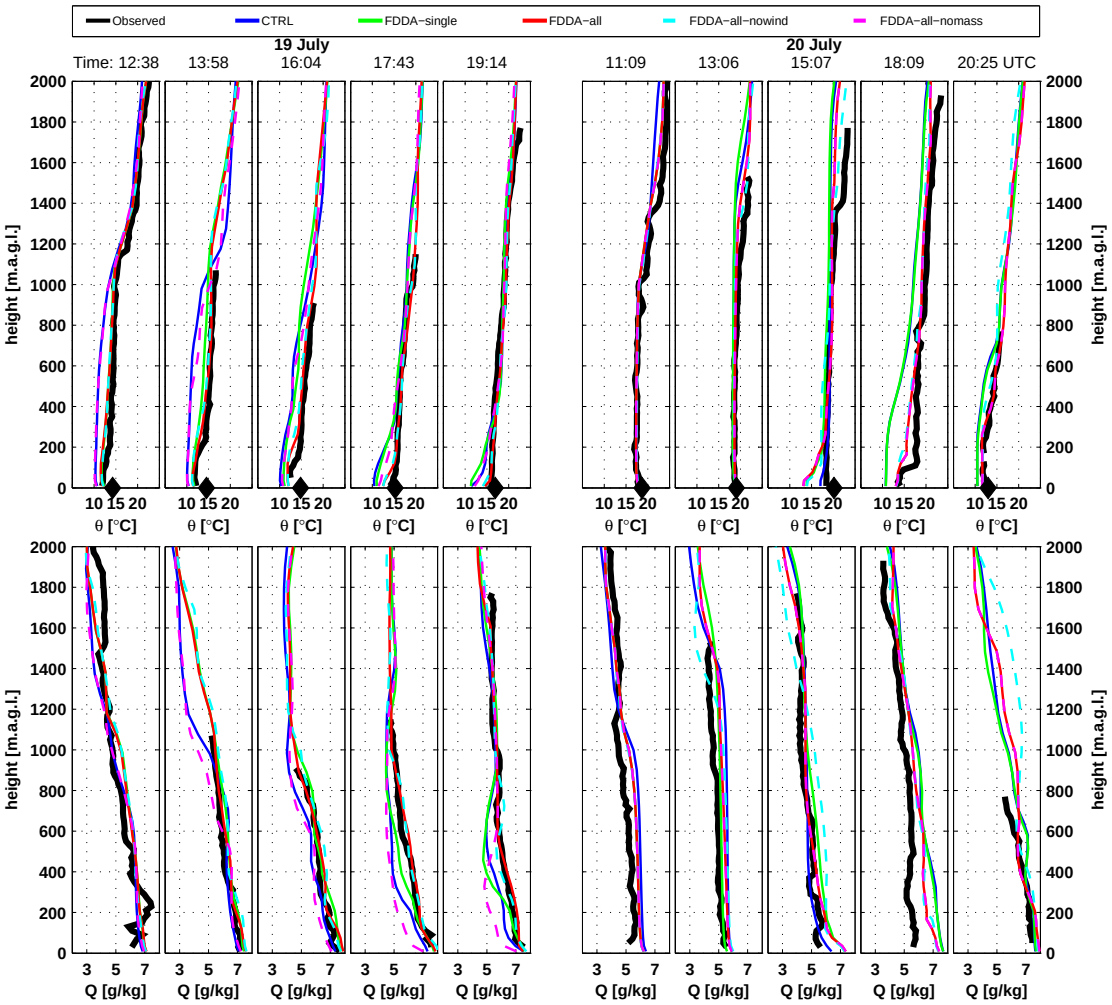

FIG. 12. Observed and simulated profiles of potential temperature (Θ) and specific humidity (Q) from Eyrarbakki on 19 and 20 July, 2009. Observations made by the AWS at Eyrarbakki are indicated with black diamonds. The 1809 UTC profile on 20 July is measured some 18 km to the east of Eyrarbakki.

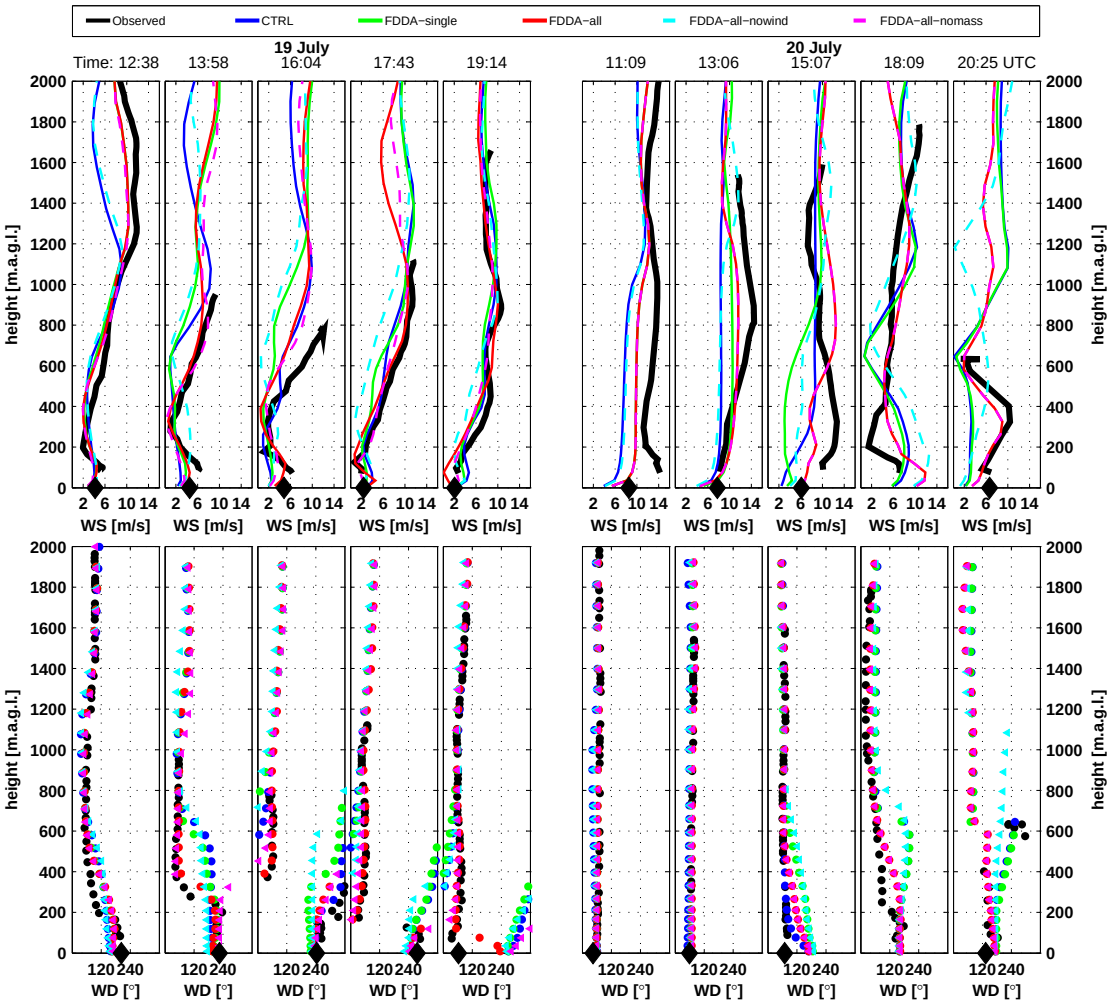

FIG. 13. Same as in 12, but for wind speed and wind direction.

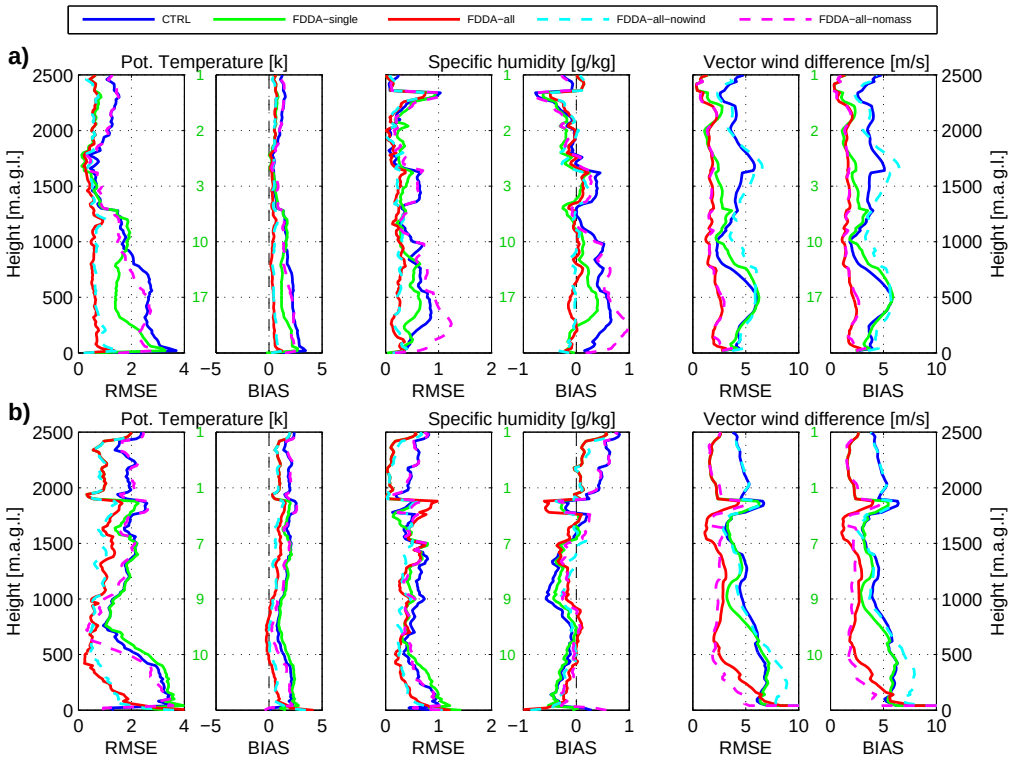

FIG. 14. RMSE and bias (mean error) between the observed and simulated atmospheric profiles of potential temperature, specific humidity and vector wind difference at Eyrarbakki on 19 July (panels a) and 20 July (panels b), 2009. The numbers in green indicate the number of soundings reaching each respective height above the ground level.

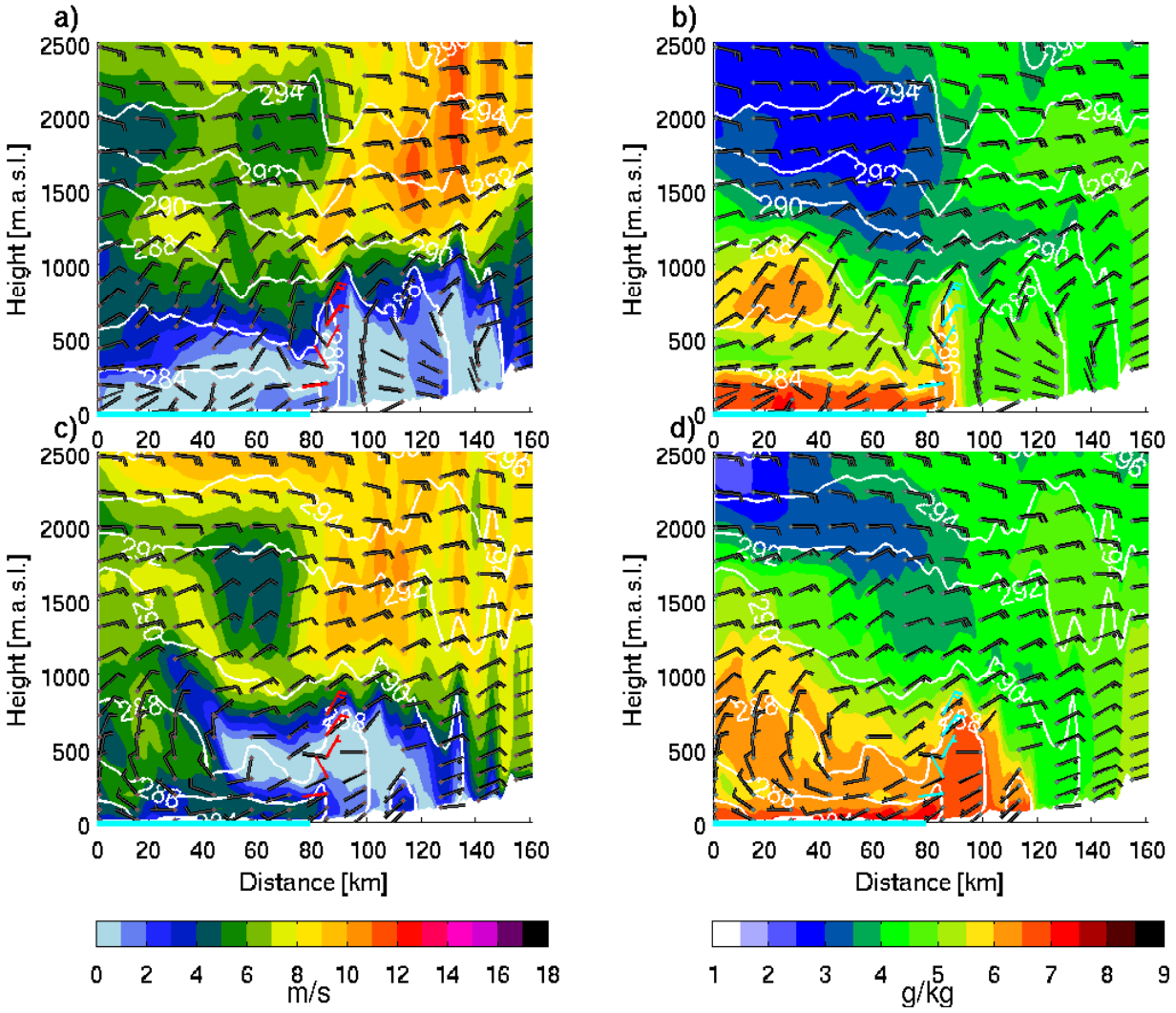

FIG. 15. Vertical cross sections of simulated wind speed and specific humidity at 1600 UTC on 19 July 2009 for the CTRL simulation (**a)** and **b)**) and FDDA-all simulation (**c)** and **d)**) in domain 3 (1 km horizontal resolution). Isentropes are given with white contours at an interval of 2 K. Each half barb represents 2.5 m/s. The geographical location of the cross section is shown in Figure 1. UAS wind measurements are indicated as well (red and cyan wind barbs). The offshore part is marked with a horizontal, solid line in cyan.

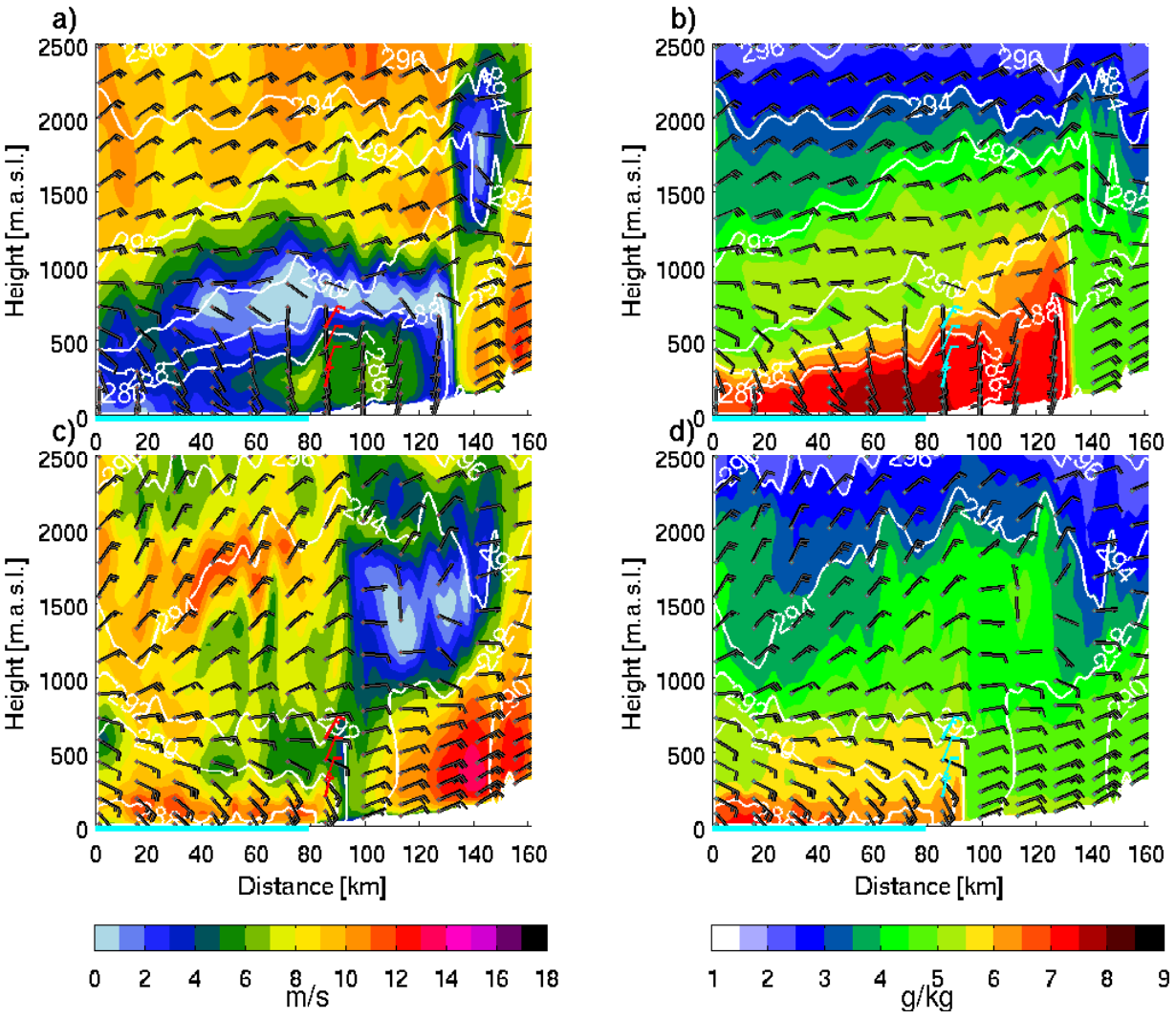

FIG. 16. Same as in 15, but for 1800 UTC on 20 July, 2009.